

DESIGN AND OPTIMIZATION OF A CENTRIFUGAL PUMP'S IMPELLER FOR HYDRO STORAGE PURPOSES

OVERVIEW ON HYBRID WIND-HYDRO POWER DIMENSIONING



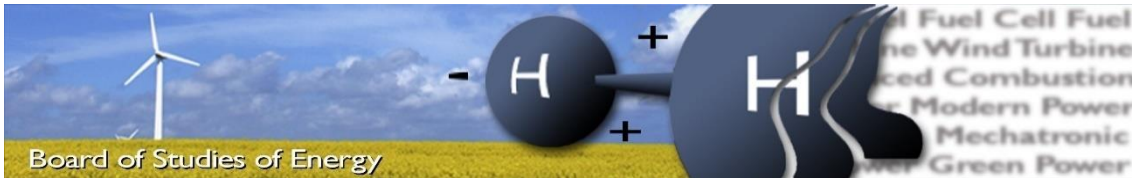
AALBORG UNIVERSITET

GROUP TE6-600

AALBORG UNIVERSITY

BACHELOR PROJECT

June 9th 2017



Title: Design and optimization of a centrifugal pump's impeller for hydro storage purposes. Overview on hybrid wind-hydro power dimensioning

Semester: 6th

Semester theme: Thermo-mechanical energy systems

Project period: 02/02/2017-09/07/2017

ECTS: 20 ECTS

Supervisor: Chungen Yin, Henrik Sørensen

Project group: TE6-601

Helena Domenech Guxens

Pages, total: 132

Appendix: 1,2

Supplements: see attached folder

SYNOPSIS:

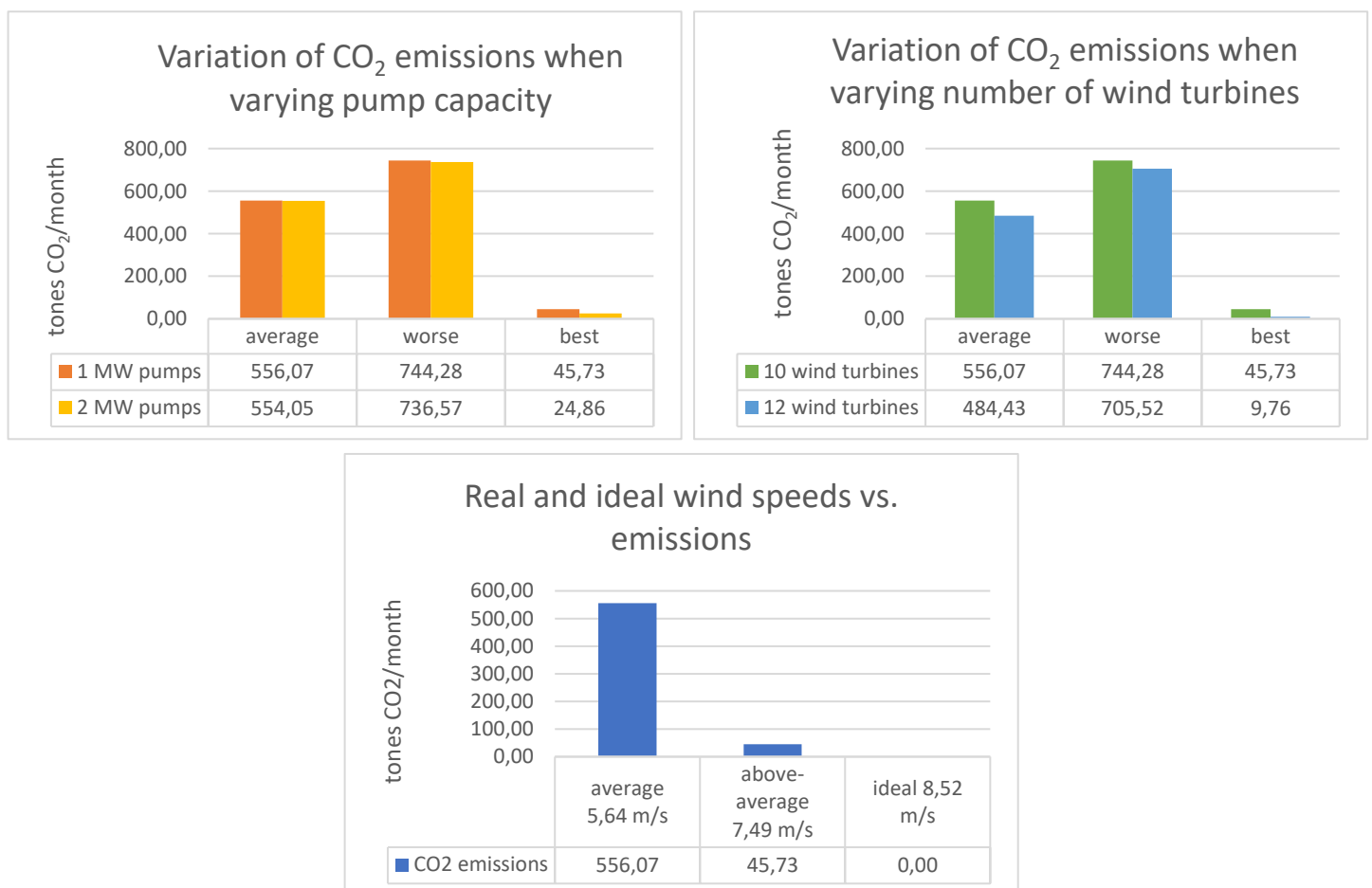
Pumped Hydroelectric Energy Storage (PHES) is the most used bulk Electric Energy Storage (EES) technology with a global installed capacity of 130 GW. This technology combined with wind power creates a power technology named hybrid wind-hydro. A study case on a hybrid wind-hydro power plant is presented, analyzing in detail 2 different cases in which the plant can operate (with excess wind and with no wind). In the first case, the pump group will play the central role, being able to achieve a head of 200 m for the storage of the excess wind in the upper reservoir. A mathematical model is developed for centrifugal pumps using the pump NK 32-125/142 from Grundfos for such purpose. Lab tests are performed using this same pump to collect data for model validation. The impeller of the Grundfos pump has been optimized based on the mathematical model. Lab tests are conducted also for the new impeller to verify the optimization (despite not being presented in this report). Finally, the optimized impeller is up-scaled to suit the requirements of a 1 MW pump which can be used in the hybrid wind-hydro power plant. This last step will verify that the mathematical model is suitable for pumps of diverse size and application.

By accepting the request from the fellow student who uploads the study group's project report in Digital Exam System, you confirm that all group members have participated in the project work, and thereby all members are collectively liable for the contents of the report. Furthermore, all group members confirm that the report does not include plagiarism.

i. Summary

This project consists in a Final bachelor project elaborated by a student at Aalborg University in the spring semester of 2017. The project has been approached to respond to the following problem statement: **How can a hybrid wind-power power plant be dimensioned to be able to predict its behavior under given wind conditions? Are small-scale optimized models viable for large-scale hydro storage pumps?**

This project addresses two separate but related subjects. Firstly, the technology of wind-hydro power plants is looked into. This allows to elaborate a template that enables to predict the performance, functioning and environmental impact of the power plant under given wind conditions. The feasibility of a project of this kind is examined, choosing the island of el Hierro as a study case. Of course, such installation is based on hydro-storage energy which relies on electricity absorption by pumps to store water and electricity production by turbines. This is the meeting point between the two subjects. The conclusion of this part is that hybrid wind-hydro power plants are only environmentally feasible in insular systems with average wind speeds of around 8.5 m/s. The greatest influence on the savings of CO₂ emissions from the diesel engine comes from the wind resource, the amount of wind power and lastly the pumping capacity of

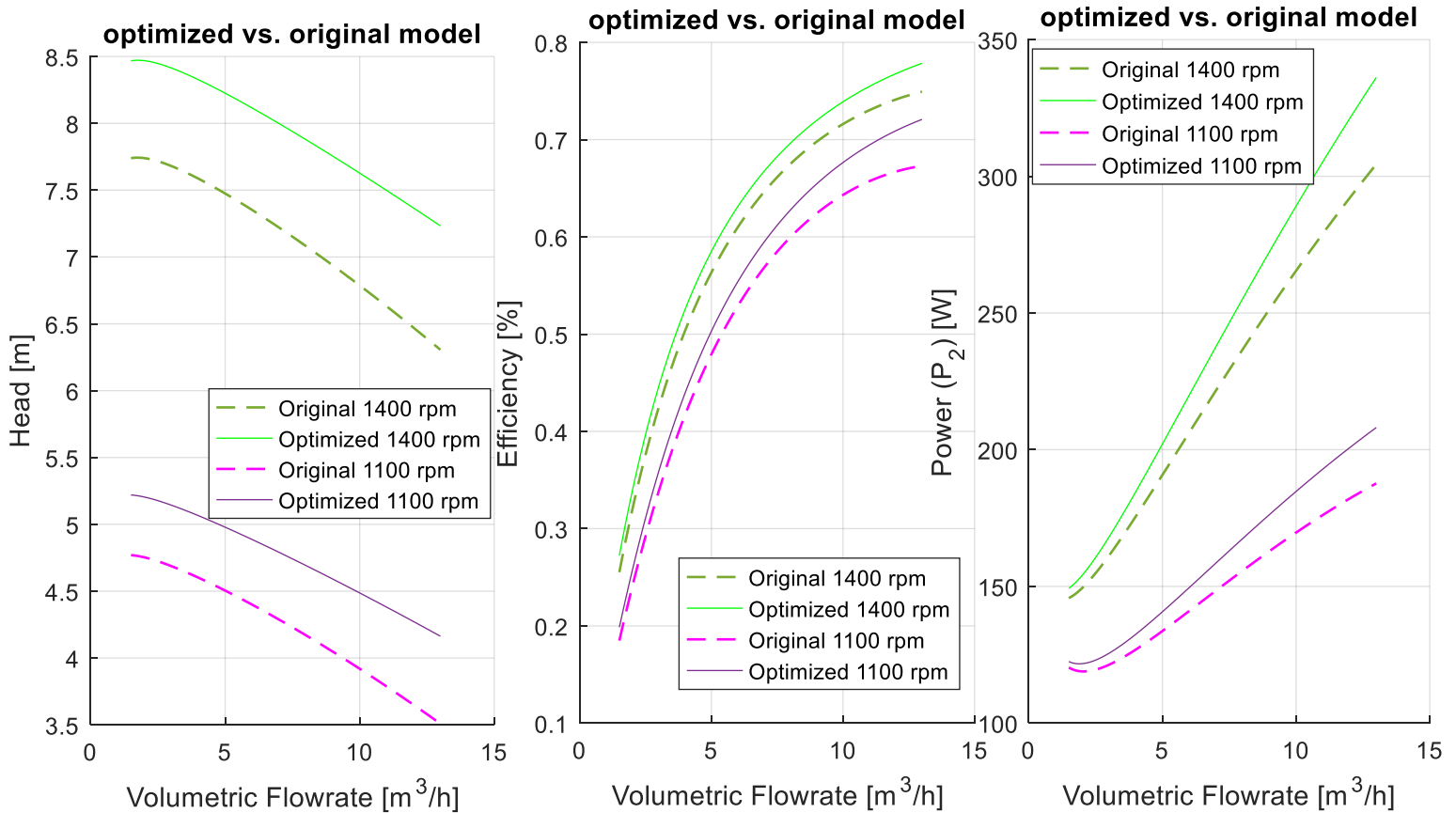


Graph 1-1 Effect of varying the pump capacity, the installed wind power or wind resource on the CO₂ emissions

the pump group. For all the approaches, 3 scenarios have been contemplated; one with average wind, one with above average wind (best) and one with below average wind (worse).

The second part approaches the modeling and optimization of a pump's impeller. The modelling is done using an existing impeller from Grundfos (NK 32-125/142). The performance of the mathematical model for the Grundfos impeller is compared to the test results obtained from the same pump in the lab. Additionally, also the points from the Grundfos data-sheet are plotted for major concretion.

Using the before mentioned plots, the mathematical model is fitted and validated. This fitted model is later used for optimization purposes. The optimization is done to achieve a higher head and efficiency at high flow rates. This objective is set bearing in mind that this optimization



Graph 1-2 Change seen in the pump characteristics before and after optimization

would also benefit a large-scale pump for hydro-storage use. The optimization results with a new impeller which in fact has higher head and efficiency in all the range of flows but most notably at high flow rates. This has a repercussion in the power consumption of course. The optimized geometrical parameters are listed in Table 1-1.

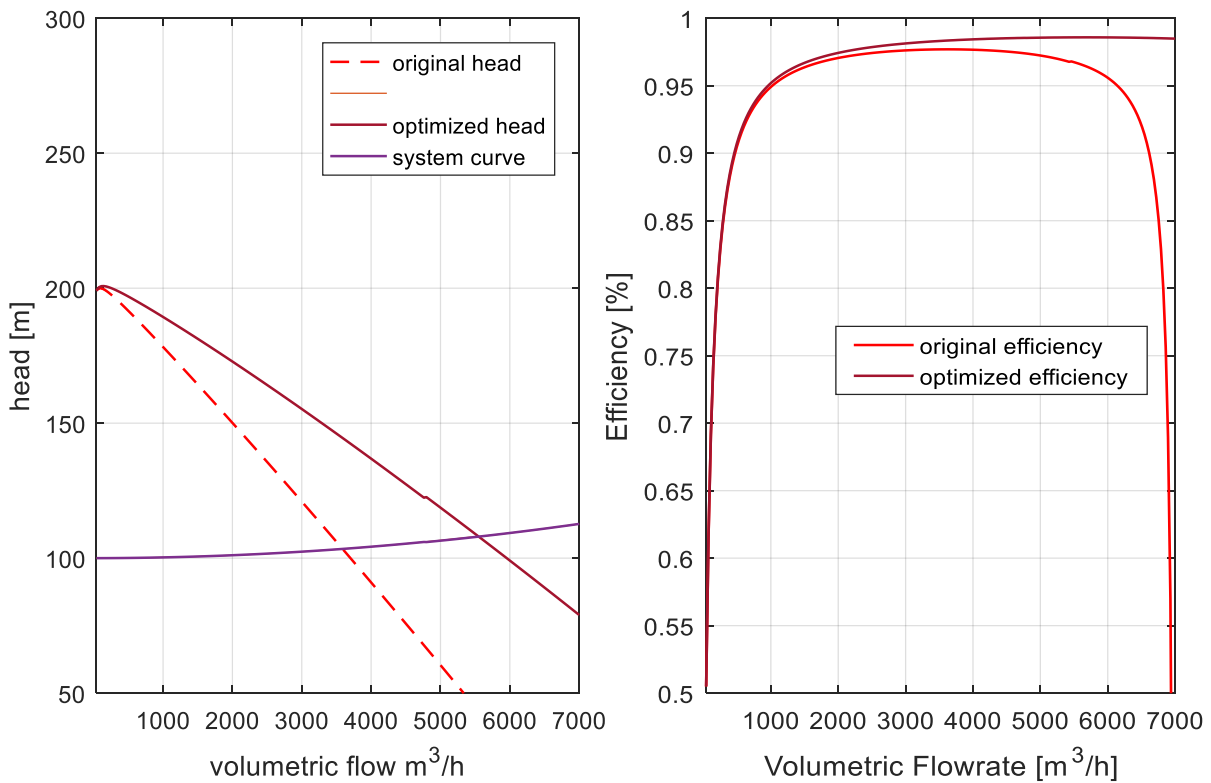
| Description | Symb | Initial | Final | unit |
|-----------------------------------|-----------|---------|-------|--------|
| Outlet blade angle | β_2 | 27.28 | 30 | ° |
| Thickness of the blades at inlet | e_1 | 2.17 | 1.75 | mm |
| Thickness of the blades at outlet | e_2 | 3.47 | 2.8 | mm |
| Number of blades | Z_{La} | 5 | 9 | blades |

Table 1-1 Optimized geometrical parameters of the impeller

Lastly, the model is used to predict the pump performance of a large-scale pump. The main geometrical traits for a 1 MW pump are calculated and used in the model. For major correlation between the small impeller and the large impeller, the optimized values obtained for the small

one is used in the large-scale model to evaluate their feasibility at larger scales. The optimizations used in the large-scale impeller are limited to the number of blades and the outlet blade angle since the blade thickness requires individual dimensioning for the large pump ergo the same values cannot be taken.

The optimization meets its mission in the large pump too, at expense of giving a common operating point with the system that is displaced to the right involving more head and more flow (see Graph 1-3).



Graph 1-3 Q-H and Q- η for the large scale impeller with and without optimization

ii. Nomenclature

| Symbol | Description | Units |
|----------------------|---|---------------------|
| d_1/d_2 | Inner/outer diameter of the impeller | [m] |
| ΔH_{sp} | pressure difference across the seal | [m] |
| a_1/a_2 | Distance between the vanes at inlet/outlet | [m] |
| b_1/b_2 | Blade height at inlet/outlet | [m] |
| C | scaling parameter or characteristic velocity of the wind | [-] |
| C_{2r}' | Corrected radial velocity at the outlet | [m/s] |
| c_{ax} | axial velocity of the fluid inside the gap | [m/s] |
| C_d | dimensionless number for calculation of friction losses | [-] |
| C_f | Dimensionless coefficient for calculation of disk losses | [-] |
| C_{r1} | Absolute radial velocity at the inlet | [m/s] |
| C_{r2} | Absolute radial velocity at the outlet | [m/s] |
| C_{t1} | absolute tangential velocity at the inlet | [m/s] |
| C_{t2} | absolute tangential velocity at the outlet | [m/s] |
| D | Diameter of the pipe | [m] |
| d_{1i} | inside diameter of the bottom part of the blade | [m] |
| d_{1m}^* | dimensionless number for calculation of slip | [-] |
| D_h | hydraulic diameter | [m] |
| d_{sp} | Radial distance to the gap through where the leakage goes | [m] |
| e_1/e_2 | Thickness of the blades inlet/outlet | [m] |
| f | Pipe friction factor | [-] |
| g | Gravitational acceleration | [m/s ²] |
| H | head | [m] |
| $H_{fric_impeller}$ | Height losses due to flow friction in the impeller | [m] |
| H_{fric_volute} | Height losses due to flow friction in the volute | [m] |
| h_1/h_2 | Height at point 1/2 | [m] |
| $H_{contract}$ | Height losses due to contraction | [m] |
| $h_{cylinder}$ | height of the cylinder | [m] |
| H_{exp} | Height losses due to expansions | [m] |
| h_f | Friction losses with the pipe walls | [m] |
| $H_{loss'}$ | Height loss due to ' ' phenomena | [m] |
| H_{losses} | Height losses = Shock losses, contraction & expansion losses, friction losses, recirculation losses | [m] |
| h_o | Intial height of reservoir | [m] |
| H_p | Pressure drop | [m] |
| H_{real} | Pump head including losses | [m] |
| H_{recirc} | Height losses due to recirculation | [m] |
| H_{shock} | Height losses due to shock | [m] |
| $H_{theoric}$ | Ideal pump head | [m] |
| j/l | dimensionless number for calculation of slip | [-] |

| | | |
|--|--|------------------------|
| k | Rotation factor for calculation of leakage | [-] |
| k_v | shape parameter of the Weibull function | [-] |
| k_w | Coefficient for the influence of the inlet diameter on the slip factor | [-] |
| L₁/L₂ | Angular momentum at inlet/outlet | [kg·m ² /s] |
| L_{disk} | circumference of the impeller. | [m] |
| L_{eq} | Equivalent length of the pipe | [m] |
| L_{sch} | the length of the impeller channel | [m] |
| L_{sp} | Length of the gap through which leakage goes | [m] |
| m[·] | Mass flowrate $\dot{m} = \rho \cdot Q$ | [kg/s] |
| n | Rotational speed | [rpm] |
| n_q | Specific rotational speed | [rpm] |
| η_{hyd} | Hydraulic efficiency | [%] |
| η_p | Pump efficiency | [%] |
| n_{ref} | reference rotational speed which equals 1500 rpm | [rpm] |
| η_t | Turbine efficiency | [%] |
| P_{cylinder,loss} | Power losses due to friction with the cylinders | [W] |
| P_{plate,loss} | Power losses due to friction with the plates | [W] |
| p₁/p₂ | the pressure of Point 1/2 | [Pa] |
| P₂ | Shaft power | [W] |
| P_{disk} | Power loss due to disk friction losses | [W] |
| P_{fluid} | Power absorbed by the fluid | [W] |
| P_{hydr} | Power loss due to hydraulic losses | [W] |
| P_m | Power loss due to mechanical loss | [W] |
| P_{opt} | shaft's power at the BEP | [W] |
| P_{recir} | Power losses due to recirculation | [m] |
| P_{shaft} | Shaft power | |
| Q_{BEP} | Volumetric flow at the best efficiency point | [m ³ /s] |
| Q_{impeller} | Volumetric flow through the impeller | [m ³ /s] |
| Q_{leakage} | Leakage volumetric flow | [m ³ /s] |
| Q_{pump} | Volumetric flow through the pump | [m ³ /s] |
| Q_{ref} | Reference volumetric flow which equals 1 m ³ /s | [m ³ /s] |
| r₁/r₂ | radius of the inlet/outlet | [m] |
| r_{cylinder} | radius of the cylinder | [m] |
| r_{outerplate}/r_{innerplate} | outer radius of the plate/inner radius of the plate | [m] |
| Re | Reynolds number | [-] |
| Re_u | Reynolds number with radial and circumferential speeds | [-] |
| s | width of the gap through where the leakage flow goes | [m] |
| S | swept area by the rotor | [m ²] |
| T | Torque | [Nm] |
| U₁ | blade velocity at the inlet | [m/s] |
| U₂ | blade velocity at the outlet | [m/s] |
| u_{sp} | Velocity for calculation of leakage loss | [m/s] |
| V | Volume | [m ³] |
| v₁/v₂ | fluid's speed at Point 1/2 | [m/s] |

| | | |
|---------------------|---|----------------------|
| W_{1r} | Radial relative velocity at the inlet | [m/s] |
| W_{1t} | Tangential relative velocity at the inlet | [m/s] |
| $W_{1throat}$ | Relative velocity at the inlet of the impeller channels | [m/s] |
| W_{2r} | Radial relative velocity at the outlet | [m/s] |
| W_{2t} | Tangential relative velocity at the outlet | [m/s] |
| w_{av} | average relative velocity at the impeller's channels | [m/s] |
| γ_{sp} | Dimensionless coefficient for calculation of leakage | [-] |
| z_0 | length of rugosity in the normal direction of the wind | [m] |
| Z_{La} | Number of blades | [-] |
| α | kinetic energy correction factor | [-] |
| α_1/α_2 | Flow angle at inlet/outlet | [°] |
| β_1/β_2 | Inlet/outlet blade angle | [°] |
| β_{2B} | the ideal relative outlet angle= β_2 | [°] |
| γ | Slip factor | [-] |
| ϵ | rugosity of the pipe's/impeller's interior | [m] |
| ζ_{EA} | loss coefficient in inlet and outlet | [-] |
| ζ_K | loss coefficient per chamber | [-] |
| λ | friction coefficient for the gap | [-] |
| λ_{LA} | Inclination of the impeller's blade at the outlet | [°] |
| μ | fluid's dynamic viscosity | [kg/(m·s)] |
| ν | fluid's kinematic viscosity | [m ² /s] |
| ξ | Loss coefficient | [-] |
| ϖ | tangential velocity of the impeller | [m/s] |
| ρ | Fluid's density | [kg/m ³] |
| τ_2 | Blade blockage factor | [-] |
| ϕ | Loss factor | [-] |
| ϕ_2 | Dimensionless coefficient for slip calculation | [-] |
| ω | Rotational velocity | [rad/s] |

iii. Preface

This report has been elaborated during the period of 02/Feb-09/June as a final bachelor Thesis by a student from thermal energy engineering at AAU. The material used for the testing was provided by the university. The purpose of the project is to optimize the impeller of a centrifugal pump for later use in large scale installations for hydrostrage, as well as the dimensioning of the mentioned hydrostorage installation. Aside, from the main purpose, also a generic Excel template is elaborated to calculate the main functioning parameters of a hybrid wind-hydro plant.

For the understanding of this report a level of knowledge in turbomachinery, thermofluidodynamic generation and fluid mechanics is required.

Collaboration with another group (TE6-600) in this report

The two groups TE6-600 and TE6-601, have some common objectives and tasks in their projects. That is why both the groups have collaborated to some extent. More specifically, TE6-600 project mainly focuses on the development of the mathematical model for the design and optimization of an impeller for centrifugal pumps, lab testing of the pump's performance with a standard impeller and with an optimized one, both to collect data to validate the model and to verify the optimization. TE6-601 project aims to develop a reliable mathematical model for design, optimization and up-scaling of impellers for large-scale centrifugal pumps which can be used in a hybrid wind-hydro power plant. So, the model development part is done under close collaboration of the two groups. All the test results used for fitting and validating the model are from group TE6-600. The model-based optimization and parametric study is also performed somehow under collaboration of the two groups. The results interpretation and discussion are done independently by the two groups. The hybrid wind-hydro plant and the up-scaling are unique in this report.

-wo groups TE6-600 and TE6-601 have been working in this project proposal having the groups similar objectives in the report. Therefore, this report includes the results of the laboratory work that group TE6-600 obtained, hence this report doesn't include any details about how to obtain the measurements. The test results have been shared. The modelling of the pump was also made in collaboration of both groups. The analysis of the laboratory results, theoretical work and further conclusion have been elaborated separately.

Reading instructions

The report is divided into two very clearly defined parts; the dimensioning of the hybrid wind-hydro plant and the optimization of the impeller. This two parts are later put in common to reach the final objective of the project.

All the references are done following the Harvard Standard Method (Author,Year). A list of references is included at the end of the report.

Figures, tables or graphs include a brief description of what they are showing, together with the source they were taken from.

The appendixes are structured in order of appearance in the main report. Appendix 1 includes all the mathematical developments cited during the report. Appendix 2 contains tables, graphs and figures mentioned along the report.

iv. Table of content

| | | |
|-----------|---|----|
| Chapter 1 | Introduction..... | 1 |
| Chapter 2 | Problem statement | 3 |
| 2.1 | Problem definition | 3 |
| Chapter 3 | Dimensioning of the wind farm and hydroelectric storage | 4 |
| 3.1 | Location and demographics | 4 |
| 3.2 | Wind resource and secondary aspects | 5 |
| 3.3 | Hydroelectric storage..... | 8 |
| 3.4 | Electric demand in the island | 10 |
| 3.5 | Design of the template..... | 11 |
| 3.6 | Chosen dimensions for the hybrid plant | 13 |
| 3.7 | Study cases | 15 |
| 3.8 | Conclusion on Part 1 | 17 |
| Chapter 4 | Pump modelling | 19 |
| 4.1. | Velocity triangles in the pump's inlet & outlet | 19 |
| 4.2 | Blade blockage | 21 |
| 4.3 | Slip factor | 22 |
| 4.4 | Pump losses..... | 23 |
| 4.5 | Pump power and efficiency..... | 28 |
| Chapter 5 | Model validation | 29 |
| 5.1 | Fitting of the model..... | 29 |
| 5.2 | Fitted model and experimental results..... | 39 |
| Chapter 6 | Model uncertainty analysis | 46 |
| 6.1 | Geometrical uncertainties in the leakage | 46 |
| 6.2 | Empirical parameter uncertainties in the leakage | 48 |
| 6.3 | Empirical parameter uncertainties in losses | 49 |
| 6.4 | Impacts of different models for slip factor | 51 |
| Chapter 7 | Optimization in the impeller's design | 52 |
| 7.1 | Number of blades Z_{La} | 54 |
| 7.2 | Blade angle β_2 | 55 |
| 7.3 | Blade outlet thickness e_2 | 56 |
| 7.4 | Blade height at the outlet b_2 | 58 |
| 7.5 | Variations in the inlet parameters | 58 |
| 7.6 | Final design..... | 59 |

| | | |
|--------------|--|-----|
| Chapter 8 | Up-scaling of impellers for the centrifugal pumps in the hybrid wind-hydro power plant | 61 |
| 8.1 | Uncertainties in the scaled geometrical parameters | 63 |
| 8.2 | Conclusions part 2 | 63 |
| Chapter 9 | Conclusion | 65 |
| Chapter 10 | Future work | 70 |
| 10.1 | User interface | 70 |
| 10.2 | PIV tests for a better understanding of the impeller flow | 70 |
| 10.3 | Testing of the optimized impeller | 70 |
| 10.4 | Optimization of large-scale impellers | 70 |
| Chapter 11 | Appendix 1 | 71 |
| 11.1 | Calculations for the hydro storage | 71 |
| 11.2 | Inlet velocity triangle | 75 |
| 11.3 | Outlet velocity triangle | 77 |
| 11.4 | Euler's pump equation | 77 |
| 11.5 | Blade blockage | 79 |
| 11.6 | Slip | 80 |
| 11.7 | Mechanical losses | 84 |
| 11.8 | Hydraulic losses | 84 |
| 11.9 | Calculation of geometrical dimensions | 97 |
| 11.10 | The Weibull distribution | 102 |
| 11.11 | The Betz law | 107 |
| Chapter 12 | Appendix 2 | 110 |
| 12.1 | Maps of the island of el Hierro | 110 |
| 12.2 | Wind roses | 113 |
| 12.3 | Data of the wind turbine | 115 |
| 12.4 | Data for the hydro storage dimensioning | 116 |
| | | 116 |
| 12.5 | Parameters of the pump | 118 |
| Bibliography | | 119 |

Chapter 1 Introduction

Centrifugal pumps are the most common type of pump operating nowadays. They have diverse configurations available and because of the simplicity of their design, the high range of heads achievable and the high efficiency they are perhaps the most manufactured pumps. According to statistics, pump's energy consumption accounts for nearly 22% of the world's energy used by electric engines, so they can have a great saving potential (Wang, et al., 2016)

These pumps are used in oil refineries, municipal water applications and so on. They are also used for hydroelectric storage, as investigated in this report.

Hydroelectric storage technology consists in a hybrid wind power plant which combined with a hydroelectric plant, it stores energy in off-peak hours and releases water in peak hours. They are commonly known as hybrid wind-hydro power plants. In determined locations in which wind power and hydroelectricity are feasible, implementing hybrid wind-hydro power plants is becoming a more considered option given the maturity of both technologies and the fact that

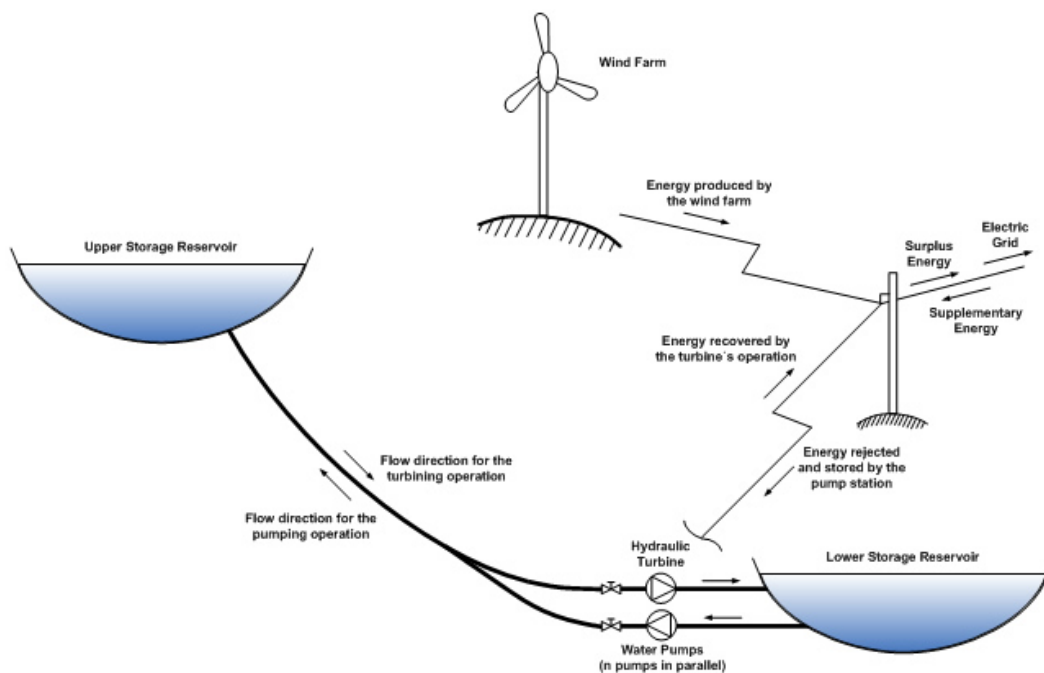


Figure 1-1 Representation of a hybrid wind-hydro power plant

relying on two different technologies gives the system greater dynamism. Hydroelectric storage has geographic limitations but economically talking it is a far cheaper storage technology than flow batteries. Hydraulic plants have a very high efficiency in a complete cycle around 70-80% and a very quick response time. These plants can be dimensioned as reversible pump-turbine plants or with a duplicated hydraulic circuit with a pump and a turbine. This report talks about the second type more in detail.

One of the main inconveniences with hybrid wind-hydro power plants is that there's a risk that the upper reservoir becomes empty and the wind farm is not producing any electricity. For these extreme situations, the project will count on auxiliary biomass engines.

For the dimensioning of the wind park with hydraulic storage, the variable data will consist in the wind speed and the energy demand. The water height of the water tank will also vary and therefore the pumped or turbined energy too.

Since wind data should be analyzed hour by hour to have the most accurate possible results, the template will be designed for a period of 1 month.

A model of wind turbine should be chosen to obtain the power curve according to the different wind speeds. We will then have an energy demand (also model) that will change hour to hour. With the two numbers, we can already calculate the excess or deficiency of energy. When we have excess energy, we will use it to pump water upwards. When there's an energy deficiency we will turbine the water backwards into the inferior water tank. The pumped-turbined energy is limited to the dimensioning of these two parts. So, given the situation that we have to pump more energy than the pump group can afford, the maximum pumping capacity will be the one fixed by the pumping groups. In the opposite situation in which there's no wind to cover the energy demand and that the turbines cannot turbine enough water, we will have to take hand of the diesel engines.

This report will therefore focus on the centrifugal pump used in the system. Pump failure in this type of system can lead to undesirable consequences. Therefore, the aim of this report will be to develop a general model for an impeller that will then be optimized to increase the efficiency of the excess electrical power used. Lab-testing will be performed to validate the model. Once validated, the optimized design of the impeller is later going to be scaled to applicable dimensions through similarity laws and geometrical similitude for its use in the hydro storage plant.

Chapter 2 Problem statement

As mentioned previously, hybrid wind-power power plants are a good alternative for electricity production and storage. There are cases in which this system has been implemented successfully in insular systems to cover the island's electrical demand (Island of El Hierro, Canarias).

How can a hybrid wind-power power plant be dimensioned to be able to predict its behavior under given wind conditions? Are small-scale optimized models viable for large-scale hydro storage pumps?

2.1 Problem definition

In order to elaborate a study case which is near to reality, the hybrid power plant is dimensioned using data from the island of El Hierro.

Regarding the impeller design, the results and plots obtained from the model is also to be compared and contrasted to the measurings provided by the test-rig as well as the test-points provided by the manufacturer. The pump that is tested is Grundfos NK 32-125 which comes with three impellers of different sizes.

The optimized impeller will be scaled to suit the requirements of a large centrifugal pump.

Chapter 3 Dimensioning of the wind farm and hydroelectric storage

The island of El Hierro has been chosen as a sample location to study the feasibility of this kind of installations given the great amount of information available about the general topography of the island, its energetic demand and wind data.

How the hybrid power plant is going to be dimensioned and the operating idea of such installation is examined in detail in chapters 3.5 and 3.6.

Two concrete calculation cases are examined more in detail:

Case 1

The hybrid power plant receives a lot of wind and therefore it has excess wind power. The pump will have to come into operation to pump water from the lower reservoir to the upper reservoir for energy storage

Case 2

The power plant is not receiving enough wind to be able to supply all the electric demand of the Island and therefore the upper reservoir will be emptied to turbine water to create electric energy.

In order to understand the different calculation steps, there's some important background to be looked at since the hybrid power plant will be located at a concrete site. Both wind energy and hydroelectric energy will be looked into in more detail in the following two sections.

3.1 Location and demographics

The island of el Hierro is located in the Atlantic Ocean. It is the most meridional and occidental of the islands in the Canary archipelago.

GENERAL INFORMATION

| | |
|----------------------|------------------------|
| Surface area | 268.71 km ² |
| Highest point | 1501 m |
| Population | 10587 |
| Coordinates | 27° 45'N 18°00'O |

General topography

This volcanic island contains a mountain range that crosses it from east to west. All the coastal line is formed by abrupt cliffs. From all the Canary Islands, el Hierro has the most protected area of them, a 58% of the island is protected by the Canarian network of protected natural regions.

The major part of the population is concentrated in 3 cities; Valverde, La Frontera and El Pinar del Hierro (from bigger to smaller)

3.2 Wind resource and secondary aspects

All the Canary Islands receive not very extreme winds. They do have indeed a very high potential for off-shore wind power as it can be seen in Figure 3-1. The maximum onshore winds in the island reach the 9.5 m/s which is not a very impressive magnitude.

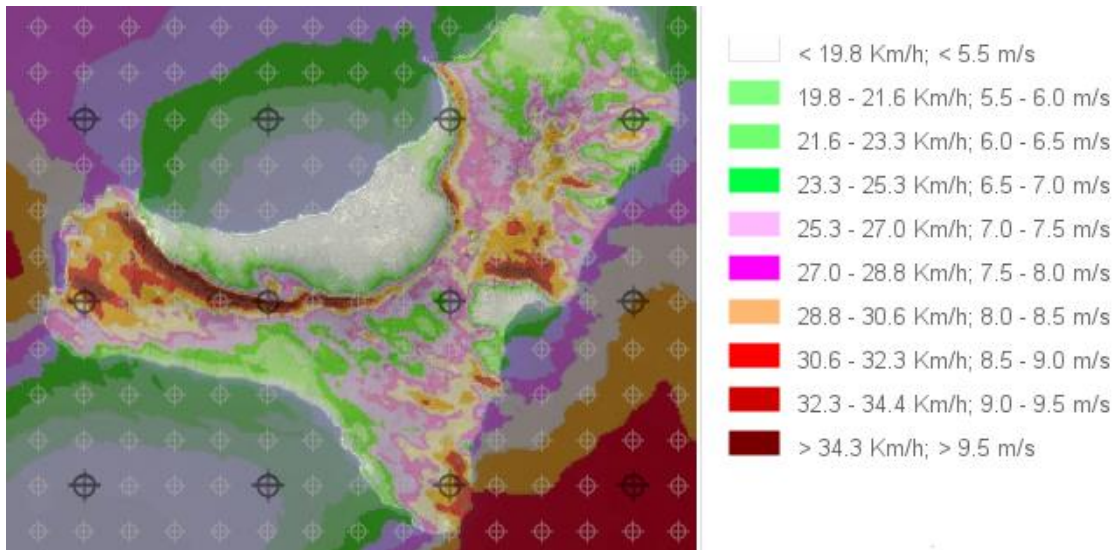


Figure 3-1 Wind speed map of the Island. Source: (Anon., 2017)

In order to determine the most suitable location for the wind farm we must take into account the following considerations:

- Wind speed at 60 m
- The degree of unevenness of the ground for the waterfall
- Proximity to the electrical substation
- Restricted natural parks
- Geographical accidents which would interfere in the wind profile

Wind speed at 60 m

As it can be seen from Figure 3-1 the windiest areas come along the most western side of the mountain range and in the South-West part of the island. The wind speed is being examined at 60 m above the ground level since the hub height is also 60 m.

Degree of unevenness of the ground

To build the water reservoirs, a considerable water fall is needed. As it can be seen from Figure 12-2 the highest points reach the range between 1201-1500 m and the lowest ones between 0-100 m. Anywhere along the mountain range that crosses the island would be a good location for the upper reservoir.

Proximity to electrical substations

For being such a small island, El Hierro only has one electrical substation (Figure 12-1). This reduces significantly the distance at which we can locate the hybrid power plant to avoid huge

cabling and electrical tower expenses. There must be an interconnecting electrical substation between the hydraulic plant, the pumping plant and the wind farm. This should be placed ideally in the area adjacent to the Llanos Blancos substation, with double bus bar, double switch and attached to the SE of Llanos Blancos.

Restricted natural parks

El Hierro is considered a biosphere reserve since it has a large amount of area covered by rural parks shown in Figure 12-3 Non-buildable areas. Source: (Anon., 2017)Figure 12-3. These areas should of course be excluded from all the location choices the island has.

Geographical features

Geographical accidents like hills have a positive influence in the local acceleration of the wind. For example, a hill with a soft inclination accelerates the wind along the slope giving a maximum speed at the top of it. Instead, a very abrupt cliff dissipates the wind energy due to the turbulences generated. This phenomenon is illustrated in Figure 12-4. In the map from Figure 12-5 it can also be appreciated how the level of turbulences vary at 60 m. It should also be taken into consideration that there are obstacles like trees or buildings. There are two types of obstacles; porous and non-porous. Porous obstacles are those that let the air through partially like trees. Non- porous obstacles don't let the air through like buildings. The rugosity of the terrain (Figure 12-6) influences the wind speed too; the lowest rugosity is present in water environments, while the most rugose surfaces are forests and urban areas.

Chosen location for wind-farm

After examining these different aspects, it can be concluded that the wind farm should be located somewhere in the south-eastern part of the island since it would be near the electrical substation, it wouldn't occupy any natural protected areas, the land doesn't present a lot of geographical accidents, has medium rugosity and some very windy locations. This location receives the name of "Punta de Ajones".

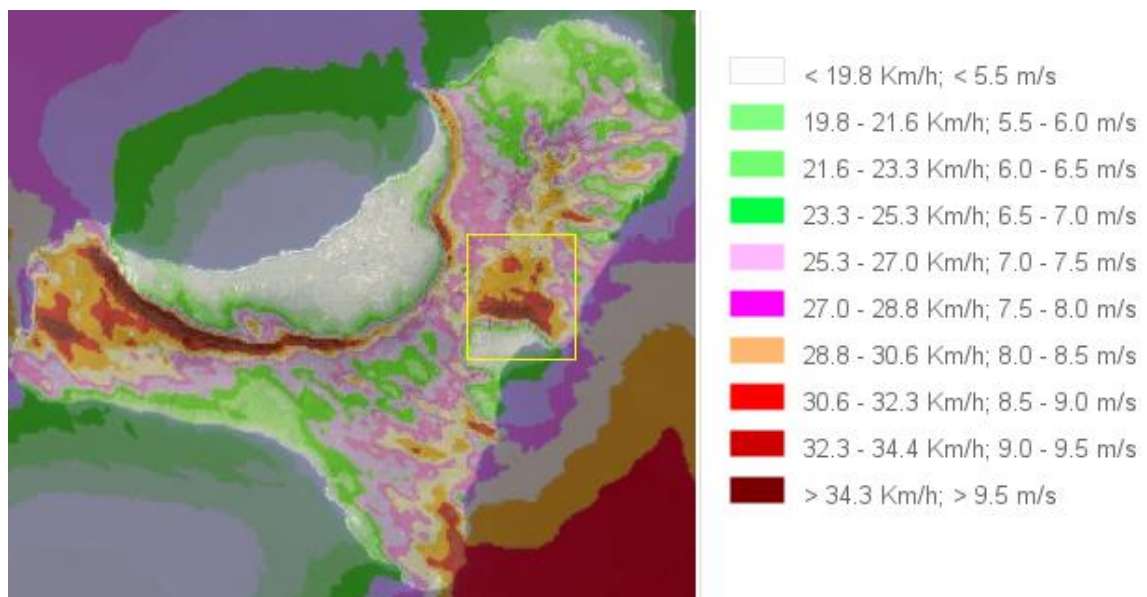


Figure 3-2 South-eastern location of the wind farm.Source: (Anon., 2017)

Data collection (Weibull parameters, Weibull distribution)

The wind presents a seasonal behavior along the year, but it is usually random at short and medium term. Therefore, despite the direction and the wind intensity being stochastic measures (they are subject to random fluctuations), they can be treated by means of statistic variables. The most common way is using a probability distribution with the Rayleigh and Weibull distributions which are described in Appendix 11.10.

The wind rose

Its utility consists in providing the direction or directions with their frequencies in a circular diagram allowing to choose the ideal location of the wind turbines. In case there's not a dominant direction, another wind rose incorporating power production is used to choose the final orientation.

In *Punta de Ajones* the most frequent orientation is NE (see Figure 12-8). More detailed wind roses with monthly measures are included in the Appendix Wind roses.

Wind power. The Betz formula

The Betz law indicates the maximum power that can be extracted from the wind independently from the wind turbine's design. According to this principle, no turbine can capture more than a 59.3 % of the kinetic energy from the wind mainly due to its own geometric limits. Further calculations are carried out in the Appendix The Betz law

Wind power. Power curve

The power curve for the wind turbine indicates the available electrical power it produces at a particular wind speed. This data must be provided by the wind turbine manufacturer. Power curves are based on measures taken on site where an anemometer is placed on a mast that is relatively close to the wind turbine (not on the wind turbine itself since the rotor would create turbulences). If the wind speed is relatively constant, the measures done by the anemometer can be used together with the power production measurements taken directly from the wind turbine to create the power curve. An example power curve appears in Appendix 12.3

Uncertainty is the power curve measurements

The curve consists in a tendency line created from disperse points in a graph. The reason for that is that wind fluctuates and the wind can't be measured exactly though the wind turbine. In practice, an average value for the different measures is taken and the curve is plotted with those averages. If the measures have a $\pm 3\%$ error margin (Association, 2003), this translates to a $\pm 9\%$ variation in the energy production since the energy production varies with the third power of the wind speed (see Eq.(11.11.6))

Selection of wind turbine

The selected wind turbine for this purpose was the Bonus 2300/82.4. This wind turbine has a nominal power of 2.3 MW each. It has its cut-in speed at 3 m/s, and the cut-out speed at 25 m/s. The number of installed wind turbines will be chosen optimally depending on the results of the 2 studied cases

The power curve and data on the wind turbine are shown in Appendix 12.3

3.3 Hydroelectric storage

Bernoulli equation

The Bernoulli equation is always important to remind when speaking about hydraulic energy. The specific fluid energy at point 1 can be expressed in meters of water head as:

$$H_1 = h_1 + \frac{p_1}{\rho g} + \frac{v_1^2}{2g} \quad [m] \quad (3.3.1)$$

Where,

h_1 is the height of Point 1 [m]

p_1 is the pressure of Point 1 [Pa]

v_1 is the fluid's speed at Point 1 [m/s]

The total net head at point 1 is formed by 3 different contributions; potential energy height h_1 , the potential energy pressure $\frac{p_1}{\rho g}$, and the kinetic energy velocity $\frac{v_1^2}{2g}$.

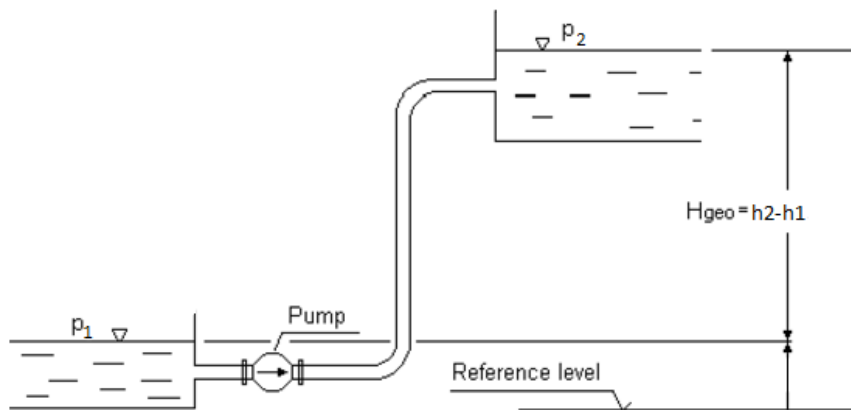


Figure 3-3 Simplified reservoir schematic

The specific energy at point 2 can be expressed in the same way just changing the subscripts. The gross head between these 2 points can be expressed as:

$$H_{12} = (h_1 - h_2) + \frac{p_1 - p_2}{\rho g} + \frac{v_1^2 - v_2^2}{2g} - h_f \quad [m] \quad (3.3.2)$$

Where,

h_f are the friction losses with the pipe walls [m] calculated in Eq.(11.1.3)

Considering the following hypothesis:

- $\Delta v = 0$
- $p_1 = p_2$ normally both reservoirs are open-air
- No pressure losses

We obtain a new equation for the gross head which shows that ideally the only contributions which should count are the ones for potential energy

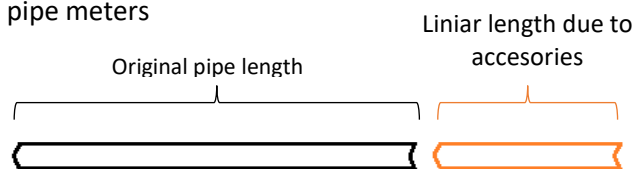
$$H_{12} = h_1 - h_2 \quad [m] \quad (3.3.3)$$

Pressure losses

Pressure losses are originated by the friction exerted by the flow against the walls and the turbulences created by obstacles intercepted by the flow as direction changes, valves or gratings. The calculation of these losses will be necessary for the elaboration of the template. All the necessary equations together with a flow chart on how to elaborate the calculations is included in Appendix 11.1. following the Darcy-Weisbach equation and the Colebrook-White equation.

Secondary losses

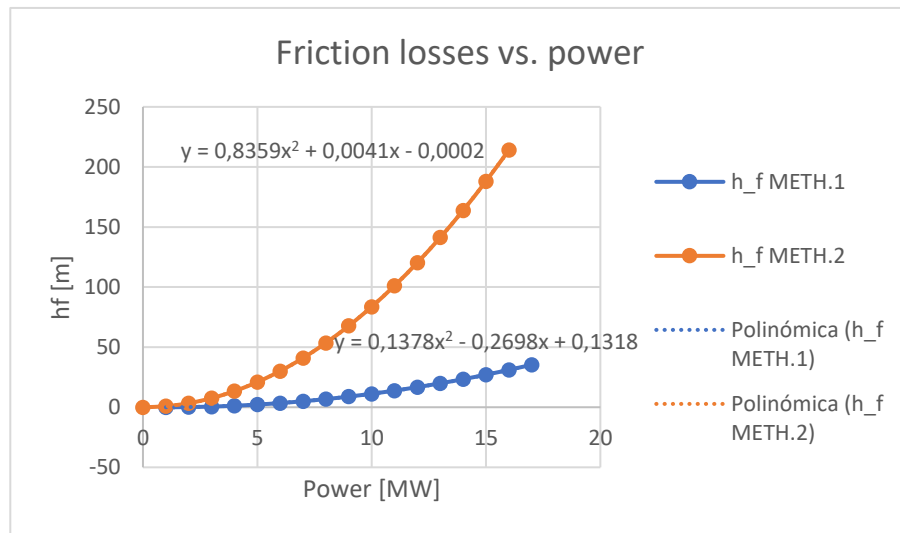
Secondary losses are due to the accessories included in the pipe installation such as bends, valves, contractions, expansions, venturis... These losses are usually expressed in equivalent length of straight pipe meters



One of the suggested methods on how to evaluate which is the corresponding length of each accessory is to use an abacus like the one in Figure 12-10. The central axis indicates the additional meters of pipe that belong to each accessory. The axis to the right indicates the inner diameter of the pipe. When a straight line is drawn from the abacus to the right axis, the crossing point with the central axis will give the additional meters that have to be added to the original length of the pipe (see Eq.(11.1.3))

One other method proposed by (Çengel, et al., 2012) is through geometry-dependent loss coefficients K_L . This second method is explained in detail in Appendix 11.1 in the subsection Method 2: loss coefficient K_L

The result of employing both methods is plotted in Graph 3-1. The second method was further used for the calculations.



Graph 3-1 Relation between power and pressure losses in pipe network.

System curve

Using Eq.(3.3.2) the required pumping head for the flow of an incompressible fluid is determined

$$H_{required} = (h_2 - h_1) + \frac{p_2 - p_1}{\rho g} + \frac{v_2^2 - v_1^2}{2g} + h_f \quad [m] \quad (3.3.4)$$

In circumstances in which both reservoirs are open-air and in which the water at the surface of the reservoir is static, these two elements $\frac{p_2 - p_1}{\rho g}$ and $\frac{v_2^2 - v_1^2}{2g}$ are omitted, leaving this expression which is dependent on the flow Q :

$$H_{required}(Q) = (h_2 - h_1) + h_f(Q) \quad [m] \quad (3.3.5)$$

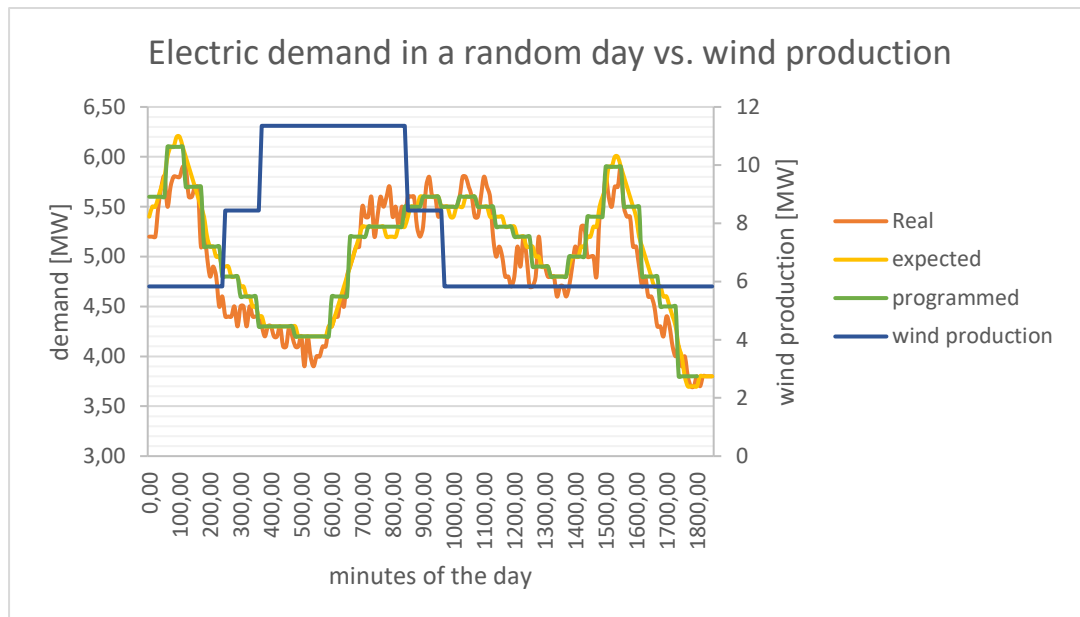
Where,

h_f is calculated in Eq.(11.1.3)

3.4 Electric demand in the island

The electric demand of the Island is the most important number to be considered. In 2015 the annual demand was of 48 GWh. The electric demand is expected to rise a 4% annually up to 2020. Therefore, the reservoirs and the piping should be dimensioned for an annual demand of 58.38 GWh.

The electric demand curve has this particular shape which presents peaks and valleys along the day. The electric demand curve was plotted using 10 min step measures along the day and the wind production curve was plotted using the wind production with hourly averages. As it can be observed the non-coincidence of these 2 profiles is the reason why the hydro storage is going to be needed.



Graph 3-2 Electric demand from el Hierro vs. wind production

3.5 Design of the template

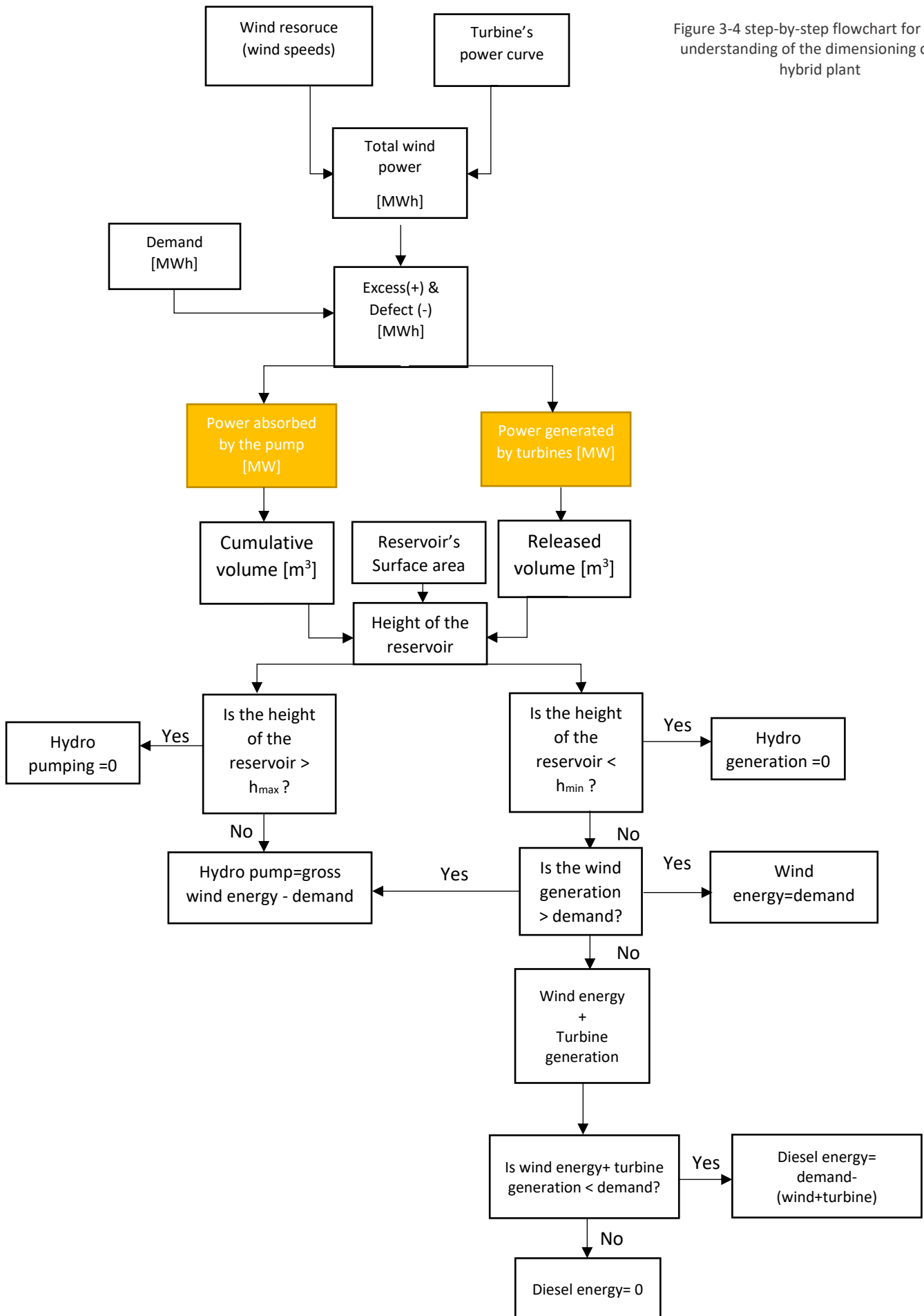
The purpose of this template is to provide a tool for any calculations of a hybrid wind-hydro plant. In order to make the predictions on the functioning the most accurate as possible, wind data for every hour over one month is used. All the input parameters which are marked in red in the excel template attached in the delivery, can be varied at the user's will.

This tool will predict the end results of the functioning of the plant, saying to which extent the island will rely on wind, hydro power or diesel power.

For the design of the template, the most relevant equations were used in the calculation of the released/accumulated volume from the upper reservoir based on the excess/defect power. The equations are listed in Appendix 11.1 together with an explanation on how to use them.

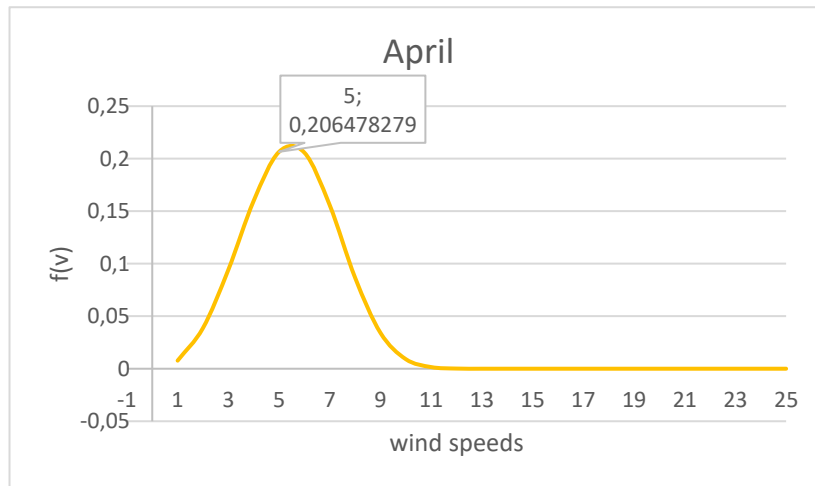
The flow chart from Figure 3-4 consists in the step-by-step procedure that was carried out to elaborate the template for the dimensioning of the hybrid power plant. Despite being the calculations very simple, some calculations require more attention. That is the point marked in yellow in Figure 3-4. For the calculation of the cumulative and the released volume, Eq. (11.1.1) and (11.1.2) must be used. In these equations, there's a height loss due to friction that must be calculated in every step of the template, since as it will be seen in the detailed calculations, this height loss depends on the speed of the flow and the speed depends on the volume that will be pumped or released. How to calculate the friction losses is explained in Appendix 11.1 with Figure 11-1.

Figure 3-4 step-by-step flowchart for better understanding of the dimensioning of the hybrid plant



3.6 Chosen dimensions for the hybrid plant

The dimensioning of the power plant has been optimized in order not to over dimension it or to under dimension it and have a consequent great use of diesel. Therefore, an average month of the year was taken in which the wind speeds weren't either very low nor very high. This selection was done by checking the monthly Weibull distributions and selecting the month which had the most centered curve in the range of [5-9] m/s and which had a frequency between [0.2-0.25]. It is important to prioritize the frequencies rather than the wind speeds. Large wind speeds occurring twice a month will have barely no effect.



Graph 3-3 Weibull distribution for the average month

Under this wind conditions the wind park was equipped with 10 wind turbines (2.3 MW each).

The hydro-storage will have the dimensions illustrated in Figure 3-5

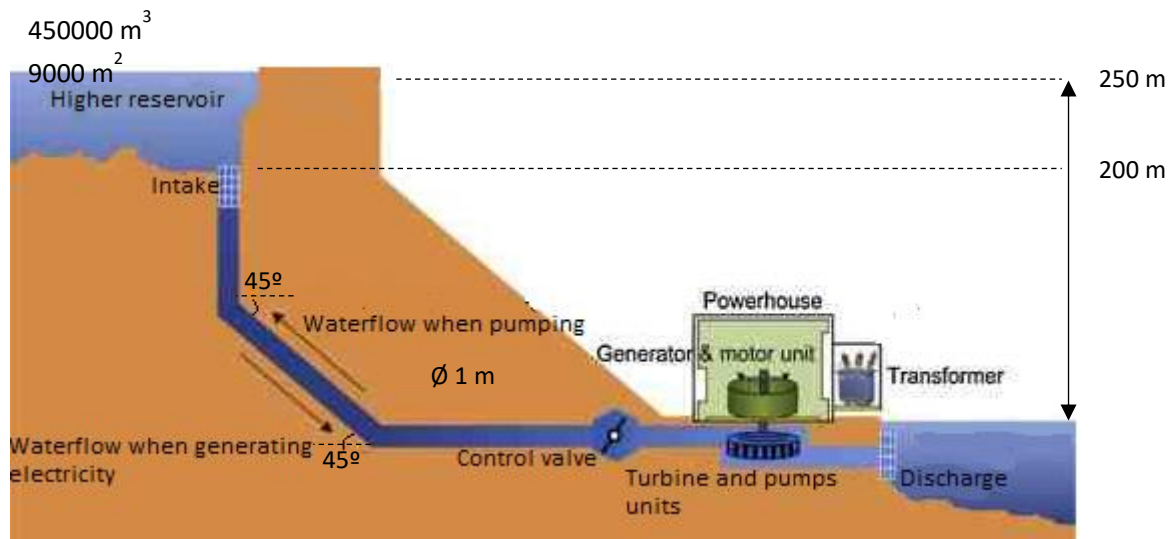


Figure 3-5 Dimensions of the hydrostorage installation

The power house will be equipped with the following groups

| | Units | P_e /unit | Total P_e | η |
|-----------------|-------|-------------------------|-------------|------------------------|
| Pumps | 4 | 1 MW (see Figure 12-11) | 4 MW | 97.69% (see Graph 8-1) |
| Turbines | 2 | 3.5 MW | 6 MW | 90% |

Tabla 3.6-1 Power group for the hydro storage installation

To achieve the head demands and flow demands a parallel-series configuration will have to be used. According to Figure 3-5 and Table 12-2, the head of the higher reservoir is of 200 m and the maximum flow rate is of around $2 \text{ m}^3/\text{s}$. To distribute the flow and the head, the pump group will be set in the configuration from Figure 3-6.

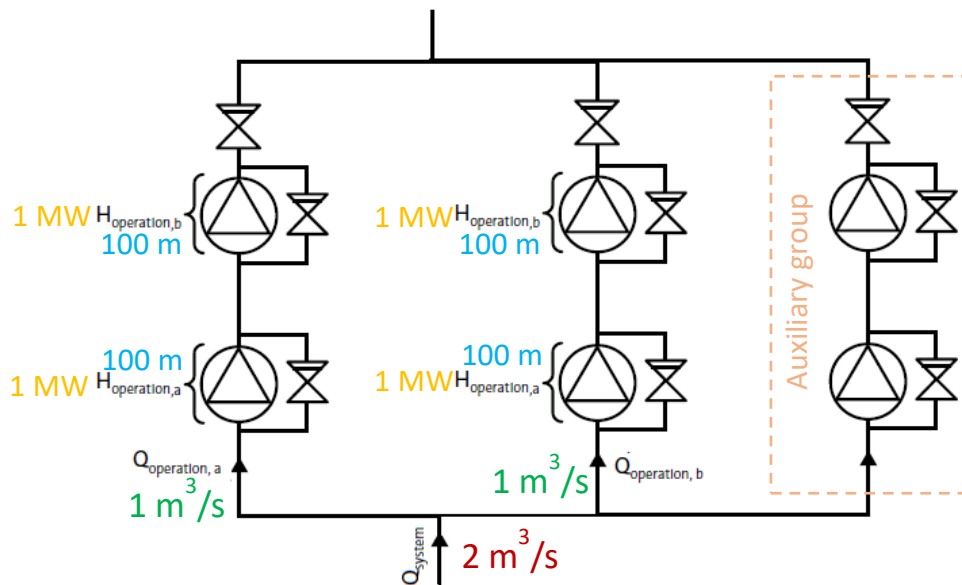


Figure 3-6 Series-parallel configuration for the pumps

The pipe installation will count with the dimensions listed in Appendix 12.4 Table 12-2.

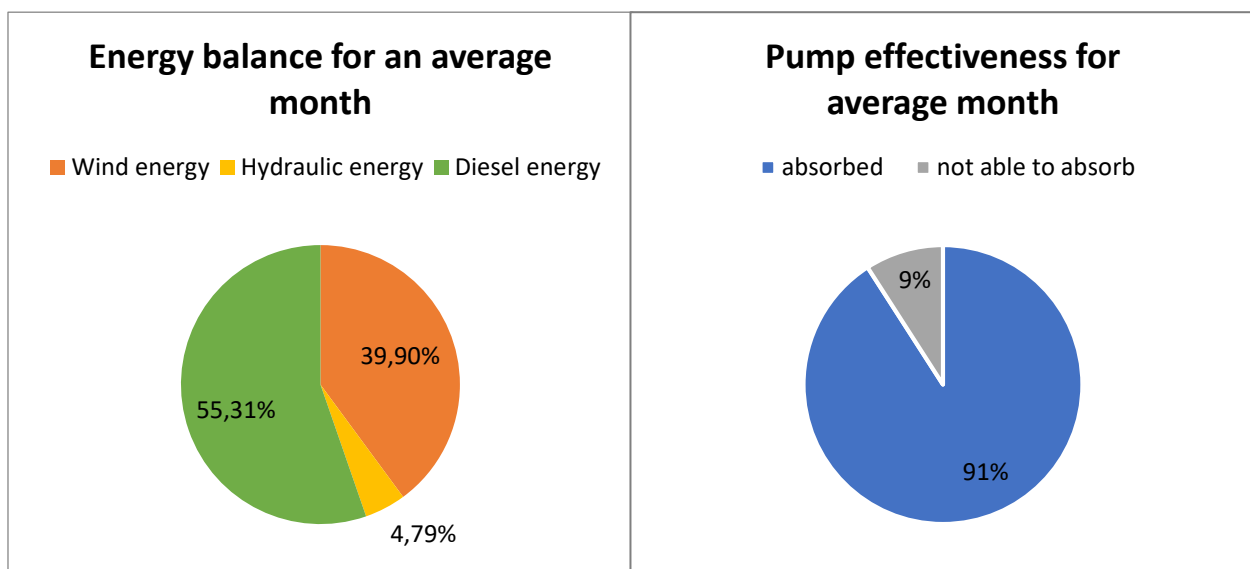
The auxiliary diesel engine will have the dimensions Appendix 12.4, Table 12-3.

3.7 Study cases

Having all the necessary dimensions introduced in the template, the hybrid power plant can be evaluated to see how it behaves and to which extent the auxiliary diesel engine will be required.

Case 0: average

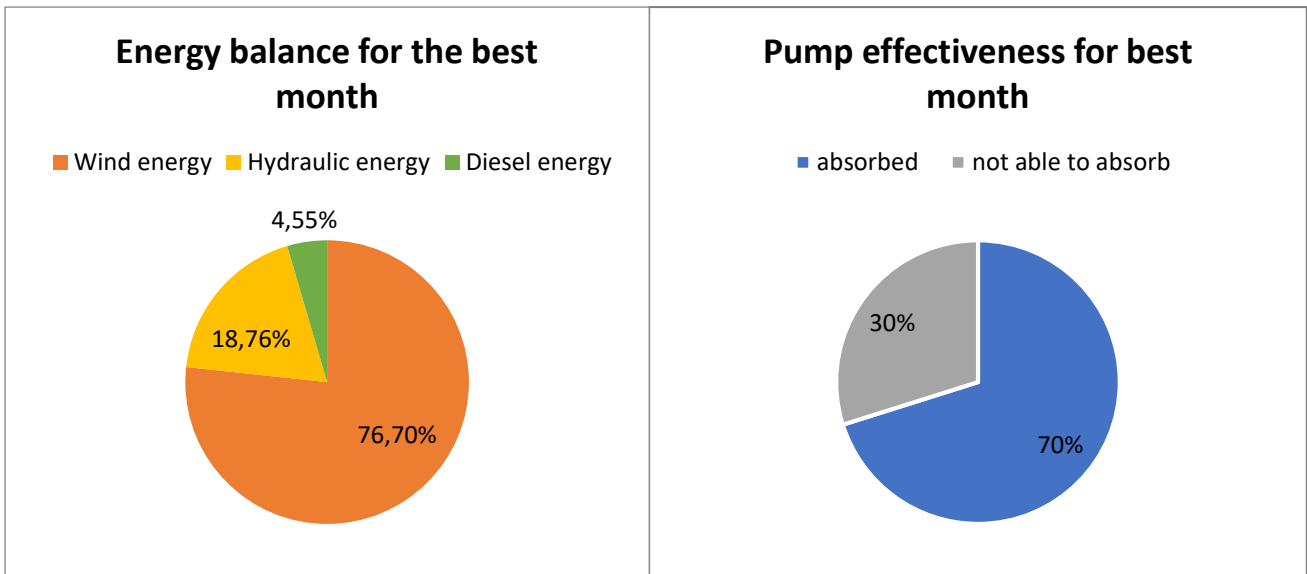
As it is mentioned in subsection 3.6, the average wind conditions for the month of April were used to do the dimensioning of the plant, obtaining the following results regarding the energy source and the effectiveness of the pump. The effectiveness of the pump was evaluated taking the available excess electricity that could have been absorbed by the pump group and the actual electricity that was absorbed by it. As it may be seen, there's a small percentage of electricity that is going to be lost due to the limited capacity of the pump group. The average excess electricity in this case was of 0.3296 MW, having its maximum at 6.55 MW.



Graph 3-4 Energy source distribution and pump effectiveness for the average month

Case 1: above-average

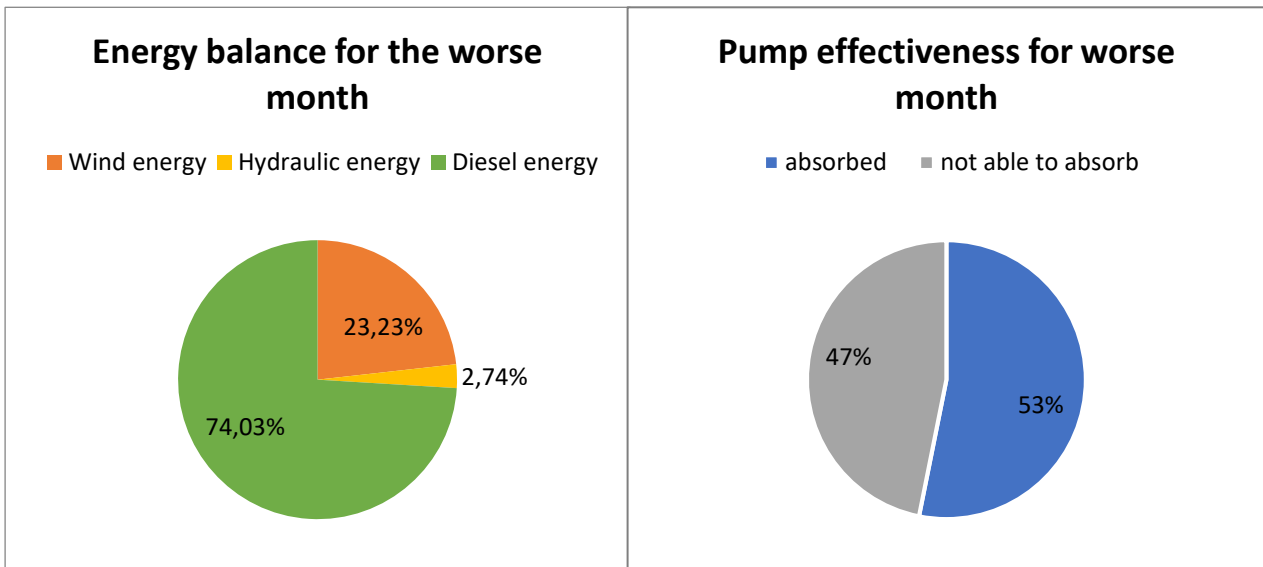
As it can be seen from Graph 3-5, in a month like March, the contribution of the wind clearly makes a difference, increasing at the same time the hydraulic contribution and dramatically reducing the diesel consumption. Despite having more wind, the percentage of hydraulic energy has increased because the upper reservoir was full more often than in the average case, when it was empty 74% of the month and full not even once. In this case, the upper reservoir was empty only an 11% of the month being able to turbine more water. Despite these improvements, the percentage of electricity that the pump is not able to absorb has increased a 21% ,since the average excess electricity is now around 1.61 MW, having its maximum at 15.56 MW (nearly 4 times the available pump capacity), making it harder for the pump to absorb at all times the excess electricity from the wind.



Graph 3-5 Energy source distribution and pump effectiveness for the best month

Case 2: below-average

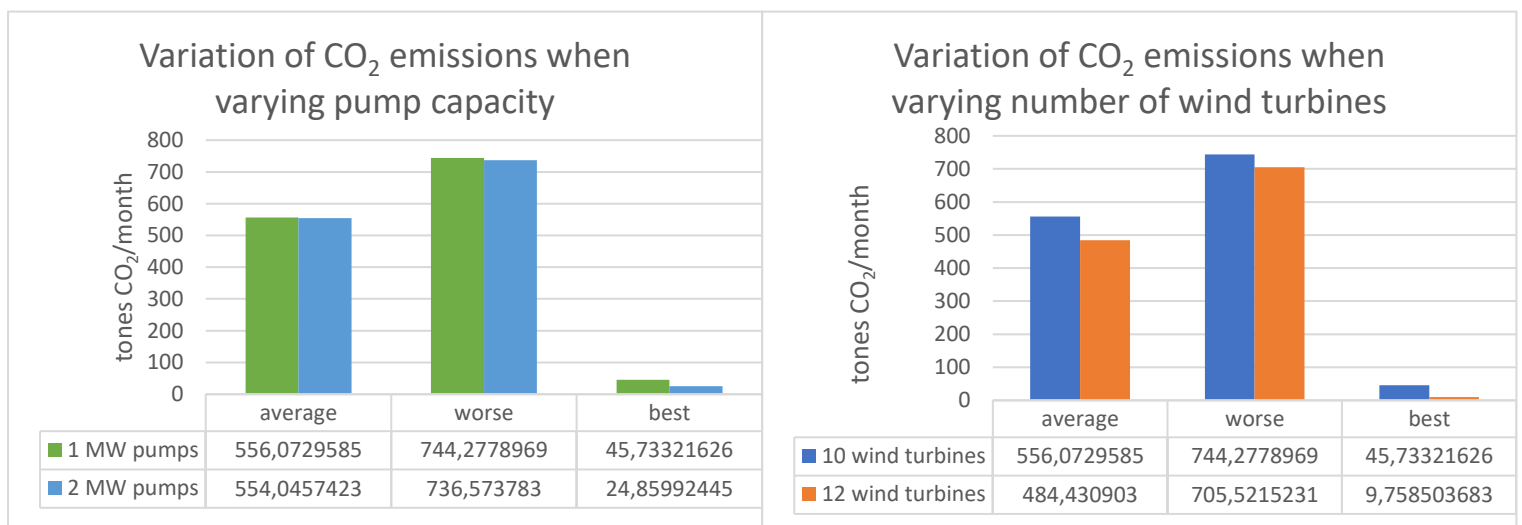
As it can be seen from Graph 3-6, in a month like October, the diesel contribution reached its maximum as it was expected. The upper reservoir was empty 89% of the month reaching a maximum height of 211 m out of 250 available. Regarding the pump effectiveness, it nearly reached a half-half relation close to the relation obtained for the average case in Graph 3-4. The average excess power absorbed by the pump was of 0.37 MW (slightly above the average), reaching a punctual maximum of 16.41 MW (four times the available capacity).



Graph 3-6 Energy source distribution and pump effectiveness for the worst month

Effect of the pump dimensions in the environment

In this section, the environmental impact of the diesel engine will be looked into. Knowing the consumption of diesel every month, the CO₂ emissions have been calculated. The first hypothesis when it comes to reducing the dependency on the diesel engine would be to increase the power of the turbines. This hypothesis ended up not having any repercussion on the CO₂ emissions, since the water that can be turbined depends on the state of the upper reservoir which depends on how much water the pumps have pumped. Therefore, the second hypothesis would be increasing the individual pump capacity from 1 MW to 2 MW (Graph 3-7). This hypothesis ended up having a bigger effect on the windiest case (best case) since there was more excess electricity the pumps could use. In the two other cases the effect was negligible. The third and last hypothesis was to vary the wind generation increasing the number of wind turbines. This hypothesis ended up being the most effective one as it can be seen in Graph 3-7.



Graph 3-7 CO₂ emissions depending on two different hypothesis

3.8 Conclusion on Part 1

The template designed for the dimensioning is fully functional regardless the input parameters. As part of the conclusion, some limitations in the dimensioning will be mentioned; this dimensioning was carried out supposing that the lower reservoir would never have any capacity issues, so for instance, the lower reservoir would be infinite like the the sea. Having the sea as a lower reservoir is a possibility, but it is often discarded given the additional costs that installing a desalination plant have. This template could be extended to control also the levels of the lower reservoir by adding more restrictions into the existing model.

As it has been seen, the usage of the diesel engines is quite considerable. This has been a real problem in the real-life installation of this type that currently operates in el Hierro. The location is not windy enough to make the generation 100% renewable, therefore enlarging the pumps or adding more wind turbines makes no difference in the overall functioning.

In the next chapter, the centrifugal pump used in the hybrid plant will be investigated more thoroughly. The performance of a Grundfos impeller will be examined theoretically and empirically to afterwards search for possible design optimizations. The optimized model will try to improve its head since that is what is unquestionably necessary for a hydro storage plant. Any small-scale model to be developed, is applicable to centrifugal pumps of all sizes. Thus, this model will be valid for a 1 MW pump too.

Chapter 4 Pump modelling

4.1. Velocity triangles in the pump's inlet & outlet

The flow in the impeller can be described using velocity triangles which decompose the different magnitudes and directions of the flow. In centrifugal pumps the **absolute velocity** is C , the **blade velocity** is U and W corresponds to the **relative velocity**. The sum of U and W give us C .

The triangles in the inlet and the outlet can be illustrated as the ones in Figure 4-1

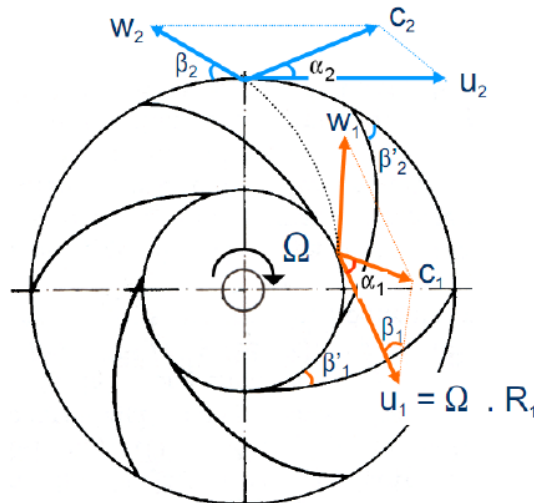


Figure 4-1 Velocity triangles in the inlet and outlet

The angle α is the absolute flow angle of the fluid and β is the blade angle when looking at the tangential direction.

The flow is three-dimensional and therefore the velocities are described in 2 planes; the meridional and the tangential plane. The meridional plane contains the meridional velocity which is the sum of the axial velocity and the radial velocity. Since the inlet to this pump is said to be fully radial, the axial component is inexistent, and therefore the meridional velocity equals the radial velocity.

Inlet

In most cases, it will be assumed that the impeller's inlet is straight and therefore the inlet flow is totally radial, which means that α_1 is 90° as shown in Figure 11-3. This assumption can be made for a radial impeller like the one in Figure 4-2 How to calculate the different velocity components for the inlet of the impeller are further described in Appendix Inlet velocity triangle.

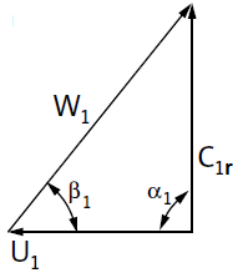


Figure 4-3 Velocity triangle inlet. Source: (Grundfos, 2008)

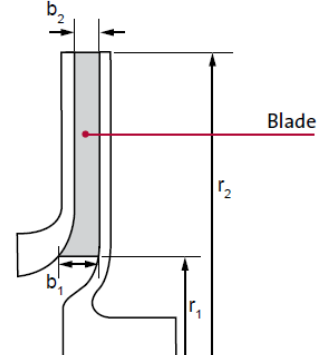


Figure 4-2 Radial impeller. Source: (Grundfos, 2008)

Outlet

In a similar way, as with the inlet, the outlet can be illustrated like in Figure 4-4. How to calculate the different velocity components for the outlet of the impeller are further described in Appendix Outlet velocity triangle

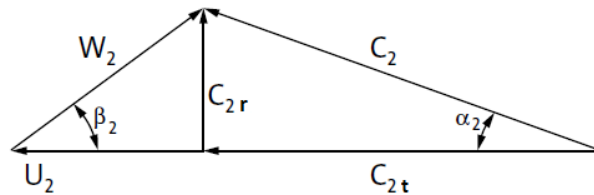


Figure 4-4 Velocity triangle outlet. Source: (Grundfos, 2008)

Euler's pump equation

Euler's pump equation is the most relevant expression in connection to pump design. To determine the balance equations for the pump's impeller we need to fix a control volume. Knowing the control surfaces and the momentum balance we can calculate the energy transfer from the impeller to the fluid. The conservation of momentum doesn't require any knowledge of the flow details inside the control volume, hence it's use. The detailed steps to come up with Eq.(4.1.1) are included in Appendix Euler's pump equation.

$$H_{theoric} = \frac{U_2 \cdot C_{t2} - U_1 \cdot C_{t1}}{g} \quad [m] \quad (4.1.1)$$

Where,

U_2 is the blade velocity at the outlet [m/s] calculated in Eq. (11.3.3)

C_{t2} is the absolute tangential velocity at the outlet [m/s] calculated in Eq.(11.3.5)

U_1 is the blade velocity at the inlet [m/s] calculated in Eq.(11.2.5)

C_{t1} is the absolute tangential velocity at the inlet [m/s] calculated in Eq.(11.2.3)

It must be known about this equation that:

- It is valid for compressible and incompressible flows
- There haven't been needed additional hypotheses to demonstrate it.
- It only depends on the conditions at the entrance and the exit of the pump, not the interior path.
- It is valid regardless the working conditions.

On the other hand, the maximum supplied height Eq.(4.1.2) is given when there's no rotation in the inlet pipe, in other words, when the absolute velocity is perpendicular to the tangential speed of the impeller ($\alpha_1 = 90^\circ$).

$$H_{t\ MAX} = \frac{U_2 \cdot C_{t2}}{g} \quad [m] \quad (4.1.2)$$

Observing the equations (11.4.3)(11.4.4)(11.4.5) it can be demonstrated that a pre-swirl decreases moment, power consumption and head while a counter-swirl has the opposite effect.

4.2 Blade blockage

This concept reflects the fact that blades do have a finite thickness Figure 4-5 that must be considered. Blade blockage has an effect in the outlet of the pump increasing the velocity respect downstream. The reason of this is because the effective area decreases due to the blade thickness. The outlet of the impeller has been taken to exemplify the calculations but the same equations must be used for the inlet too. How to calculate the blade blockage factor τ_2 is explained in detail in Appendix Blade blockage

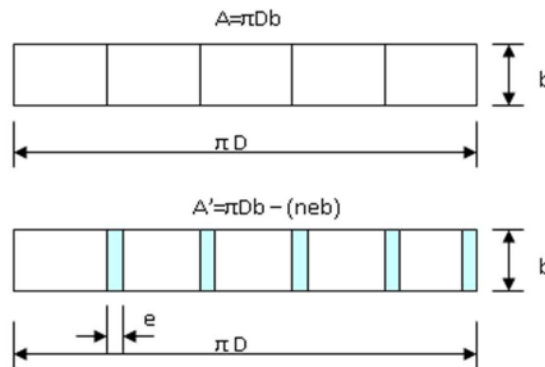


Figure 4-5 Reduction of the effective area

It is important to remark that blade blockage only exerts an effect on the radial component of the absolute velocity both at inlet and outlet C_{1r} and C_{2r} . On the other hand, the slip has an effect on the tangential component as it will be seen now.

4.3 Slip factor

The slip factor refers to the flow deflection caused by the blades. The real flow doesn't follow the blades as Euler's equation considers (Figure 4-6), the flow's angle and the blade angle aren't the same therefore. When the moment of momentum is calculated the real flow conditions occurring inside the impeller are ignored and consequently the conservation of momentum doesn't manage to reflect how the flow was generated.

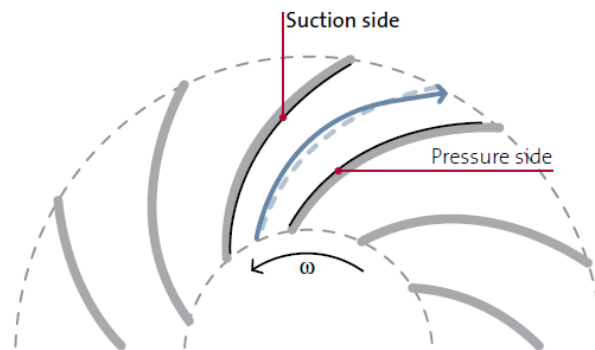


Figure 4-6 Difference between ideal flow (dashed) and real flow (continuous).Source: (Grundfos, 2008)

The velocity triangle at the impeller's outlet is corrected by taking into account the slip factor (as mentioned above). Consequently, it will affect all the calculations in which the velocity triangle at the impeller's outlet is involved. However, the slip itself is not considered an explicit pump loss, it only affects the head.

There are various methods for calculating the slip, only the Gülich slip factor will be used in this report. Detailed calculations on how to calculate the slip factor γ are included in Appendix Slip

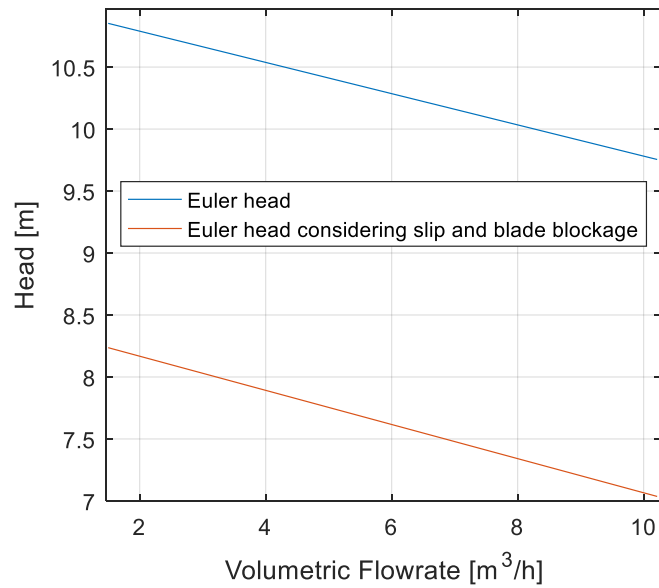
The slip affects the absolute tangential velocity at the outlet C_{2t} which will have a direct effect on Euler's head. The real head that is going to be delivered by the pump will obey the following equation from which the losses are going to be described in the next section.

$$H_{real} = \frac{U_2 \cdot C_{2tcorrected} - U_1 \cdot C_{t1}}{g} - \sum H_{losses} \quad [m] \quad (4.3.1)$$

Where,

$C_{2tcorrected}$ is calculated in Eq.(11.6.2)

As a conclusion, Graph 4-1 exemplifies what the above sections have talked about. Slip and blade blockage have a considerable effect on the head but are not considered head losses.

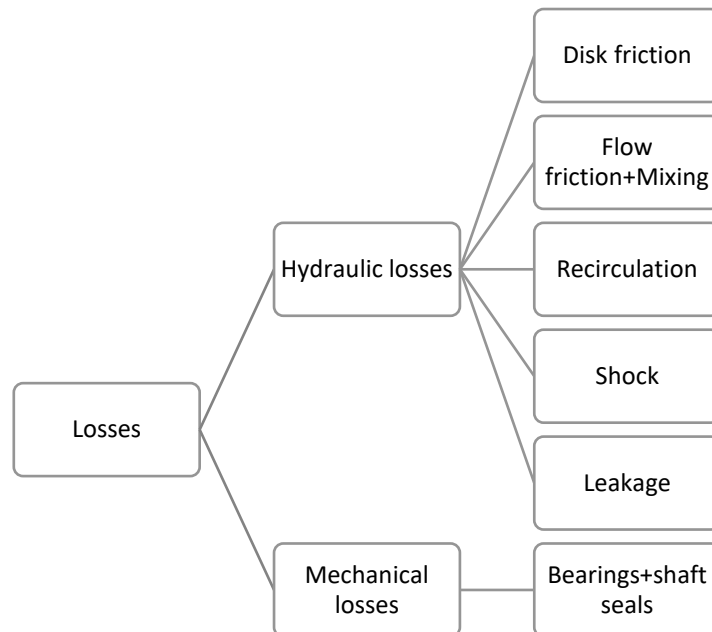


Graph 4-1 Head reduction due to slip and blade blockage

4.4 Pump losses

As it has been mentioned previously, all the head calculations seen up to here are ideal. If we now consider the hydraulic and mechanical losses that occur in reality a lower performance will be obtained than the estimated in first place.

The losses result in a smaller head and a higher power consumption depending on where they occur. See Table 4-1



Scheme 4.4-1 Schematic on different loss types

| Loss | Lower Q | Lower H | Lower P |
|------------------------|---------|---------|---------|
| Flow friction | | X | |
| Mixing | | X | |
| Recirculation | | X | |
| Shock | | X | |
| Leakage | X | | |
| Disk friction | | | X |
| Bearings & shaft seals | | | X |

Table 4-1 Types of losses in pumps. Source: (Grundfos, 2008)

4.4.1 Mechanical losses

This type of losses occur due to the friction generated between the rotating impeller and the pump housing. They are generated by the radial bearings, the axial bearings and the shaft seal. These losses vary with the design, the rotational speed and the pressure. The mechanical efficiency in most large pumps is around a 99,5%, unlike small pumps that tend to have lower efficiencies.



Figure 4-7 Source: (Grundfos, 2008)

4.4.2 Hydraulic losses

Hydraulic → Due to the friction produced by the friction between the fluid and the interior of the pump. A brief description of each type is listed below.

Flow friction losses

It occurs in areas where the fluid is in contact with the impeller, and the inside surface area of the housing of the pump. This friction causes a pressure loss which reduces the head of the pump. It depends on the roughness of the surface and the relative velocity to the surface. The equations will be calculated in Appendix Friction losses

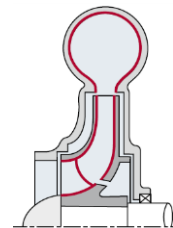


Figure 4-8 Source: (Grundfos, 2008)

Shock losses

These losses occur since the blade has an actual thickness, it is not infinitely thin. Therefore the fluid collides with the blade producing a fluid deceleration from the inlet of the blade to the blade's throat. The equations for this loss appear in Appendix Shock losses



Figure 4-9 Source: (Grundfos, 2008)

Mixing losses at cross-section expansion/contraction

When entering a sudden expansion velocity differences occur and the kinetic energy is transformed into static pressure energy, the water particles don't move any more at the same speed and friction occurs resulting in a head decrease. These expansions occur typically at the volute, the diffuser and the return channel. That's why it is important to create smooth edges in the expansions. Detailed equations are included in Appendix Expansion and contraction losses

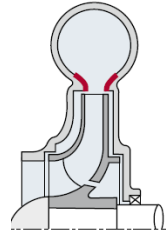


Figure 4-10 Source: (Grundfos, 2008)

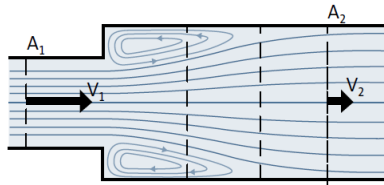


Figure 4-11 Sudden expansion. Source: (Grundfos, 2008)

Contractions accelerate the flow which must decelerate consequently after the contraction, this introduces mixing losses typically at the inlet of the blade channels or the impeller's eye. As with the cross-section expansion, this loss can be reduced by smoothing and rounding the edges. Detailed equations are included in Appendix Expansion and contraction losses

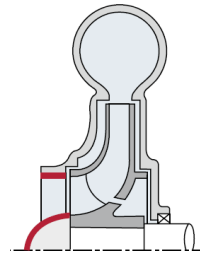


Figure 4-12 Source: (Grundfos, 2008)

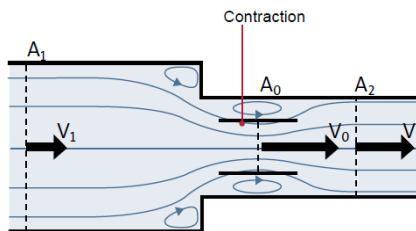


Figure 4-13 Sudden contraction. Source: (Grundfos, 2008)

Recirculation losses

This often occurs when the flow circulating through the impeller is not the optimum design flow for example when the flow is near $Q = 0$. In this circumstances, we have the highest recirculation losses as we can see highlighted in blue in Figure 4-15. Detailed equations can be found in Appendix Recirculation losses

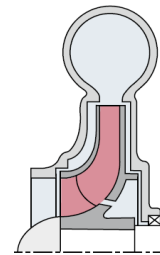


Figure 4-14 Source: (Grundfos, 2008)

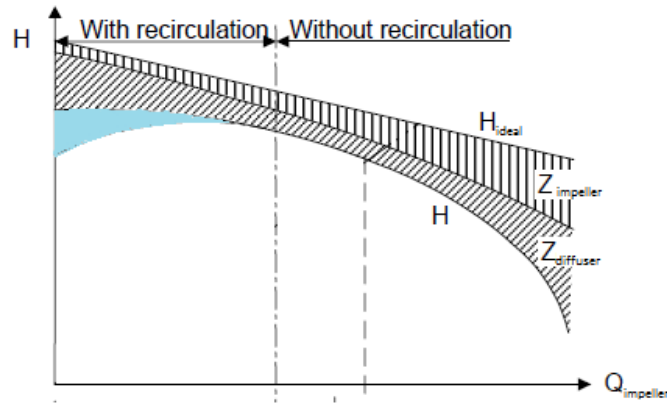


Figure 4-15 Head loss due to recirculation. Source: (Gülich, 2010)

Disk friction losses

These losses are due to the rotation of the impeller and the fluid. As the Table 4-1 mentions this loss increases the power consumption of the pump. The steps on how to calculate it are included in Appendix Disk friction losses

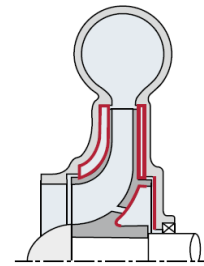


Figure 4-16 Source: (Grundfos, 2008)

Leakage flow

Leakage occurs when there's a back flow through the existing gaps between the impeller and the housing. This results in losses due to the flow in the impeller being greater than the one through the pump. Further explanation and calculations are included in Appendix Leakage flow.

$$Q_{impeller} = Q_{pump} + Q_{leakage} \quad [m^3/s] \quad (4.4.1)$$

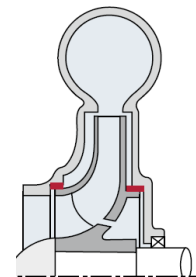
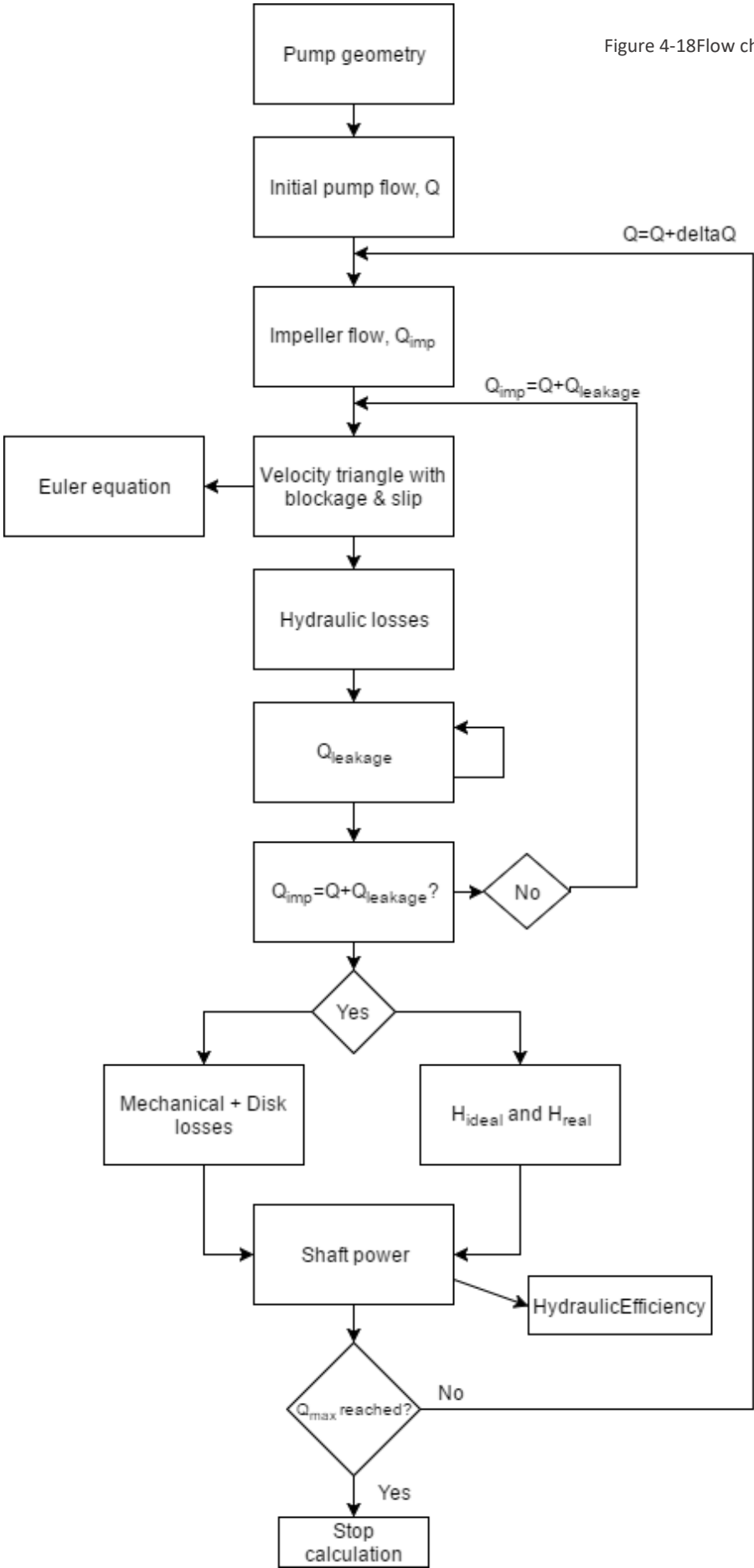


Figure 4-17 Source: (Grundfos, 2008)

4.4.3 Procedure to incorporate losses

These calculations have to follow a specific order since there are a lot of existent dependencies between results. Some losses can't be calculated without previously having done some other steps. For instance, the leakage flow depends on the pressure loss across the impeller and simultaneously the pressure loss depends on the flow rate through the impeller. Consequently, an iterative process is needed. After each iteration, the value of $Q_{impeller}$ is updated to $Q_{impeller} = Q_{pump} + Q_{leakage}$. This is better illustrated in Figure 4-18.

Figure 4-18 Flow chart for MATLAB model



4.5 Pump power and efficiency

The mechanical power that is delivered to the shaft, recognized as P_2 in Figure 4-19 is a sum of the power delivered to the fluid P_{fluid} and the power losses during the process.

$$P_2 = P_m + P_{disk} + P_{hydr} + P_{fluid} \quad [W] \quad (4.5.1)$$

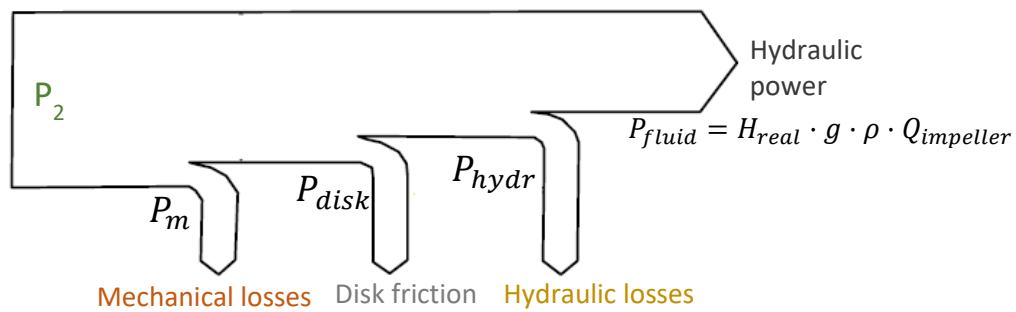


Figure 4-19 sankey diagram with power flow through the impeller

On the other hand, we can describe the pump's hydraulic efficiency using the power that has actually been absorbed by the fluid and the power that was originally provided

$$\eta_{hyd} = \frac{P_{fluid}}{P_2} \cdot 100 \quad [\%] \quad (4.5.2)$$

Chapter 5 Model validation

This chapter will take a closer look at the test results obtained in the lab set-up with the Grundfos impeller NK-32-125/142, to compare them to the model results obtained with MATLAB. This comparison will serve to verify the results from the model and introduce the necessary manipulations to the model in order to fit it to the curves obtained in the lab. The pump curves from the manufacturer data sheets will also be plotted to gain an idea where the data sheet is compared to the model prediction and the test points. The data-sheet points have been plotted using a third-degree polynomial spline. Despite including them, they are not going to be considered in the fitting since it is unknown how their curves might have been manipulated for sales-aesthetic reasons to make them more attractive to their clients. Therefore, the comparison will only be done with measures and values that have been taken for the purpose of the project.

The test results were obtained from a test-setup. The desired measurements were acquired and treated with a LabView code. The details of the set-up and the measuring procedure are not part of this report.

The chosen rotational velocities to carry out the measurements were 1400 rpm and 1100 rpm.

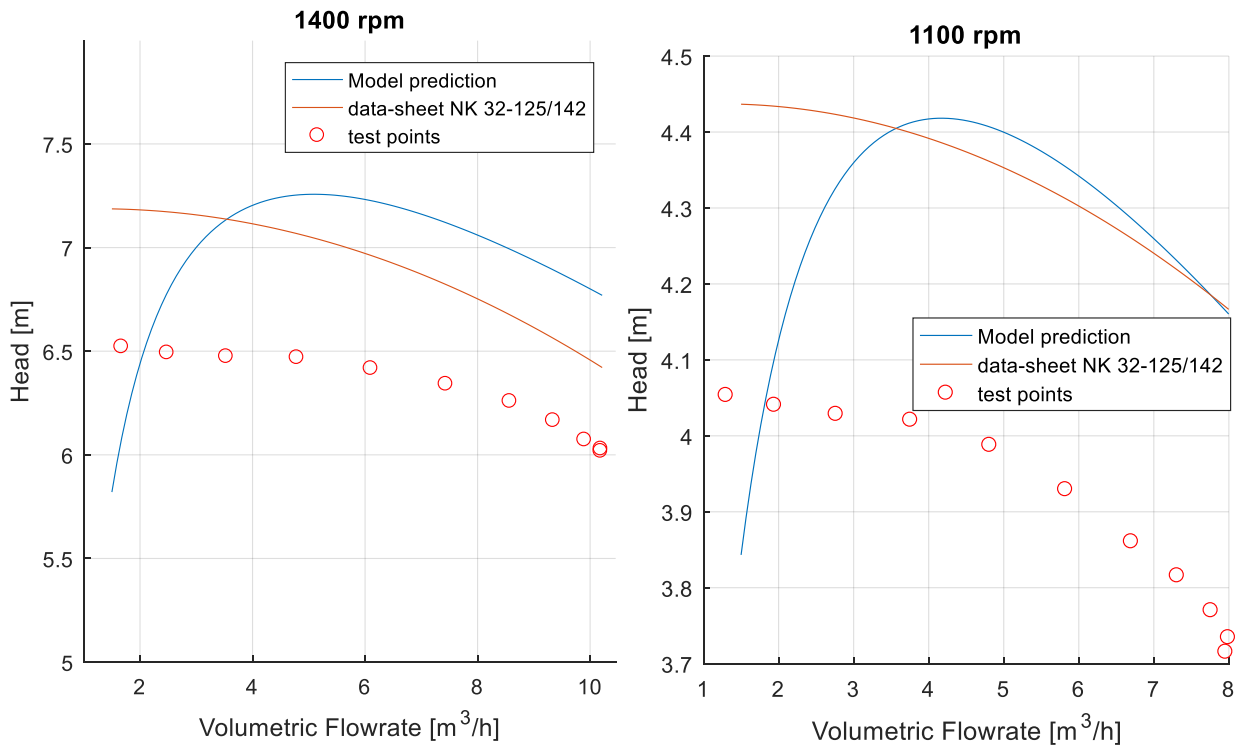
5.1 Fitting of the model

The most relevant figures such as head, efficiency and power as a function of the Flow will be compared and fitted to the test results. The flow range will be comprised from a minimum of 1.5 m³/h to the maximum flow rate that the test rig measured during the testing. In order to carry out the fitting, some of the equations might have to be manipulated. The manipulations that will be carried out will also be mentioned in this sub section

Pump head curve

As it may be observed from Graph 5-1 in both rotational speed conditions the head of the model is above the test points and above the data-sheet curve at all flow rates excepting the low ones. With 1400 rpm, the head difference is of 0.7 m at the highest flow rate and of 0.5 m for 1100 rpm. The data-sheet curve seems to be at an intermediate point between the model and the test-points and has a more accurate shape than the model. Despite this, it is still above the test-points. The data-sheet curve has a more 'ideal' pump curve which complies with the 'CFC'¹ curve. Meanwhile, the test points show a more constant head at low flow rates. It is question-less that the head has to be fitted.

¹ CFC states for constantly falling curve



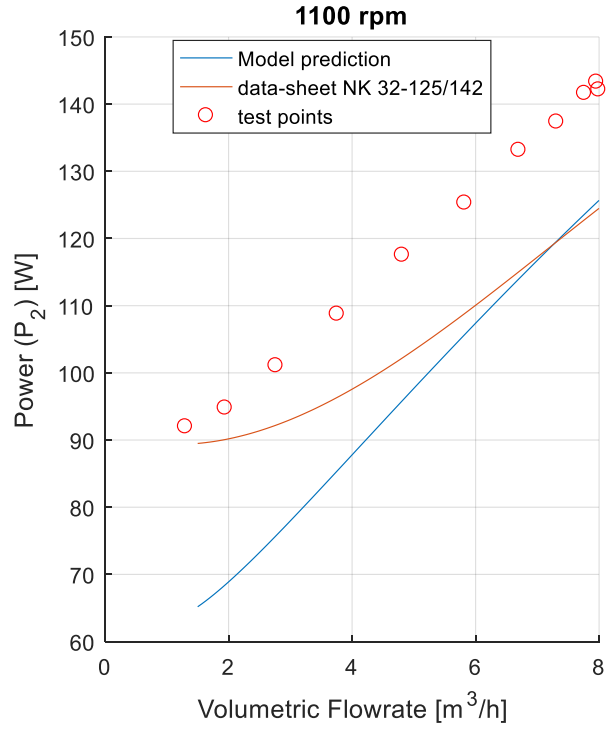
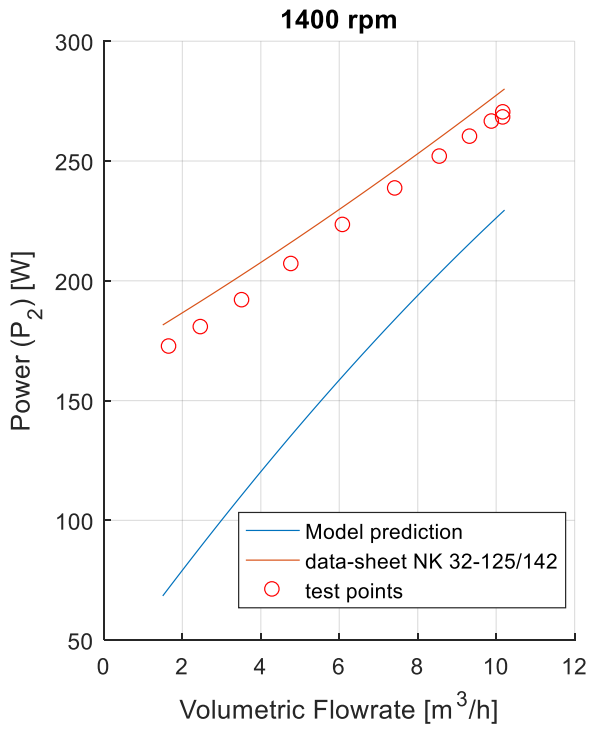
Graph 5-1 comparison of Q-H curves for model , test points and data-sheet at 1400 and 1100 rpm

P₂ and P_{hyd} curves

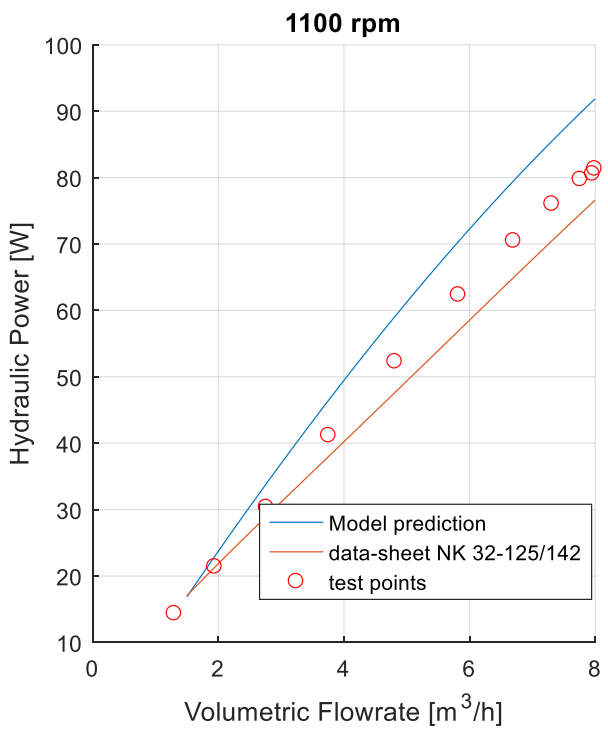
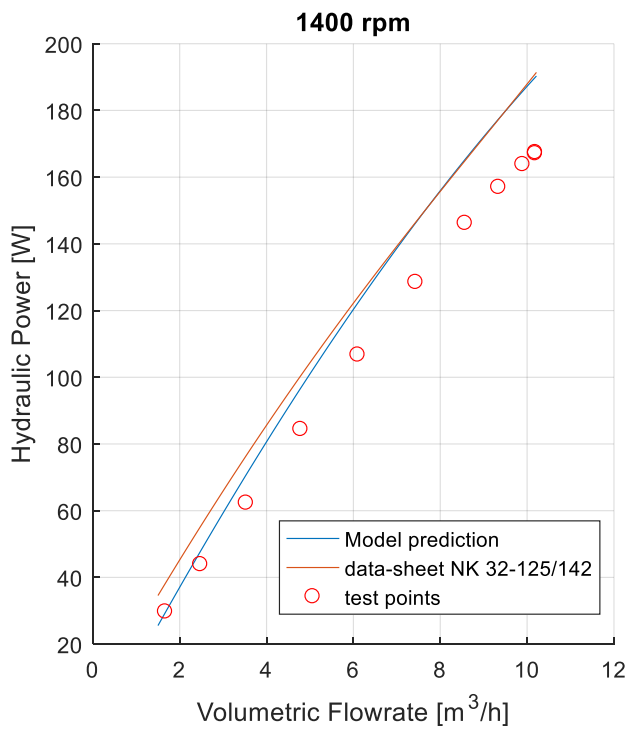
As it can be seen from Graph 5-2 in both cases the modeled power is below the test points. At 1400 rpm the difference between the model and the test points is the largest at low flow rates, having its maximum difference at 100 W at 1.5 m³/h. At 1100 rpm, the difference is also obvious, reaching a maximum of 27 W at 1.5 m³/h. The opposite happens at 1400 rpm with the data-sheet curve which shows an almost perfect concordance with the test points. This behavior doesn't repeat at 1100 rpm, where the data-sheet curve starts near the test-points but diverges towards the modeled curve at high flow rates.

On the other hand, Graph 5-3 which plots the hydraulic power, shows much more similarity between the model and the test points. There is also reasonable similarity between the model curve and the data-sheet curve. In this case both rpm's show major deviations between the three curves towards larger flow rates. At 1400 rpm the biggest difference is of 20 W and at 1100 rpm the biggest difference is of 12 W between the test-points and the model, in both cases at the highest flow.

As with the head, the P₂ curve must be fitted too



Graph 5-2 Q-P₂ curve comparison for 1400 rpm and 1100 rpm



Graph 5-3 Q-P_{hyd} curves at 1400 rpm and 1100 rpm

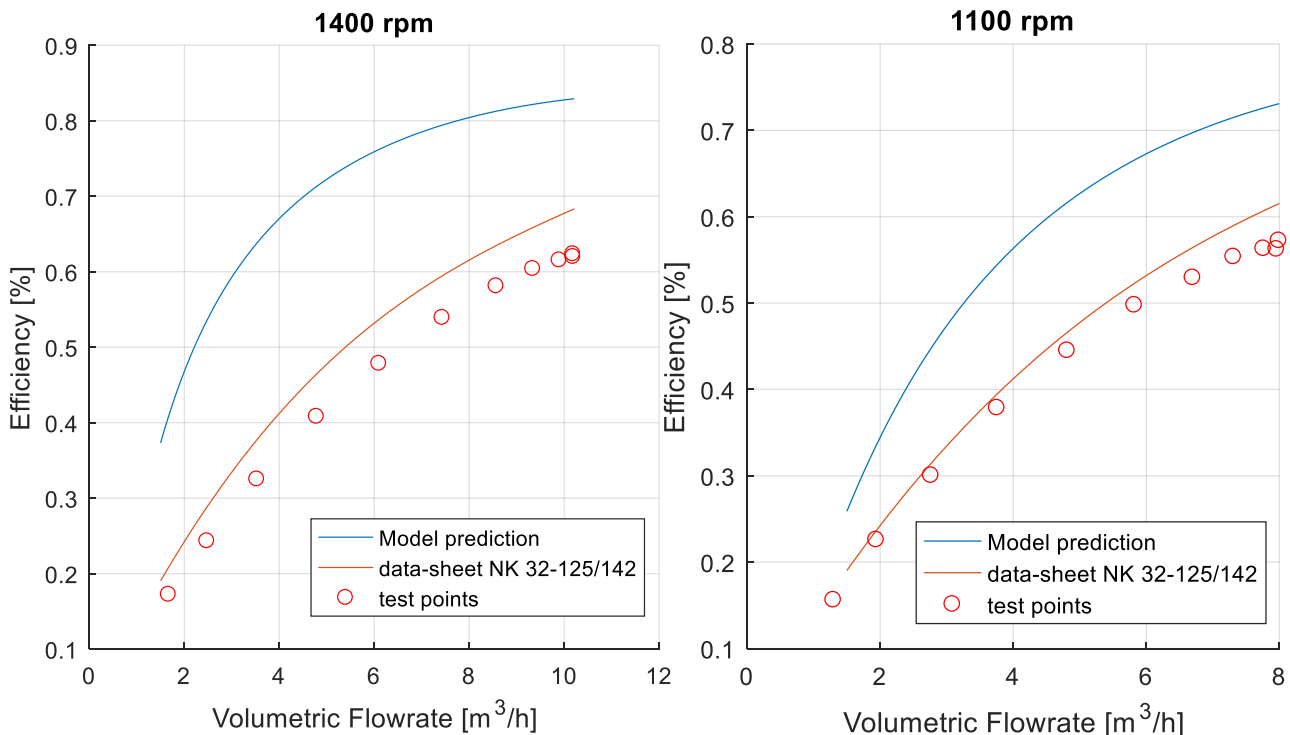
Hydraulic efficiency curve

As it occurs with the head, the modeled efficiency is also higher than the real one Graph 5-4. Since the efficiency is calculated with the absorbed power by the fluid P_{fluid} and the mechanical power delivered to the impeller P_2 , one of these 2 values must be very deviated from the test points, and therefore the efficiency curves vary so much.

$$\eta_{hyd} = \frac{P_{fluid}}{P_2} \cdot 100 \quad [\%] \quad (5.1.1)$$

At 1400 rpm the difference is much obvious. By observing Graph 5-2, it can be seen where the reason of the difference lies. Being the difference so obvious in Graph 5-2 for the P_2 , it is logical that the efficiency will also be very deviated. Therefore, the conclusion is that some fittings have to be carried out, especially when it comes to the head and the P_2 .

In this case the similarity between the data-sheet curve and the test-points is surprising compared to the other pump characteristics



Graph 5-4 Q- η comparison at 1400 rpm and 110 rpm

Fitting of the model

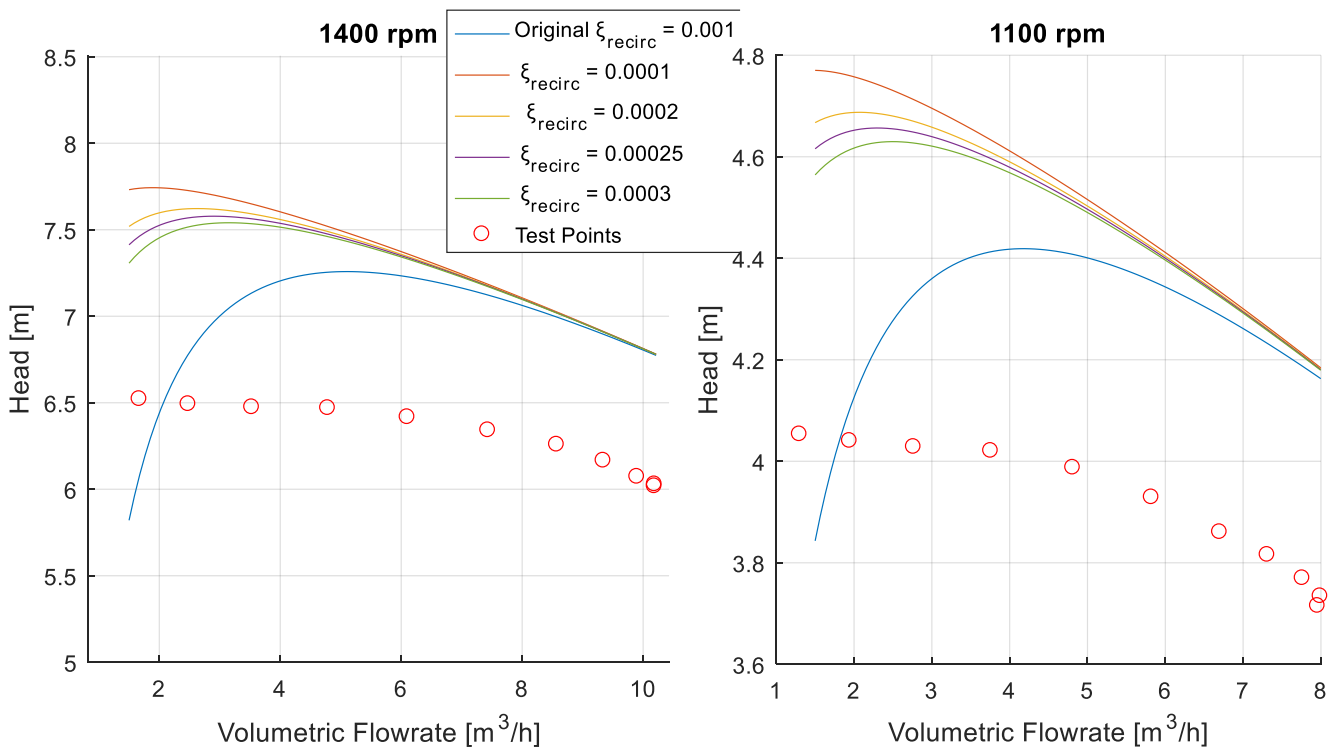
Head

It is undeniable that the head needs to be lower but that there's a major problem with it at low flow rates. When it comes to the pump head, the first thing that should be thought about are head losses. These are the ones that have a major repercussion in the final real head. All the head losses were described in Table 4-1. The two losses which have a greater effect in the head are recirculation losses and friction losses, which will be examined in this respective order.

The curvature present at low flow rates is due to the recirculation loss which has a great effect in the head. (Tuzson, 2000) uses Eq. (5.1.2) to calculate the power loss due to recirculation. This power calculation uses a recirculation loss coefficient that can take values ranging from [0.001-0.007]. Varying the value of $\xi_{recir.}$ has important repercussions.

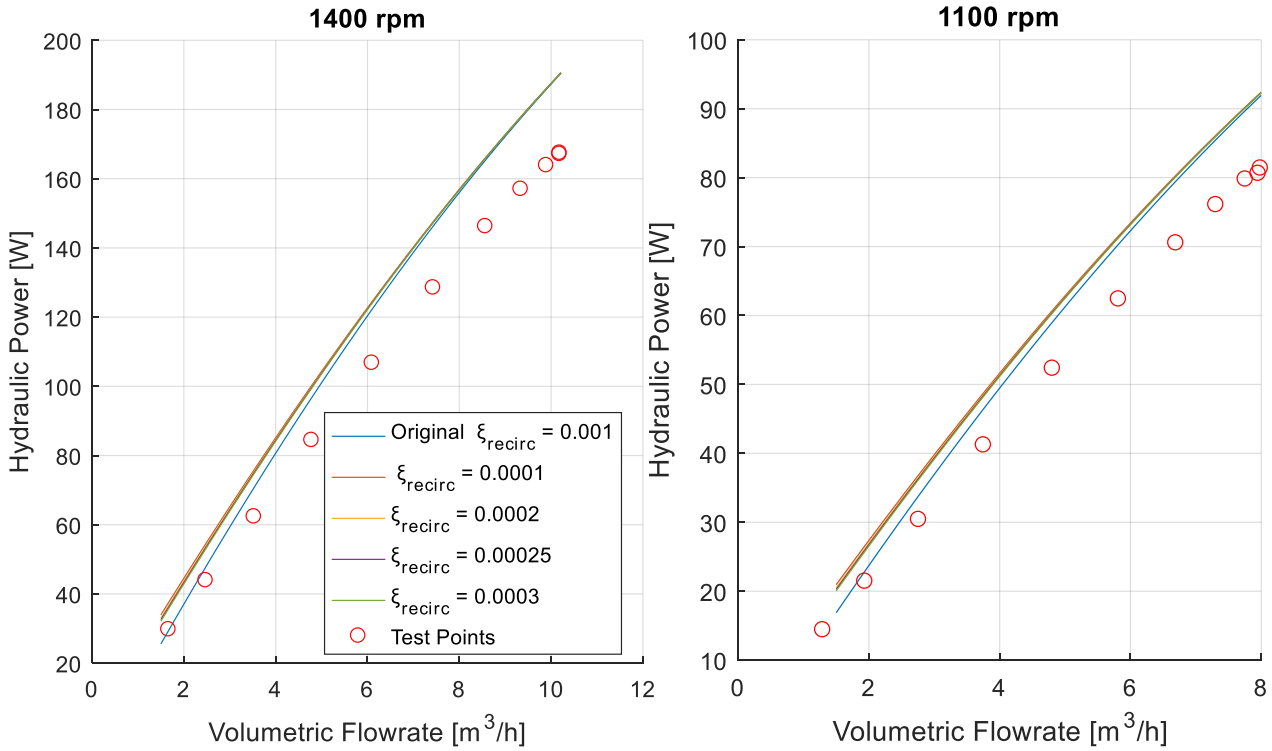
$$P_{recir.} = \xi_{recir.} \cdot \omega^3 \cdot d_1^2 \cdot \left(1 - \frac{Q_{impeller}}{Q_{BEP}}\right)^{2.5} \quad [W] \quad (5.1.2)$$

As it can be seen in from Graph 5-5 and Graph 5-6, the recirculation coefficient had to be decreased by 10 times in order to obtain a curve with a more similar curve to the test points. This is common in both rotational velocities which present the same problem. From Graph 5-6 it could be said that the curve fitted the test points better with the original value, but since the change in very valuable in the head, there is no doubt that the coefficient has to be decreased. To comply with the 'CFC'² principle, the smallest value for the recirculation coefficient was chosen $\xi_{recir.} = 0.0001$. This coefficient will be applied to proceed with the fitting.



Graph 5-5 Q-H comparing the effect of $\xi_{recir.}$ at 1400 and 1100 rpm

² 'CFC' stands for constantly falling curve



Graph 5-6 Q-Ph_{vd} comparing the effect of ξ_{recirc} . at 1400 and 1100 rpm

Furthermore, friction losses not only occur in the impeller, but they occur in the volute too. These last ones were not taken into account despite being described in Appendix B.1 Friction losses in the volute.

This loss was described with the same principle as the rest of hydraulic losses:

$$H_{fric\,volute} = \xi_{volute} \cdot \frac{(\sqrt{C_{2r}^2 + C_{2t}^2})^2}{2g} \quad [m] \quad (5.1.3)$$

Where,

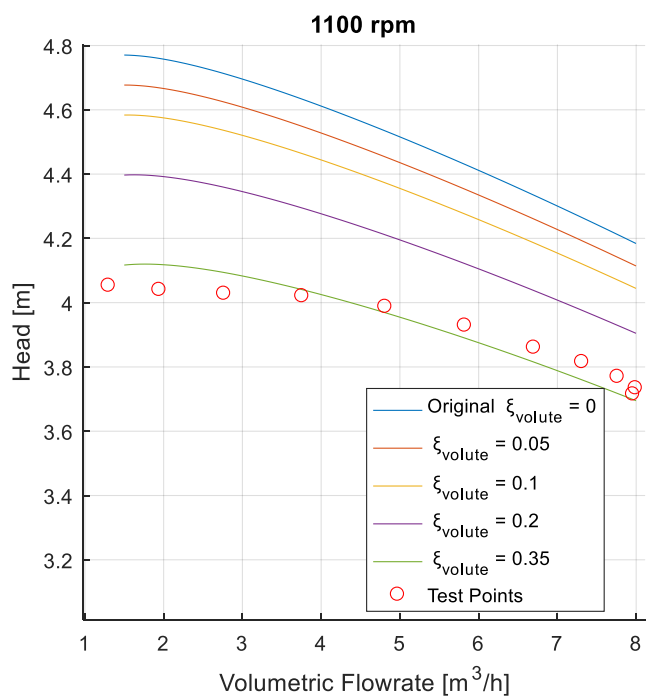
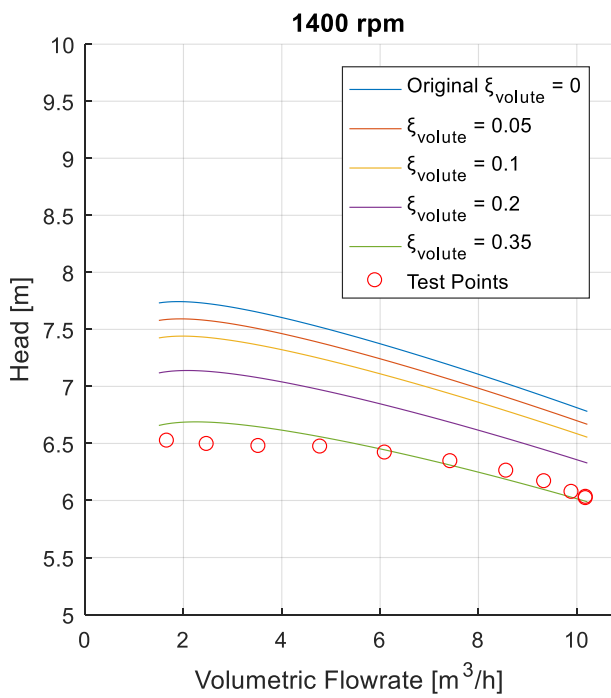
ξ_{volute} coefficient for these losses in the volute [-]

C_{2r}/C_{2t} are the flow's outlet radial and tangential speeds [m/s]

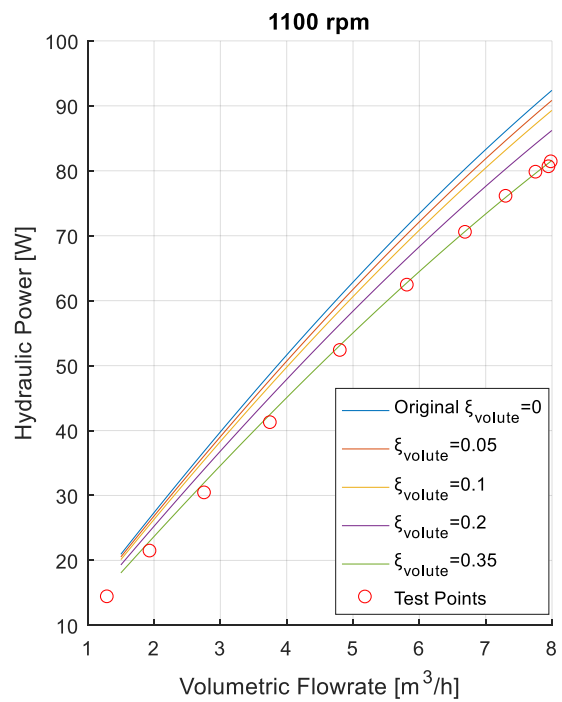
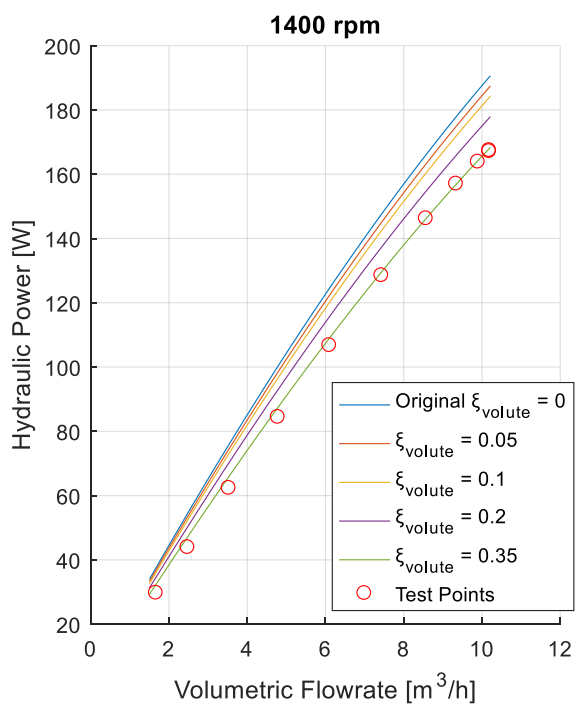
g is the gravity acceleration [m/s²]

The friction coefficient ξ_{volute} will have a great effect on the overall head loss, so it is the major source of uncertainty in this equation.

As it can be seen in Graph 5-7 in both cases the biggest ξ_{volute} is the one that fits the test curve the best. Additionally, to confirm that this value is suitable, the hydraulic power has also been plotted in Graph 5-8. This plot also shows that at both rotational speeds, 0.35 continues to be the most accurate choice. Therefore, ξ_{volute} takes a value from this point on of 0.35.



Graph 5-7 Effect of ξ_{volute} in the head for 1400 rpm and 1100 rpm

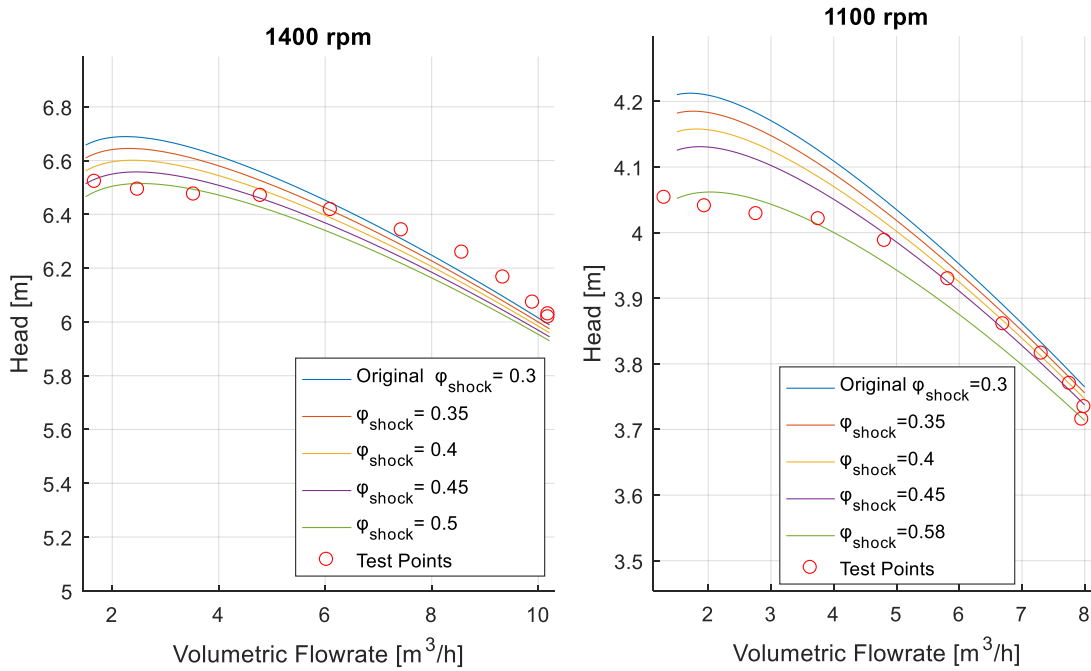


Graph 5-8 Q-Phyd for varying ξ_{volute} at 1400 and 1100 rpm

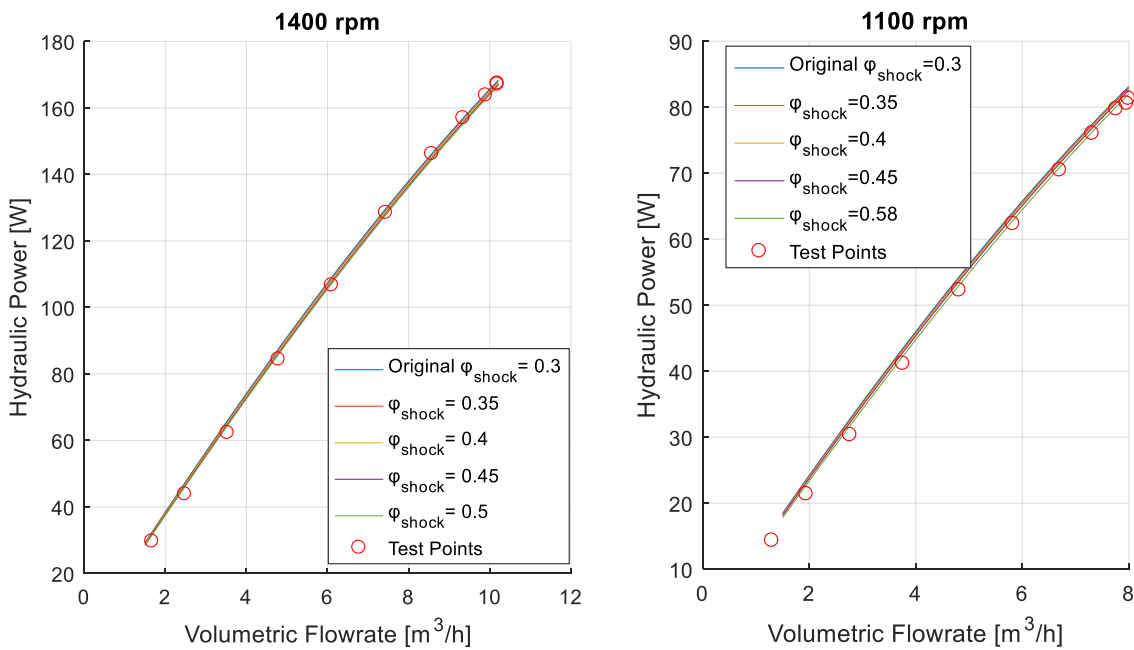
From Graph 5-7 it can be observed that the head at low flow rates still doesn't fit the test curve. Literature shows the major head losses at low flow rates are also due to shock losses. Therefore, the shock loss coefficient will be further examined.

$$\xi_{shock} = \varphi_{shock} \left(\frac{W_{1r} - W_{1throat}}{U_2} \right)^2 \quad [-] \quad (5.1.4)$$

The relative shock factor φ_{shock} (which initially takes a value of 0.3) can be varied to fit the test points.



Graph 5-9 Q-H for varying φ_{shock} at 1400 and 1100 rpm



Graph 5-10 Q- P_{hyd} for varying φ_{shock} at 1400 and 1100 rpm

As it can be seen from Graph 5-9, the difference of head at low flow between the model and the test points can be diminished at the expense of lowering the head too at high flow rates. Given the fact that Graph 5-10 shows that varying φ_{shock} doesn't improve the fitting of the hydraulic power curves, the φ_{shock} will remain unchanged from its original value of 0.3.

P_2

Moreover, the P_2 also has to be fitted given the deviations seen before in Graph 5-2. Once again, the power losses must be looked into.

P_2 can be described as:

$$P_2 = P_{mech} + P_{disk} + P_{hydr,loss} + P_{fluid} \quad [W] \quad (5.1.5)$$

From where, the most relevant contributors are P_{mech} and P_{disk} . On the other hand, P_{disk} depends basically on geometrical parameters which cannot be manipulated. Instead, P_{mech} does count with constant values within its definition which could have an end effect on P_2 .

$$P_{mech} = \varphi_{mech} \cdot \left(\frac{Q_{ref}}{Q}\right)^{0.4} \cdot \left(\frac{n_{ref}}{n}\right)^{0.3} \cdot P_{opt} \quad [m/s] \quad (5.1.6)$$

Where,

Q_{ref} is the reference volumetric flow which equals 1 m³/s

φ_{mech} is the mechanical coefficient. According to (Gulich, 2010) this value is 0.0045

Q is the volumetric flow through the impeller [m³/s]

n_{ref} is the reference rotational speed which equals 1500 rpm

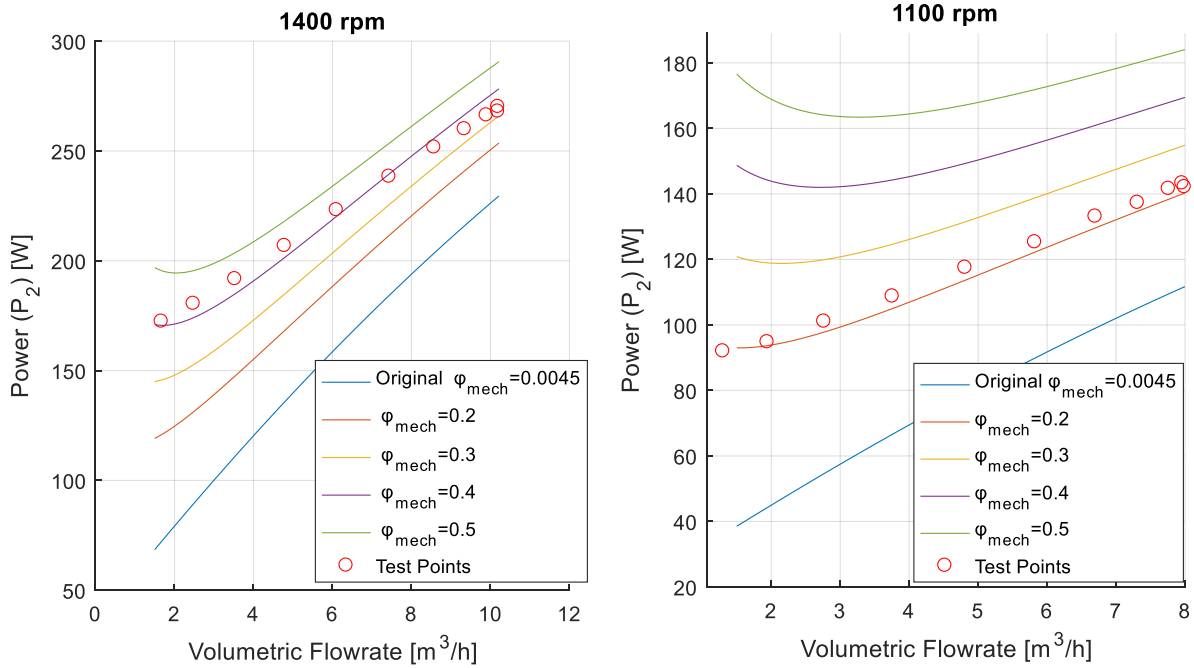
n is the impeller's rotational speed [rpm]

P_{opt} is the shaft's power at the BEP [W]

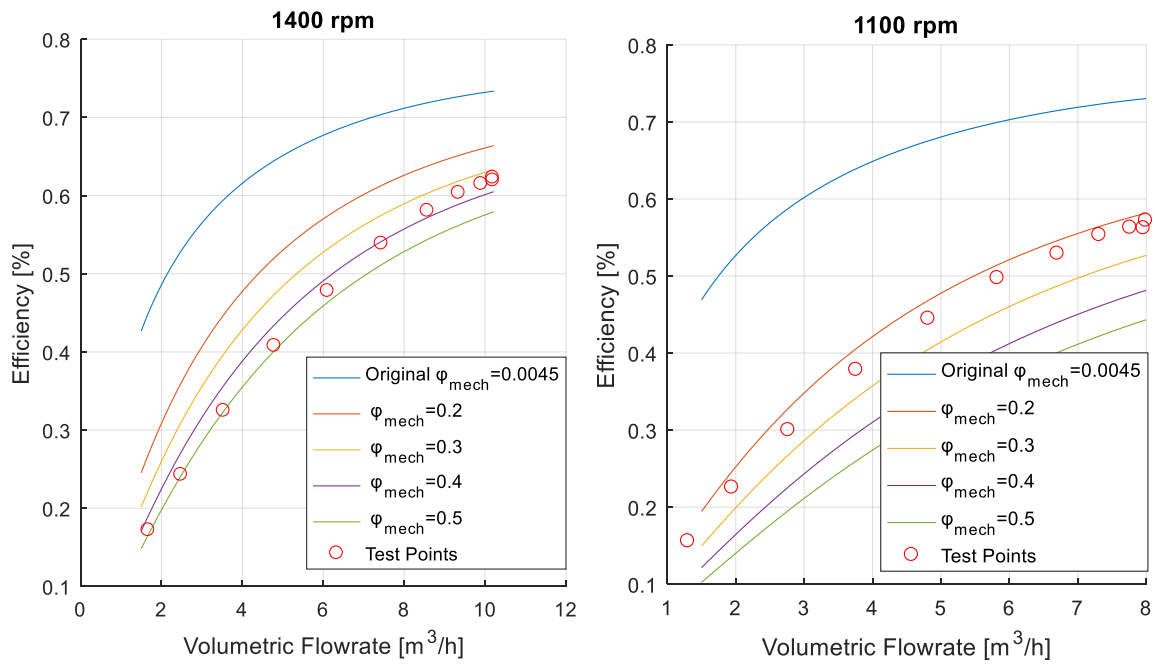
φ_{mech} must take on higher values to increase the mechanical losses.

Graph 5-11 and Graph 5-12 reflect two things; the value of φ_{mech} must indeed be higher and the optimum value for φ_{mech} differs from one rotational speed to the other. This occurs because P_{mech} is also dependent on n [rpm], hence there will never be a common φ_{mech} at which both fit the test points accurately.

Consequently, a medium point between [0.2-0.4] both should be chosen and that point is 0.3.



Graph 5-11 Q-P2 for varying ϕ_{mech} at 1400 and 1100 rpm



Graph 5-12 Q- η for varying ϕ_{mech} at 1400 and 1100 rpm

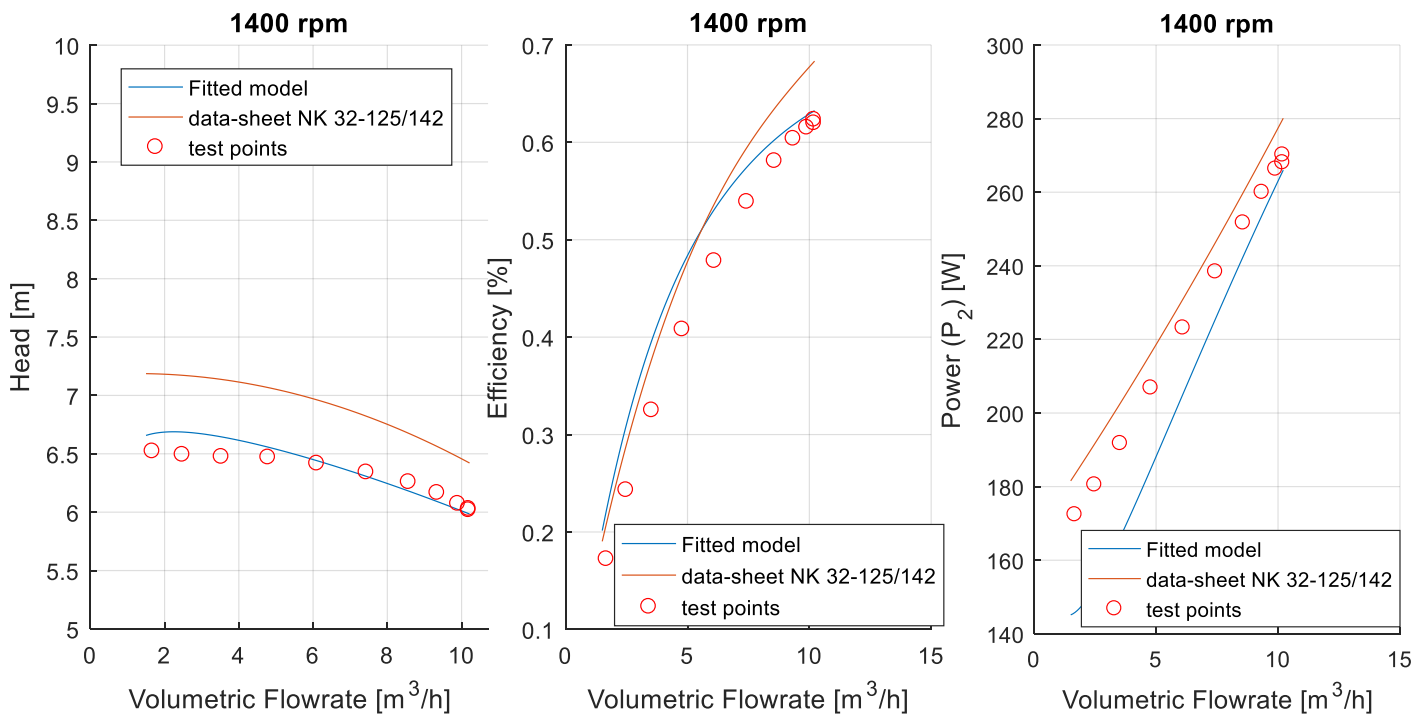
Final fitted model

| Name of the coefficient | Symb | Initial value | Fitted value | Unit | Affects... |
|--------------------------------|-------------------|---------------|--------------|------|-----------------------------|
| Recirculation coefficient | $\xi_{recir.}$ | 0.001 | 0.0001 | [-] | Recirculation losses → head |
| Friction coefficient volute | ξ_{volute} | 0 | 0.35 | [-] | Friction losses → head |
| Relative shock factor | φ_{shock} | 0.3 | 0.3 | [-] | Shock losses → head |
| Mechanical loss factor | φ_{mech} | 0.0045 | 0.3 | [-] | Mech. losses → power |

Table 5-1 Summary of fitting modifications

5.2 Fitted model and experimental results

Head, efficiency and power characteristics

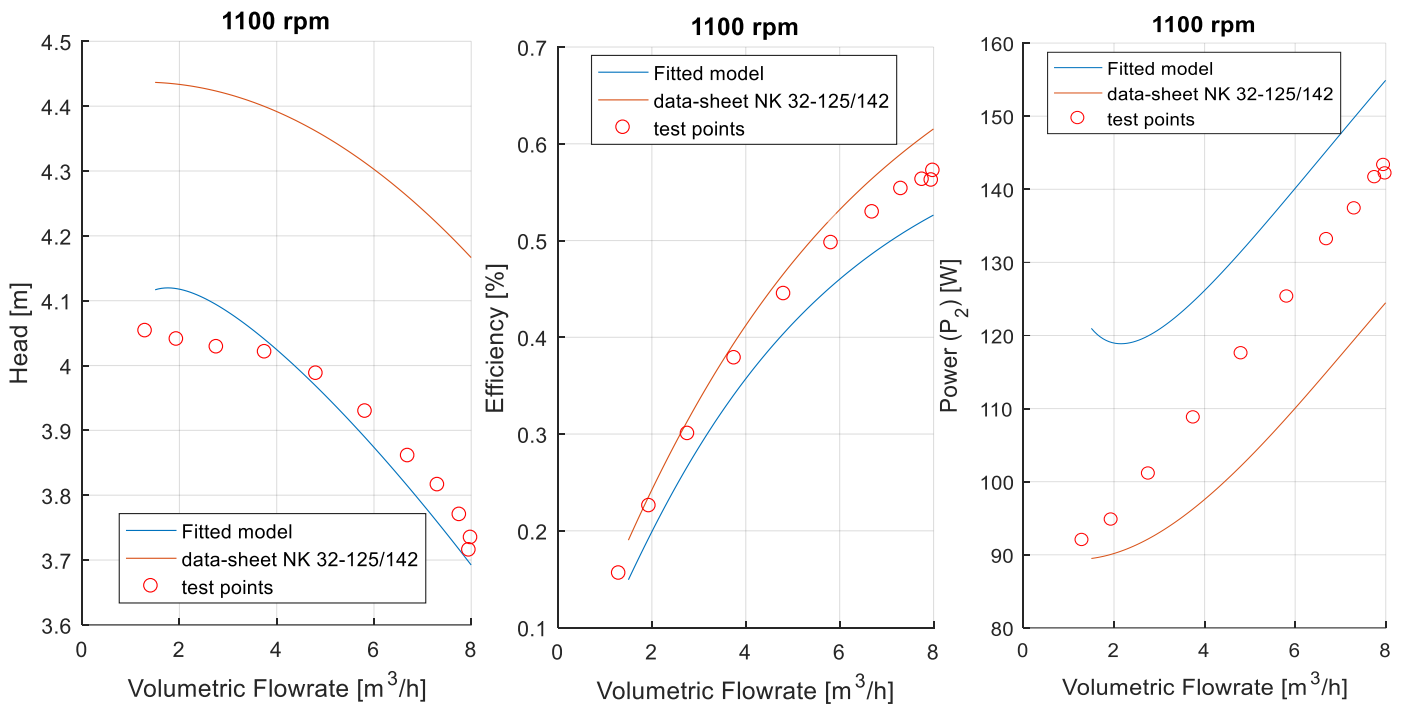


Graph 5-13 Q-H, Q- η and Q-P₂ at 1400 rpm fitted

In all cases, the fitted model is able to model the experimental results more accurately than the unfitted one (see Graph 5-14 and Graph 5-13) Despite still having some issues with the head at low flow rates which remained unsolved, the rest of the head curve follows the same line tendency as the test points at both rotational speeds. After the fitting, the model is more accurate than the data-sheet points, achieving a better concordance in all plots except for the power curve.

With the power curve, the fitting was done up to a certain extent since a balance between the two rotational speeds had to be found. Therefore, in the case of 1400 rpm (Graph 5-13), the fitted plot of P₂ remains below the test points and at 1100 rpm (Graph 5-14) it remains above.

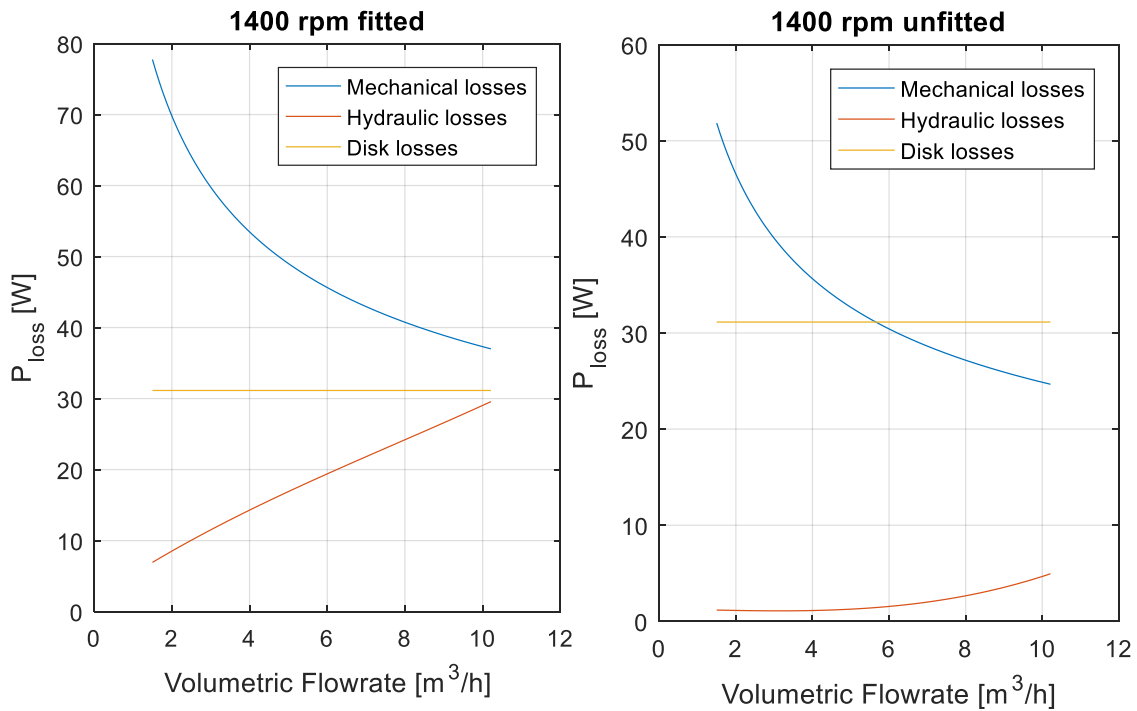
This has consequences on the efficiency plot, which shows the same respective behavior at both speeds. From the plots though, it could be said that overall, the fitting has had a better result at 1400 rpm than at 1100 rpm.



Graph 5-14 Q-H, Q- η and Q-P₂ at 1100 rpm fitted

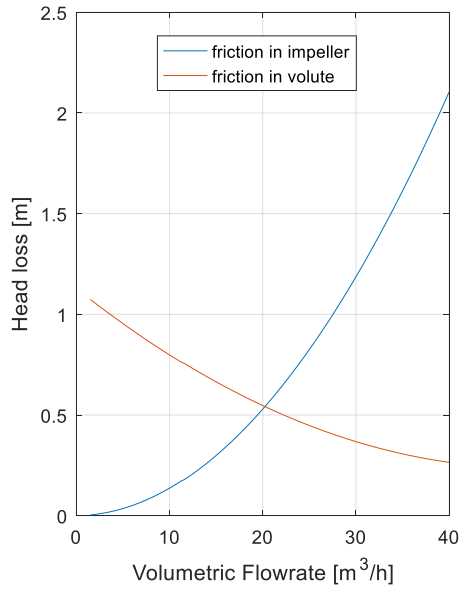
Head loss and power loss characteristics

In Graph 5-15 the different contributions to power losses can be seen. Mechanical losses plot a logarithmic shaped curve which is inversely proportional to flow rate, getting lower when the flow increases, whilst hydraulic losses grow towards higher flow rates. Disk losses don't have any dependence with the flow, hence they have a constant value throughout the model. If the fitted and the unfitted plot are compared, 2 clear observations can be made; firstly, the only change that the mechanical losses have perceived is an upward scaling while keeping the same logarithmic shape. Secondly the hydraulic losses grow in both cases towards higher flow rates but in the fitted model they do so starting from an offset value of around 8 W, while in the unfitted plot the offset value is merely of 2 W. That is due to the friction losses in the volute.

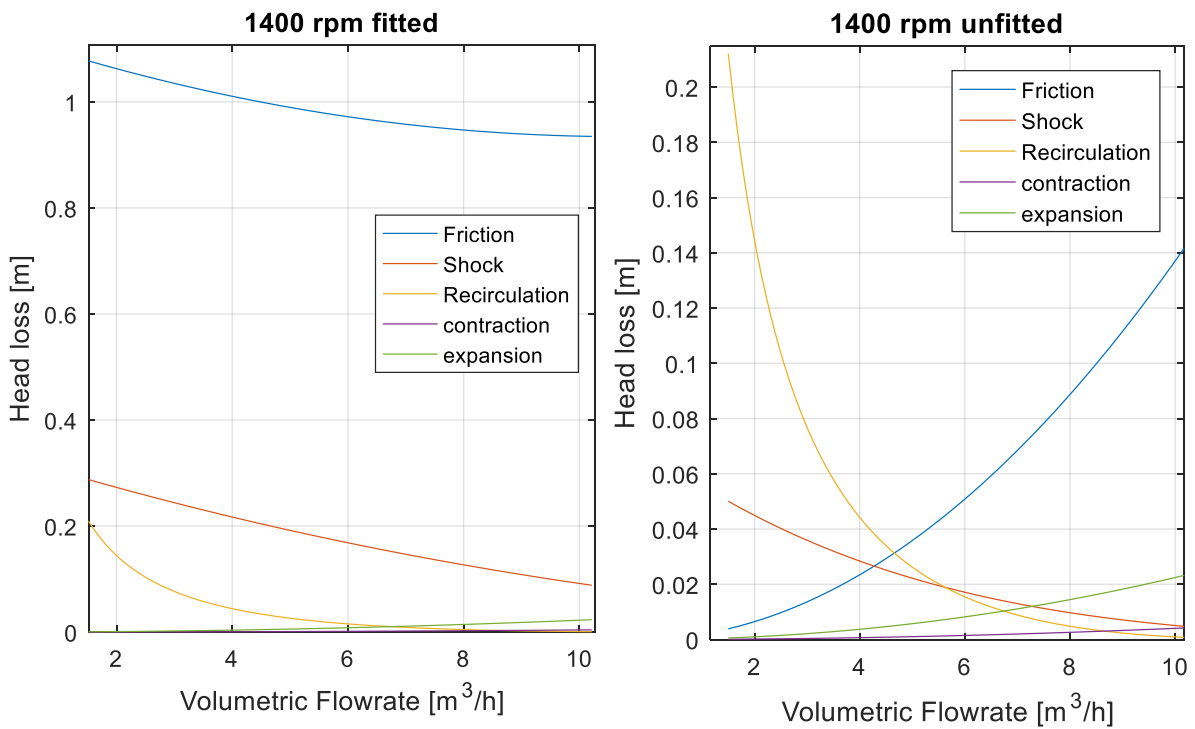


Graph 5-15 Q-P_{loss} comparison between different contributions

When the hydraulic head losses are looked into with more detail (see Graph 5-17), the difference is even more obvious. Literature (Grundfos, 2008) suggests that at low flow rates the major head losses should be due to recirculation and partly shock losses. Meanwhile, at high flow rates the losses should be mainly due to friction and partly shock losses too. The unfitted model satisfies these suggestions, whereas the fitted model shows some other things. The friction loss should experience an increase as the flow grows but that is not what can be appreciated from the fitted model. This is due to the friction losses in the volute which have a high offset value since they depend on C_{2t} & C_{2r} (see Eq. (11.8.7)). As the flow increases the slip increases too making C_{2t} get lower and therefore making the friction losses in the volute get lower. Meanwhile, the friction losses in the impeller, depend on W_2 which gets higher as the flow grows (see Graph 5-16). That is why in the fitted model the friction losses seem to decrease, while in the unfitted model they only increase (the first one includes the decreasing volute losses while the second one doesn't).



Graph 5-16 Q-H_{loss} contribution of friction losses in impeller and volute

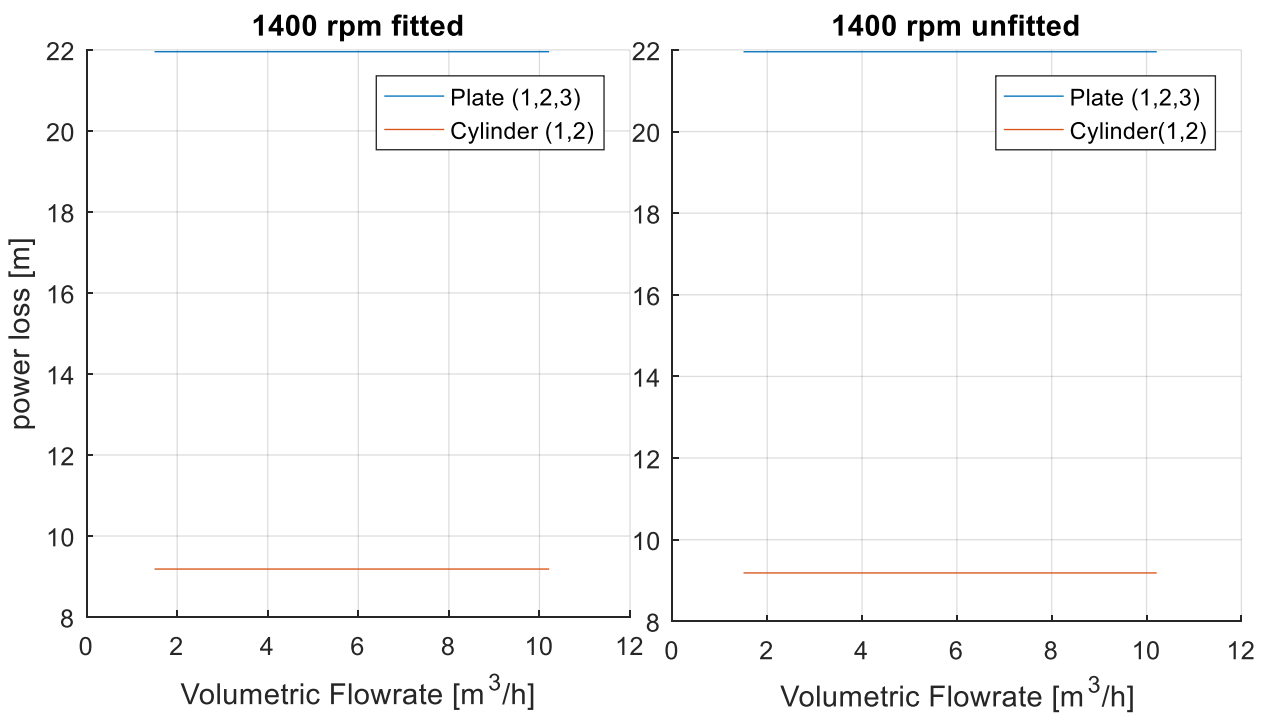


Graph 5-17 Contribution to head loss of all hydraulic losses

Some of these hydraulic losses have constant values in their expressions or determined range of values in their calculations which make the final loss calculation be uncertain. The recirculation uncertainty will be examined on its own in further chapters. The height losses due to contraction and expansion also contain factors of uncertainty like $\xi_{contract}$ from Eq.(11.8.16) which equals 0.07 according to literature (Çengel, et al., 2012) and ξ_{exp} from Eq.(11.8.18) that depends on

the height of the volute (also a range of values). Despite these facts, these losses will not be examined separately since their contribution is minimum.

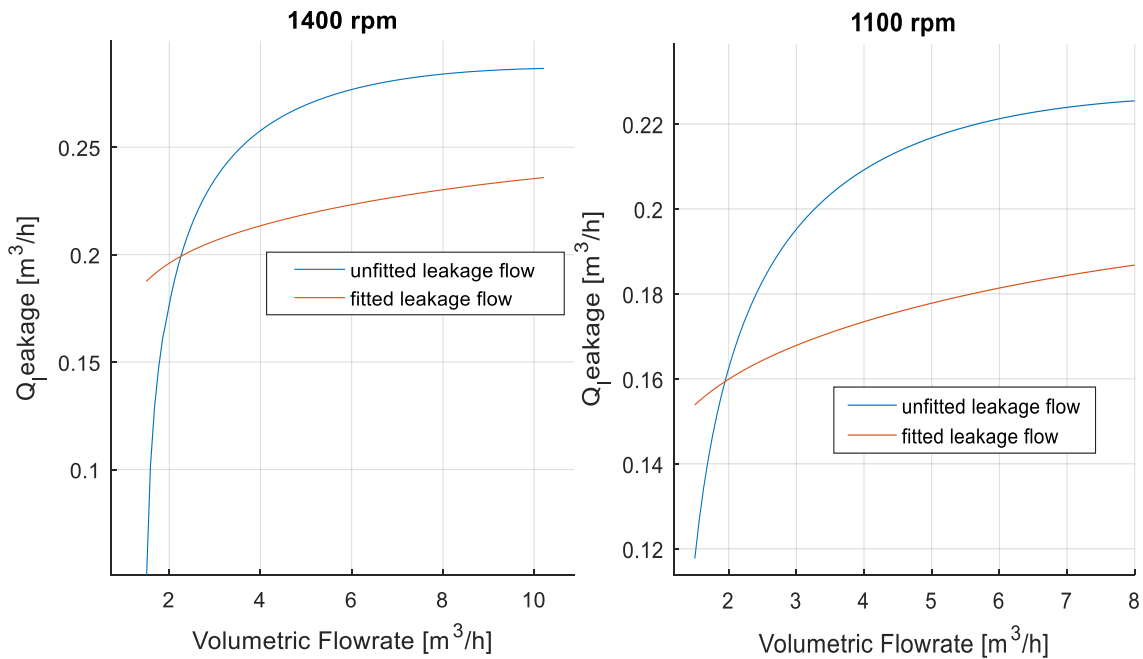
If disk losses are examined more in detail in Graph 5-18, it can be seen that plates have a predominant contribution in the power losses. This is due to plates having a major friction surface with the housing than the cylinders. Plate 3 has the largest surface from all the plates and cylinders, which makes it logic that plates have a higher contribution. There is no difference at all between the fitted and the unfitted model since the disk friction losses haven't been scaled in any way.



Graph 5-18 Power losses due to plate and cylinder friction

Leakage characteristic

In Graph 5-19 it can be seen how the leakage flow increases as the flow increases, both in the fitted and in the unfitted model. Leakage decreases as the rotational speed decreases too. Leakage is affected by the head losses as Eq.(11.8.25) shows. Therefore, when the recirculation coefficient is fitted from 0.001 to 0.0001 the head losses decrease too, making the leakage grow already at low flow rates that is where the recirculation has a greater effect.



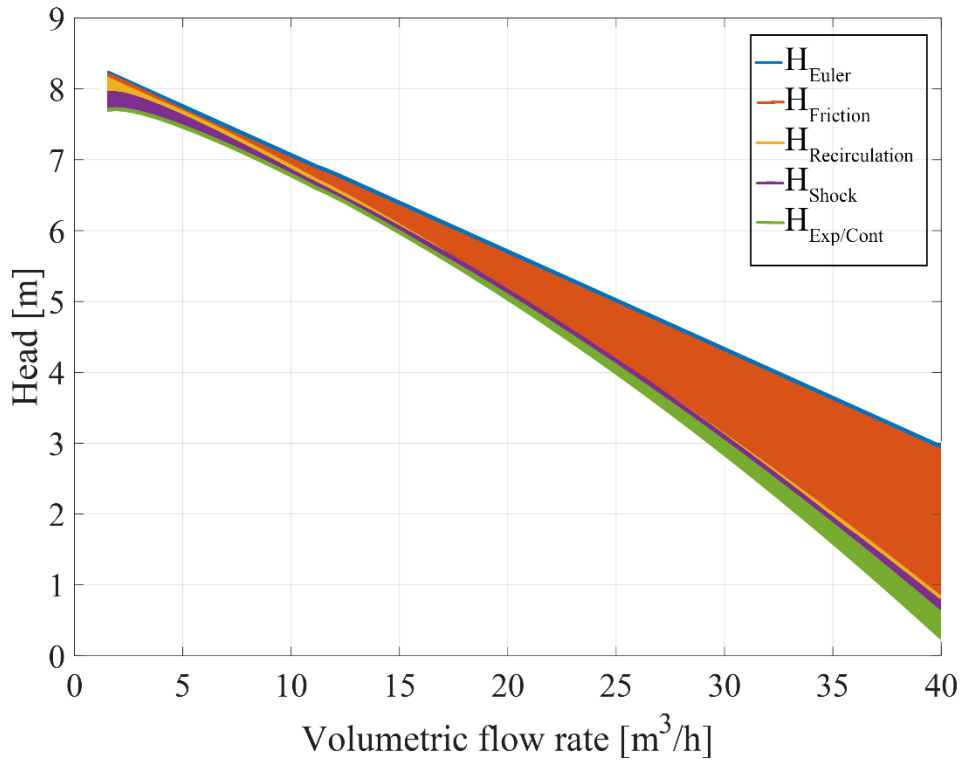
Graph 5-19 Leakage flow as a function of the flow rate

Critique on the fitted model

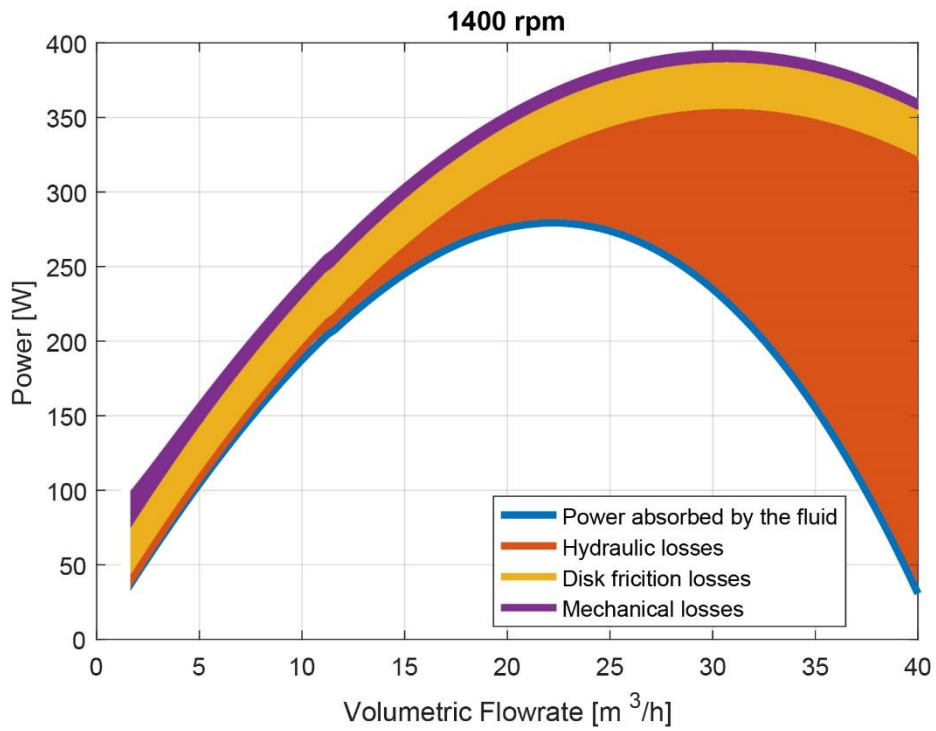
Under ideal circumstances, the ideal fittings would have been minor modifications into the expressions. In this case, minor modifications wouldn't have been enough to fit the model and therefore, some of the general empirical expressions have been severely modified. This is the case of P_{mech} , empirical expression from (Gulich, 2010). In this report, a value 67 times bigger than the one stated in the literature has been required, as well as the modification of ξ_{recir} , which has been reduced 10 times. Secondly, having no previous reference of in which range of values ξ_{volute} should be, this value has been modified in accordance to the interest of this report.

Therefore, given the fact that the fitting is just a scaling of the mathematical model by manipulating the equations and given the lack of similarity between some of the fitted and unfitted plots, the optimization and the uncertainty analysis in the following chapters will be done based on the unfitted model which is fully coherent with the references. The only two fittings that will be further used in the report are the ones for the recirculation losses and for the mechanical losses. Without applying these "corrections", the model plots results with a noticeable deviation from empirical testing (including the tests carried out by the manufacturer). Hence, the recirculation coefficient will be the only fitting further used for the head and the mechanical loss coefficient will be the only fitting used for the power curve.

To conclude the chapter, Graph 5-20 and Graph 5-21 have been plotted without being fitted. These plots illustrate very clearly to which extent and where do the different losses have the greater effect.



Graph 5-20 Reduction of Euler theoretical head due to losses



Graph 5-21 Increase in power consumption due to losses

Chapter 6 Model uncertainty analysis

During the writing of the modeling of the pump, in various occasions sources of uncertainty have been identified in the mathematical expressions due to the fact that they have been simplified, and in most cases factors are based on empirical testing when they should be measured instead with advanced laser based velocity measurements. The following chapter deals with geometrical uncertainties when measuring the impeller's geometry, with uncertainties regarding values of empirical constants and with the obtainment of different values when applying different methodologies to handle the same calculations.

6.1 Geometrical uncertainties in the leakage

The most relevant geometrical uncertainty comes from the calculation of the leakage flow. The size of the gap through which the leakage flow goes through is the most important parameter in the calculation of the leakage. The size of the gap is not constant as it appears in Figure 6-1.

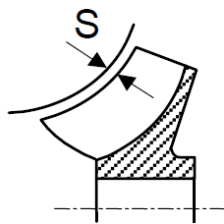


Figure 6-1 Size of the impeller gap "s".
Source: (Gülich, 2010)

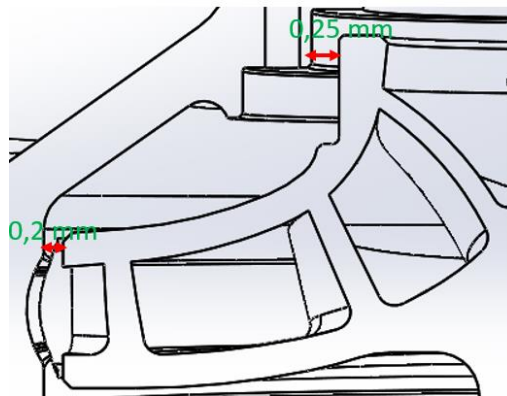
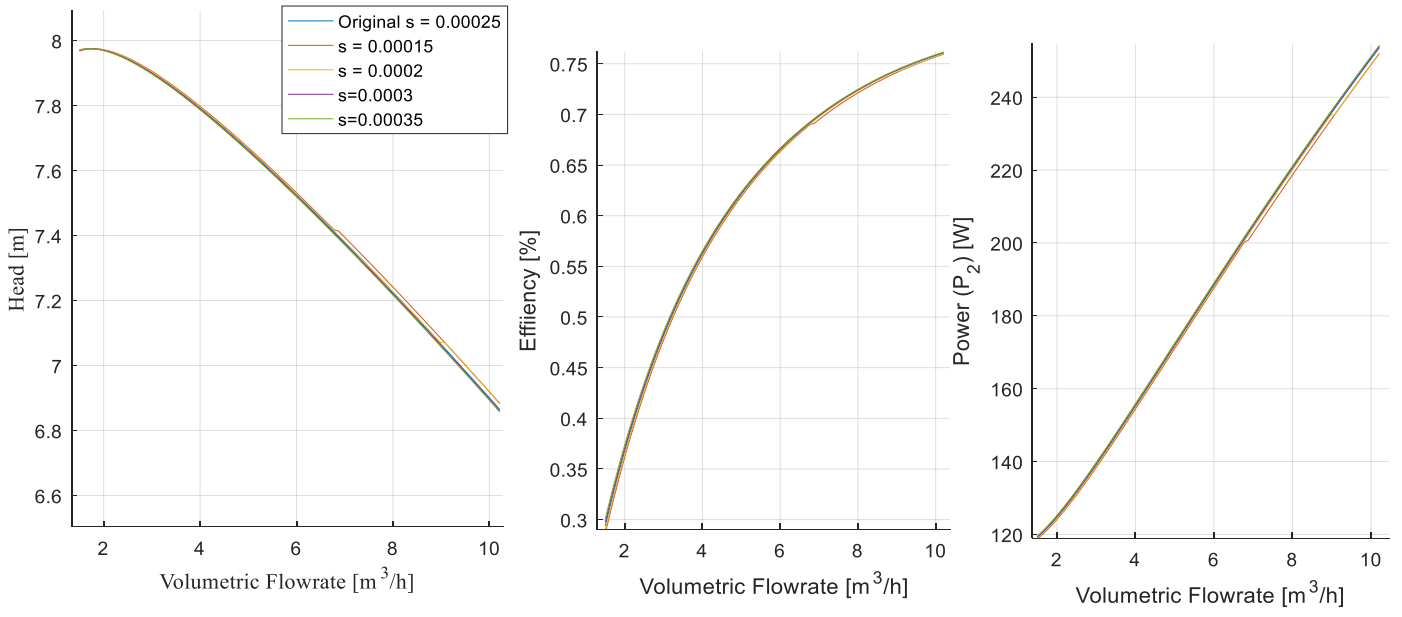


Figure 6-2 Section of impeller and housing for Grundfos NK 32-125/142

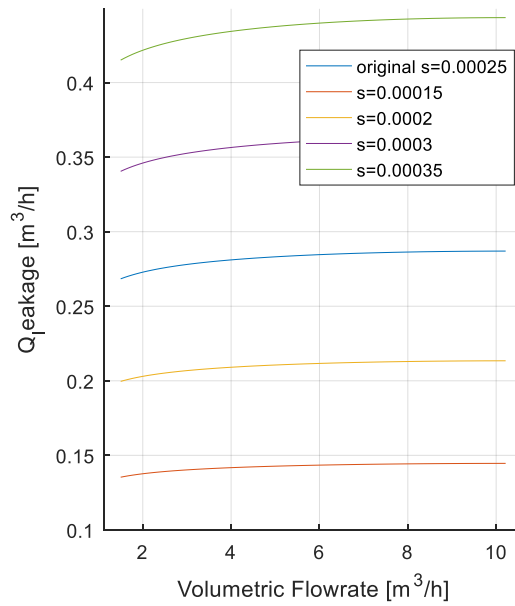
Graph 6-1 shows how varying the width of the gap size affects the head, the efficiency and the shaft power. The size of the gap has been varied from [0.15-0.35] mm. The flow rate is comprised from [1.5-10.28]m³/h given the fact that under that range the values obtained behaved in a rather unpredictable way. The higher limit is set by the highest value of flow from which measures were taken from the test rig.

As it may be seen, the variation between the curves is negligible at the level of head, power and efficiency. Higher variations must be seen at level of leakage flow.

Instead if the effect of varying the gap size is examined at a more concrete level ($Q_{leakage}$) as it is done in Graph 6-2, it can be seen that the change is more notable, becoming the leakage bigger as the size of the gap gets bigger (which would be the most logical result).

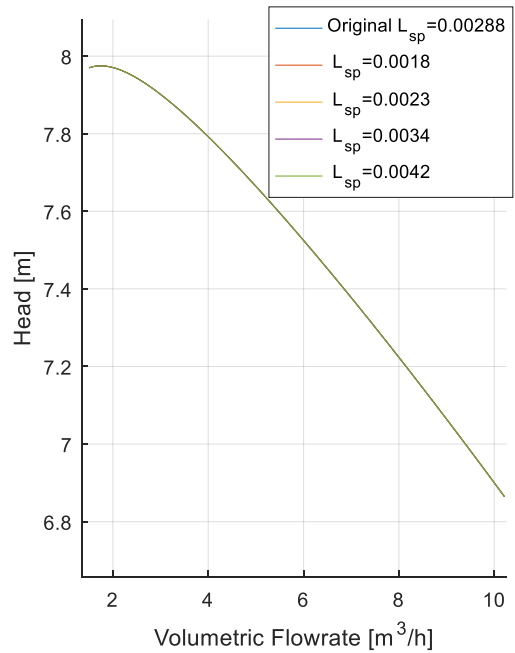


Graph 6-1 Q- η , Q-H and Q-P for varying s



Graph 6-2 Q-Qleakage for varying s

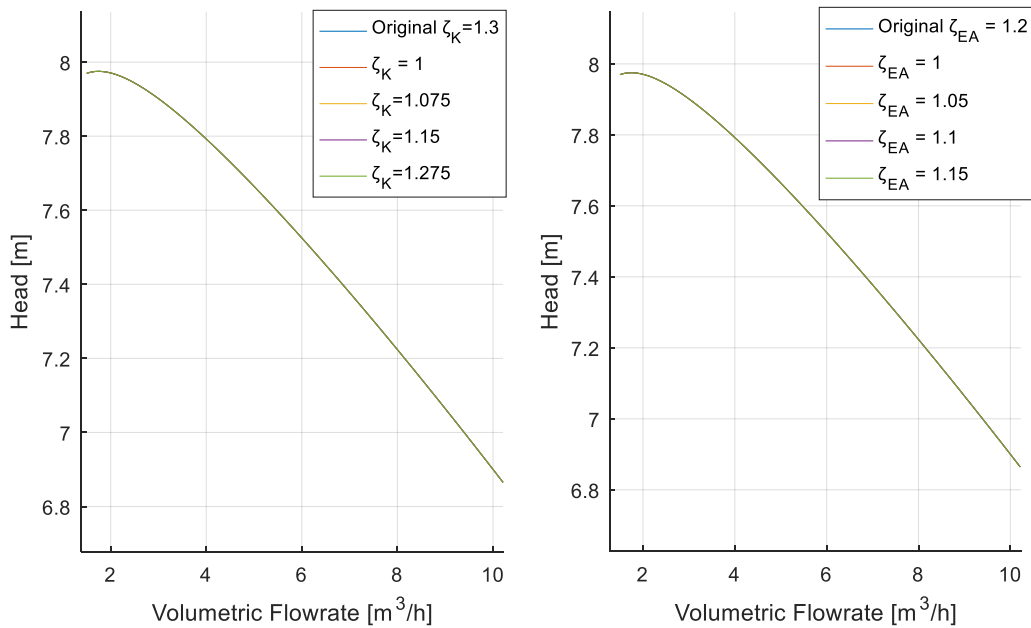
Other uncertain parameters like the length of the gap L_{sp} were also varied. Also, the eccentricity factor e_x was varied. In both occasions, no change was perceived at all. Only the head is plotted in this case



Graph 6-3 Q-H for varying L_{sp}

6.2 Empirical parameter uncertainties in the leakage

In the calculation of the leakage two parameters are given with fixed values inside a range; ζ_{EA} the loss coefficient in inlet and outlet with values ranging from [1,1.2] and ζ_K the loss coefficient per chamber with values ranging from [1,1.3]. In both cases the maximum value for them was taken to plot the worst circumstances. In both cases, the two parameters turned out to have a null effect on the Q-H, Q- η and Q-P curves.



Graph 6-4 Q-H when varying ζ_{EA} and ζ_K

6.3 Empirical parameter uncertainties in losses

A simple model was used to describe the losses due to recirculation. (Grundfos, 2008) states there are no simple models to describe the behavior of recirculation zones and to which extent it occurs. Despite this statement, (Tuzson, 2000) uses Eq.(6.3.1) to calculate the power loss due to recirculation. This power calculation uses a recirculation loss coefficient that can take values ranging from [0.001-0.007]. Varying the value of $\xi_{recir.}$ has important repercussions as it can be seen in the fitting of the model. As it can be observed from Graph 6-5 and Graph 6-6, the biggest influence of recirculation is in the head. Throughout the report this value has been set to 0.0001

$$P_{recir.} = \xi_{recir.} \cdot \omega^3 \cdot d_1^2 \cdot \left(1 - \frac{Q_{impeller}}{Q_{BEP}}\right)^{2.5} \quad [W] \quad (6.3.1)$$

Where,

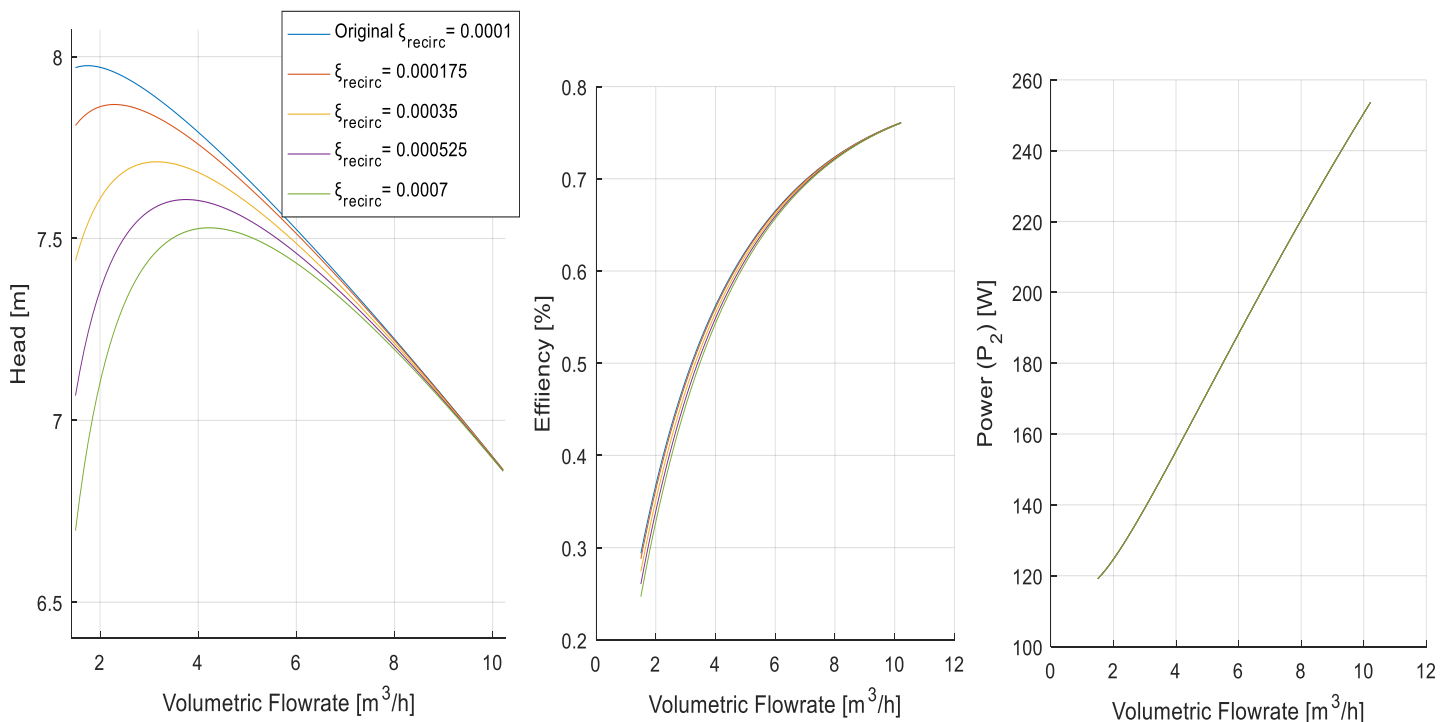
$\xi_{recir.}$ Has a value between 0.0001 and 0.0007 according to literature (Tuzson, 2000)

ω is the rotational velocity [rad/s]

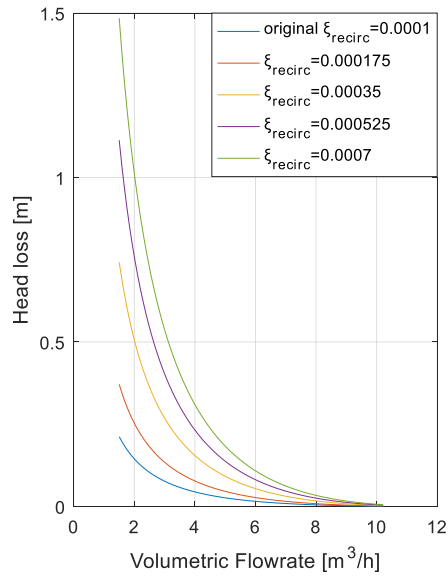
d_1 is the inlet diameter [m]

$Q_{impeller}$ flow rate through the impeller [m³/s]

Q_{BEP} flow rate at the best efficiency point [m³/s]



Graph 6-5 Q-H, Q- η , Q-P_{hyd} when varying the recirculation coefficient



Graph 6-6 Q-H_{loss} due to varying the recirculation coefficient

Other empirical parameters

Other losses like the contraction loss, also contain uncertain empirical parameters obtained from (Çengel, et al., 2012). This loss contains the parameter $\xi_{contract}$ present in Eq.(11.8.16). Given the difficulty to measure the angle of gradual contraction from Figure 11-11, the chosen value for $\xi_{contract}$ can be not very accurate. Despite this, the effect from the contraction losses in the final head are so small compared to the expansion losses and to the final head losses (see Graph 5-17), that $\xi_{contract}$ was considered a minor loss.

6.4 Impacts of different models for slip factor

This section will analyze how some formulations for the same phenomena have different effects on the overall pump characteristics. Depending on the literature that is used, every author recommends different expressions and methodologies. Most remarkably, the calculation of the slip factor was the phenomena that has the dissimilar methods. These different methods were exposed step by step in Appendix 11.6.

Both methods were used in the model to compare the results obtained with them. As it may be observed from Figure 6-3, there's an obvious difference from one head to the other (1.087 m). The Gülich method was chosen for the calculation since the formulas from Dixon had more uncertainty given the fact that some of the factors in the formulas were extracted from graphs like the one from Figure 11-9.

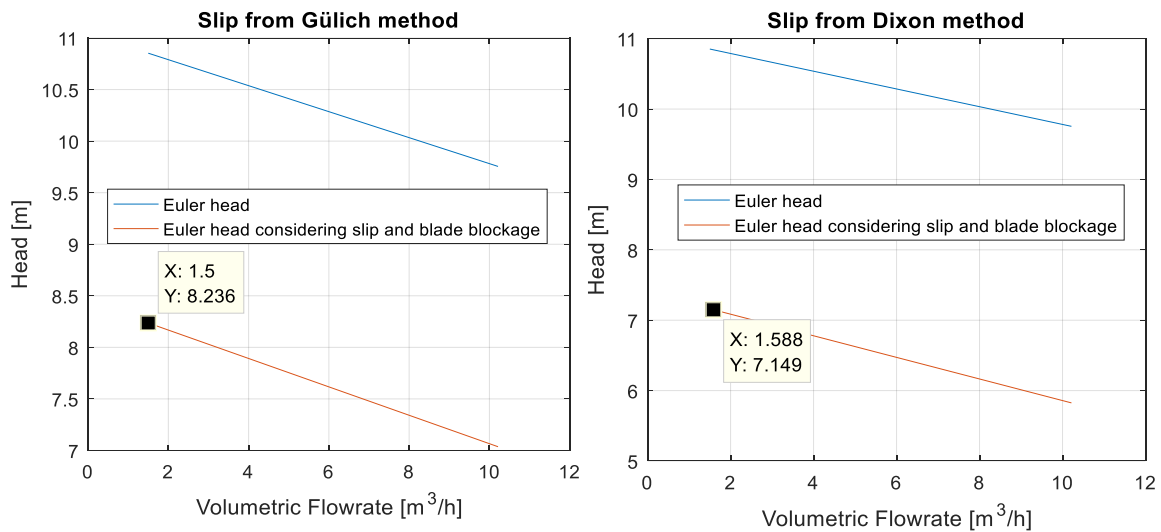


Figure 6-3 Comparison in head reduction employing two different methods to calculate the slip

Chapter 7 Optimization in the impeller's design

The optimization criteria depend highly on what performance aspect of the pump wants to be improved. Different design parameters will be affected if the head wants to be increased, whether the flow wants to be increased or the power.

A pumped hydro storage reservoir requires high heads to be able to obtain the highest potential energy as possible in the discharge. Therefore, the optimization will be focused in improving the pump's head. Additionally, it should also be decided whether the high heads should be accomplished at low flow rates or at high flow rates. Pumped hydro storage reservoirs require very high flow rates, consequently the optimization criteria will be:

Increasing the head at high flow rates, keeping the efficiency as high as possible at high flow rates too

According to (Gulich, 2010) there are a series of possibilities that can be implemented to increase the head:

- Under-filled impeller blades at the suction side of the blade at the outlet (Figure 7-1)
- Welding-up the blade's junction lines (Figure 7-2)
- Reduction of hydraulic losses
- Greater: d_2 , Z_{La} , b_2 and β_2
- Fluid counter-swirl at the inlet (Figure 11-5)

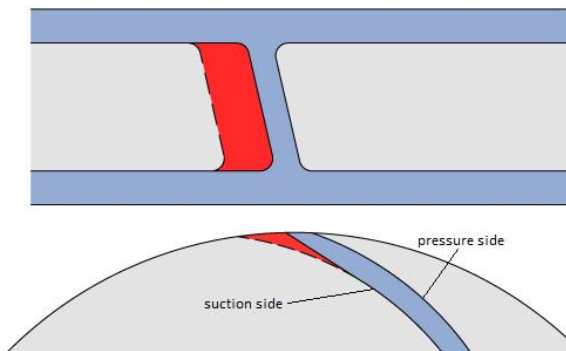


Figure 7-1 Under filing (red) at the outlet suction side. Source: (Anon., 2017)

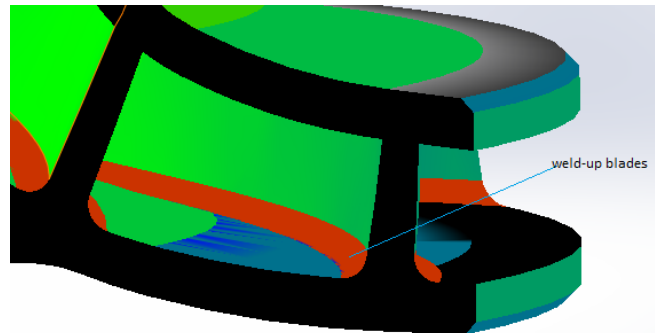
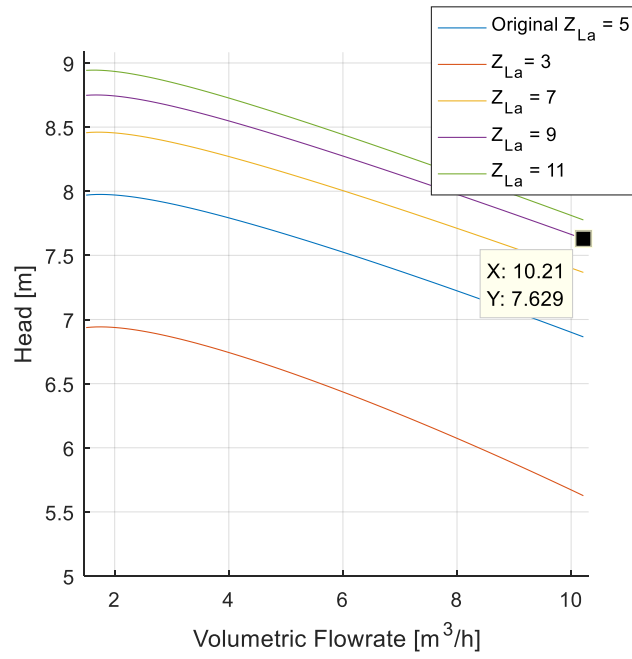


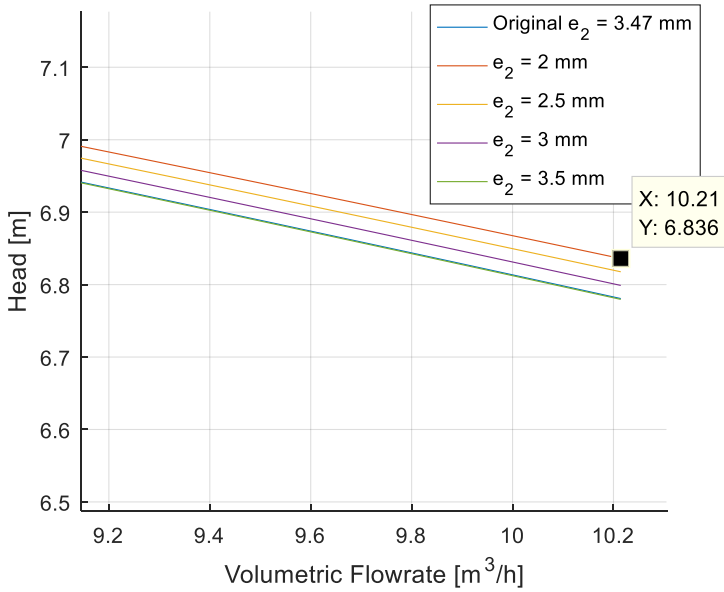
Figure 7-2 Right-plane section where the welded rounded up edges can be seen

The options that are more tangible and easily varied within the model are geometric variations in the design. Therefore, variations such as the number of blades, the blade angle, the blade height, the separation of the vanes, the blade thickness and the impeller outlet width will be examined separately.

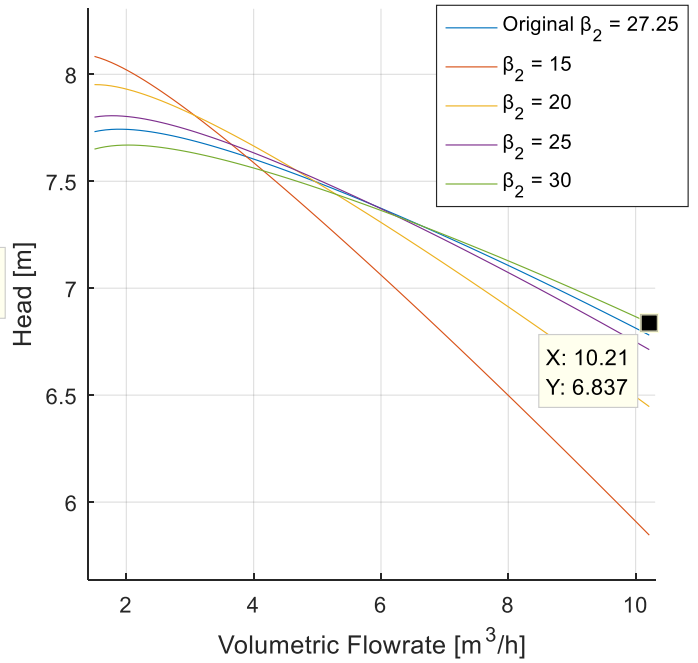
The biggest change in the head was accomplished by varying the number of blades as it can be seen from Graph 7-1, Graph 7-3 and Graph 7-2. Therefore, the first measure implemented will be varying the number of blades.



Graph 7-1 Effect on H when varying the number of blades



Graph 7-3 Effect on H when varying the thickness of the blade at the outlet



Graph 7-2 Effect on H when varying the outlet blade angle

7.1 Number of blades Z_{La}

Varying the number of blades influences in various phenomena and losses occurring in the impeller such as:

- Blade blockage (see Eq.(11.5.2))

Blade blockage is directly affected by the number of blades. The blade blockage factor τ_2 is directly proportional to Z_{La} which translates to an increase in the velocity at the outlet when more blades are added.

- Slip (see Eq.(11.6.2))

Slip refers to flow deflection caused by the blades meaning that the more blades the impeller has the better will the flow follow the blades. The slip factor γ is inversely proportional to Z_{La}

- Shock losses (see Eq.(11.8.10))

Shock losses are caused by deceleration of the flow produced when it collides with the thickness of the blade. Therefore ξ_{shock} is directly proportional to Z_{La} meaning the more blades the impeller has the more shock losses there will be

- Leakage flow (see Eq.(11.8.30))

The calculation of the axial velocity c_{ax} of the fluid inside the gap is counted “i” times for the number of chambers that the impeller has. The number of chambers is going to increase when more blades are added to the pump since there are going to be more chambers. The leakage flow is directly proportional to Z_{La}

Despite some losses getting bigger with the number of blades, the most affected phenomena is the slip, therefore the overall contribution of introducing more blades is positive.

To decide on by what number should the blades be increased it should be acknowledged that an odd number of blades is seen as the wiser choice given the higher instability that even number of blades give (Quora, 2015) .This is due to the stress being worse distributed in symmetrical designs. Secondly, the Q-H plots should be examined directly to see how the curvature of the plot behaves with varying Z_{La} . According to (Gulich, 2010), the flatter the curve gets the more the risk of instability increases. Thirdly, the hydraulic efficiency is also a meaningful value to keep in mind

As it can be seen from Graph 7-1 the more the Z_{La} is increased the more the head rises. Bearing in mind the above paragraph, the curve with 11 blades starts to not comply with the “CFC” criteria (constantly falling curve). This means the region between Point A and Point B has two possibilities—at either flow Q_a or Q_b .

To that end, 9 blades was considered to be the best option (see Graph 7-1 and Graph 7-4)

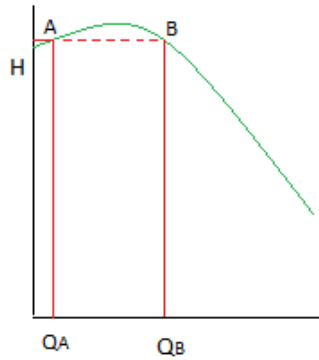
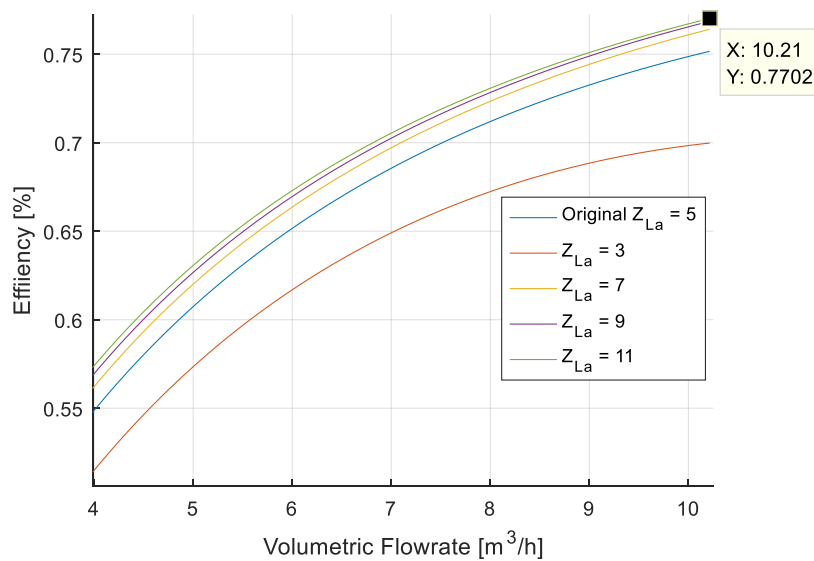


Figure 7-3 Illustration on unstable pump curves



Graph 7-4 Hydraulic efficiency for 9 blades

7.2 Blade angle β_2

According to literature (M.G.Patel, 2013), the blade exit angle has a significant and equal effect on the head and the efficiency. With the increase in the blade exit angle the performance of the centrifugal pump increases. Obviously, the stability of the of the pump cannot be compromised. (Gülich, 2010) states the value of the exit blade angle must be comprised between 15 and 45°. The same principles of instability as for the number of blades apply also.

Varying the outlet blade angle affects:

- Velocity triangle (see Eq.(11.3.5))

Increasing β_2 makes C_{2t} higher which rebounds directly into the theoretical head.

- Blade blockage (see Eq.(11.5.2))

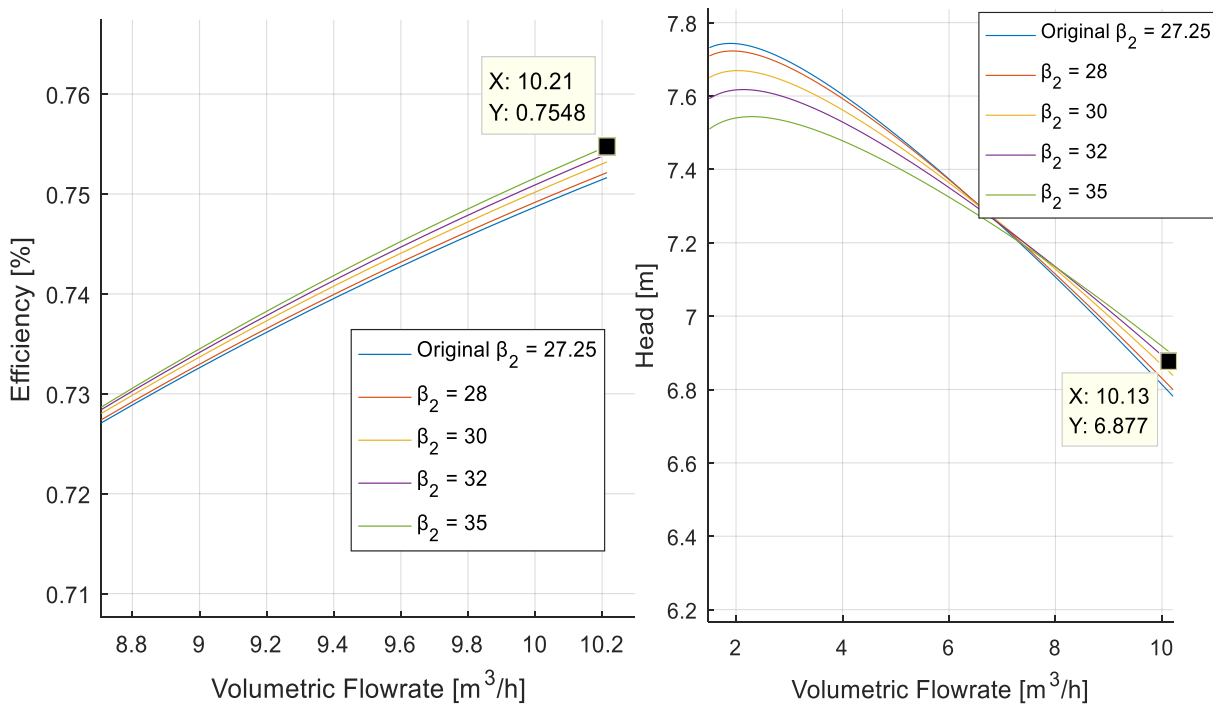
Increasing β_2 decreases the blade blockage factor τ_2 , decreasing the corrected radial velocity at the outlet

- Slip ((see Eq.(11.6.2))

When β_2 increased the slip factor γ decreases having a positive effect in C_{2t} higher which rebounds directly into the theoretical head.

As it can be observed from Graph 7-5 the most significant change in efficiency and head occurs from $\beta_2 = 28^\circ$ to $\beta_2 = 30^\circ$, from then on, the increase ceases to be so significant. Additionally, with angles above 30° , the “CFC” criteria doesn’t appear as clear as it does with smaller angles.

To that end, a $\beta_2 = 30^\circ$ was chosen as the optimum value.



Graph 7-5 Q-H , Q- η for different outlet blade angles

7.3 Blade outlet thickness e_2

Varying the blade outlet thickness will directly affect the following phenomena:

- Blade blockage (Eq.(11.5.2))

Varying the thickness of the blade at the outlet will have a positive repercussion if the thickness is lowered and negative otherwise. The blade blockage factor τ_2 and the blade thickness e_2 are directly proportional.

Testing shows head increases infinitely when the blade thickness is reduced to values near 0, but there are certain mechanical strength requirements that must be fulfilled so that the

impeller will resist blade stresses. According to (Gülich, 2010), these requirements are fulfilled when $\frac{e_{1/2}}{d_2} = [0.016 - 0.022]$. The pump Grundfos NK 32-125/142 is designed with an inlet blade thickness of $e_1 = 2.17 \text{ mm}$ and an outlet blade thickness of $e_2 = 3.47 \text{ mm}$. The outlet diameter of the impeller is $d_2 = 142 \text{ mm}$. Therefore, the ratios of this impeller would be around:

$$\frac{e_1}{d_2} = 0.01528 \quad [-] \quad (7.3.1)$$

$$\frac{e_2}{d_2} = 0.02444 \quad [-] \quad (7.3.2)$$

Where,

e_1/e_2 are the inlet and outlet thicknesses of the blades [mm]

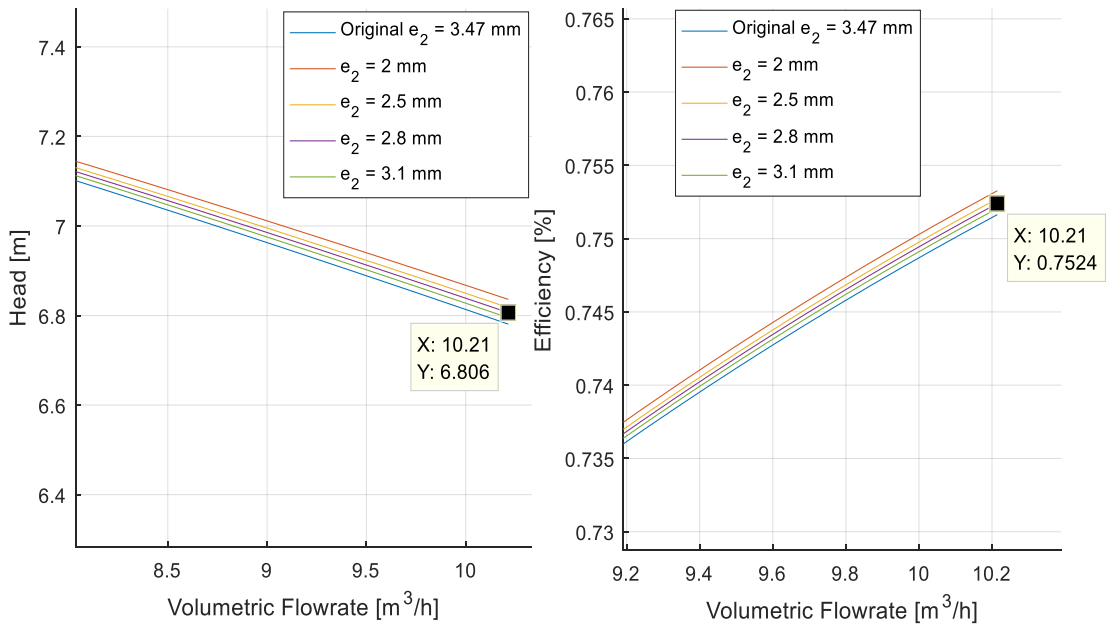
d_2 is the outlet diameter of the impeller [mm]

Nevertheless, e_2 cannot be varied independently from e_1 since it is all the same blade and a geometrical relation must be maintained between the inlet and the outlet.

$$\frac{e_2}{e_1} = 1.599 \quad [-] \quad (7.3.3)$$

To carry out this optimization e_2 will be varied in the measure that e_1 is also varied, maintaining the relation of 1.599.

A value of $e_2 = 2.8 \text{ mm}$ was chosen which complies with the ratio $\frac{e_{1/2}}{d_2} = [0.016 - 0.022]$.



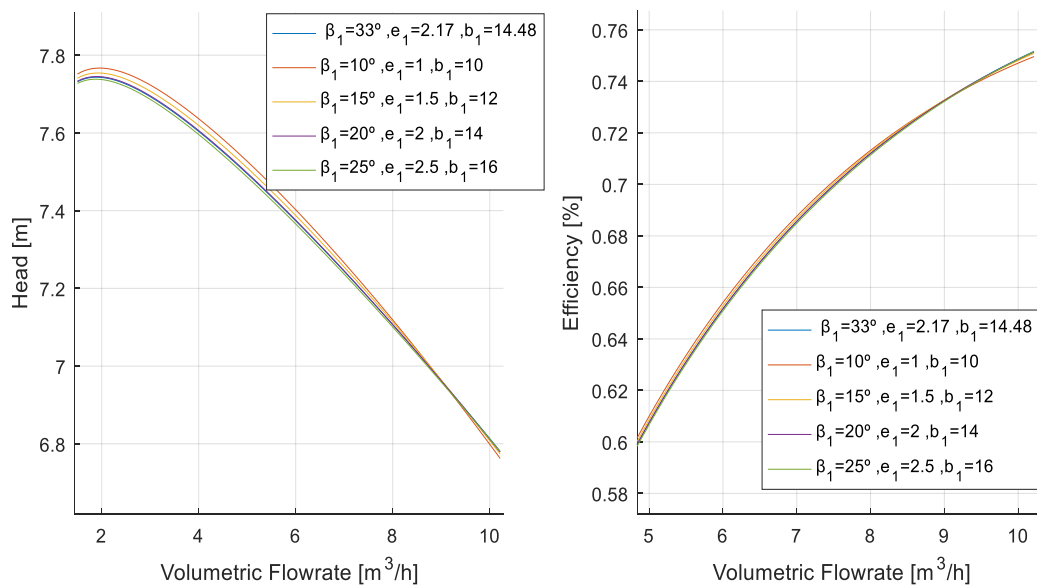
Graph 7-6 Q-H and Q- η for varying blade outlet thickness

7.4 Blade height at the outlet b_2

The variation of blade height is strictly limited to the pump housing dimensions; therefore 1 mm variation can already mean that the upper plate collides with the casing. Given the situation, the height of the blades remains unvaried.

7.5 Variations in the inlet parameters

As it may have seen appreciated from the above variations, none of them were done in the inlet parameters (β_1, e_1, b_1). That's because varying inlet parameter has a negligible effect in the head or the efficiency.



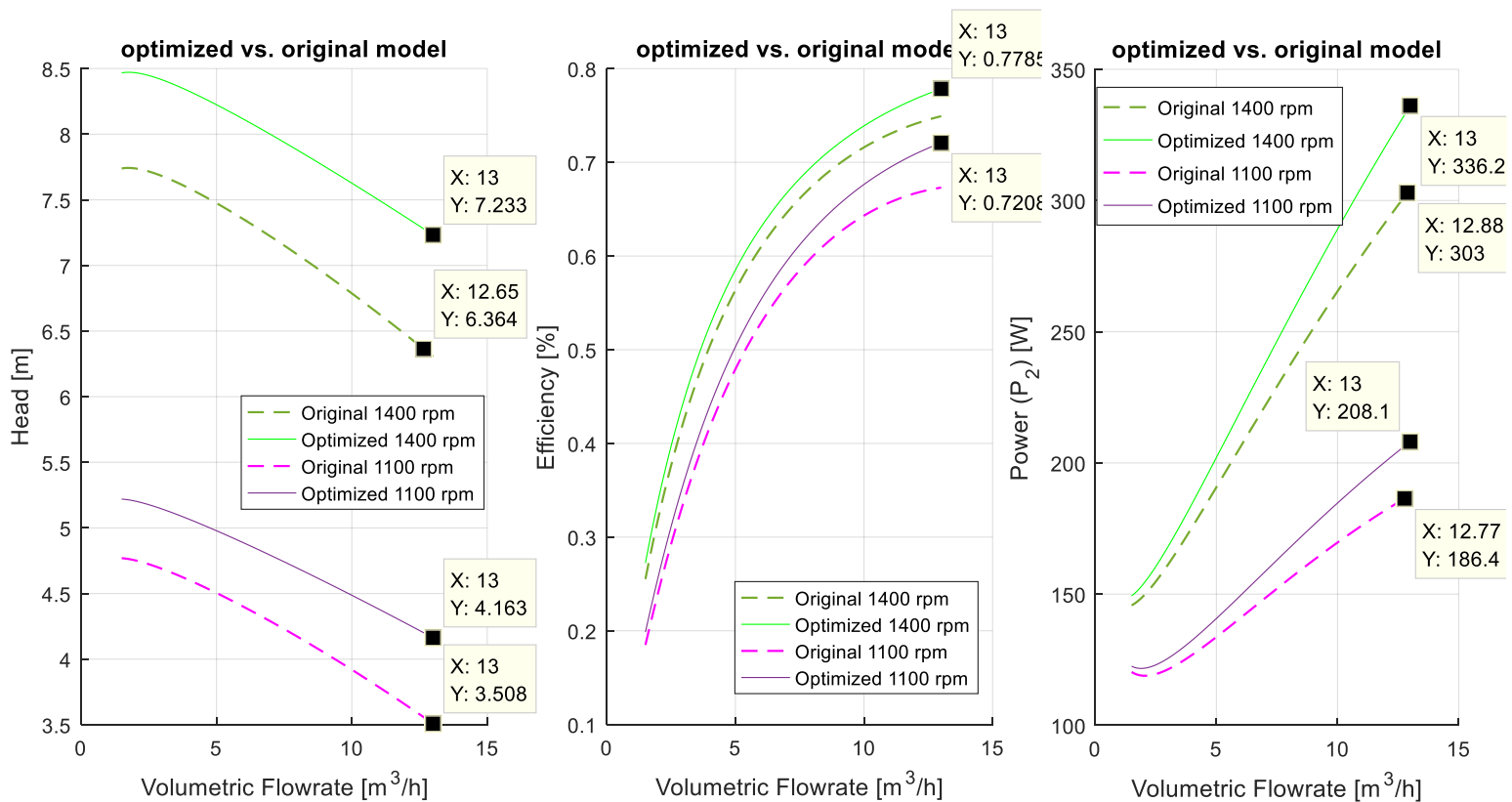
Graph 7-7 Q-H, Q- η when varying diverse inlet parameters simultaneously

7.6 Final design

Based on the analysis carried out in the previous sections, the new model of the Grundfos pump was made. The CAD-drawings of the new impeller was made from draft following the surface geometries observed in the CAD-Drawings provided by Grundfos.

| Description | Symb | Initial | Final | unit |
|--|-----------|---------|-------|--------|
| Outlet blade angle | β_2 | 27.28 | 30 | ° |
| Thickness of the blades at inlet | e_1 | 2.17 | 1.75 | mm |
| Thickness of the blades at outlet | e_2 | 3.47 | 2.8 | mm |
| Number of blades | Z_{La} | 5 | 9 | blades |

Table 7-1 Summary table with optimizations introduced



Graph 7-8 Q-H, Q-η and Q-P₂ for the optimized pump model

Pump manufacturing

The pump will be manufactured in 2 separate parts to facilitate the assembly. The top part has extruded cuts which follow the shape of the blades in order that both parts fit to one another. The optimized pump will be manufactured in hard foam which will make the impeller much lighter but vulnerable.

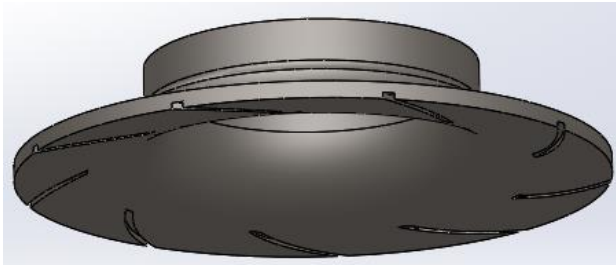


Figure 7-5 Top part of the impeller

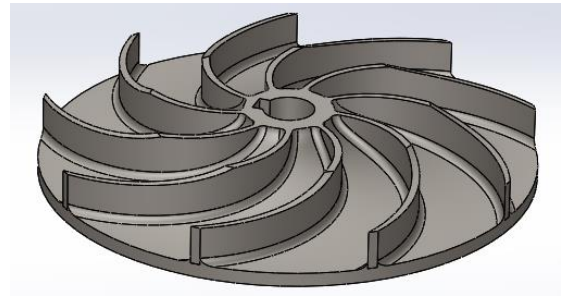


Figure 7-4 Bottom part of the impeller

Chapter 8 Up-scaling of impellers for the centrifugal pumps in the hybrid wind-hydro power plant

In this chapter, a large-scale centrifugal pump will be dimensioned to fit the hydro storage plant for the hybrid wind-hydro power plant. The validated model for the small tested impeller will be used for this up-scaling. The most common method to use to up-scale centrifugal pumps are the affinity laws. These laws use two types of scaling:

- Scaling of rotational speed
- Geometric scaling

In both scalings the same 3 pump parameters are varied Q, H and P . Nevertheless, these rules can only be applied with pumps of the same geometric family which means that the velocity triangles have to be geometrically similar before and after the scaling.

In the following table, the pump characteristics obtained from the optimized small pump are compared with the requirements the hydro-storage pump will have. As it can be seen the pump has to be scaled in all its characteristics.

| | Small scale optimized impeller | Large scale hydro-storage impeller | Up-scaling by |
|---------------------------------|--------------------------------|------------------------------------|---------------|
| Power (P_2) | 280 W | ~1.1 MW | x3900 |
| Head | 7.23 m | 100 m | x13 |
| Flow | 13 m ³ /h | 3600 m ³ /h | x360 |

Table 8-1 Pump characteristic variation from small scale pump to large scale pump

Furthermore, it cannot be assumed that the optimizations carried out in the small-scale impeller are also going to be valid for a big impeller. Impellers with very large flow requirements and large heads might need different number of blades or blade angles.

Therefore, it can be concluded that the affinity laws will not be valid for this case and that 2 different situations will have to be approached;

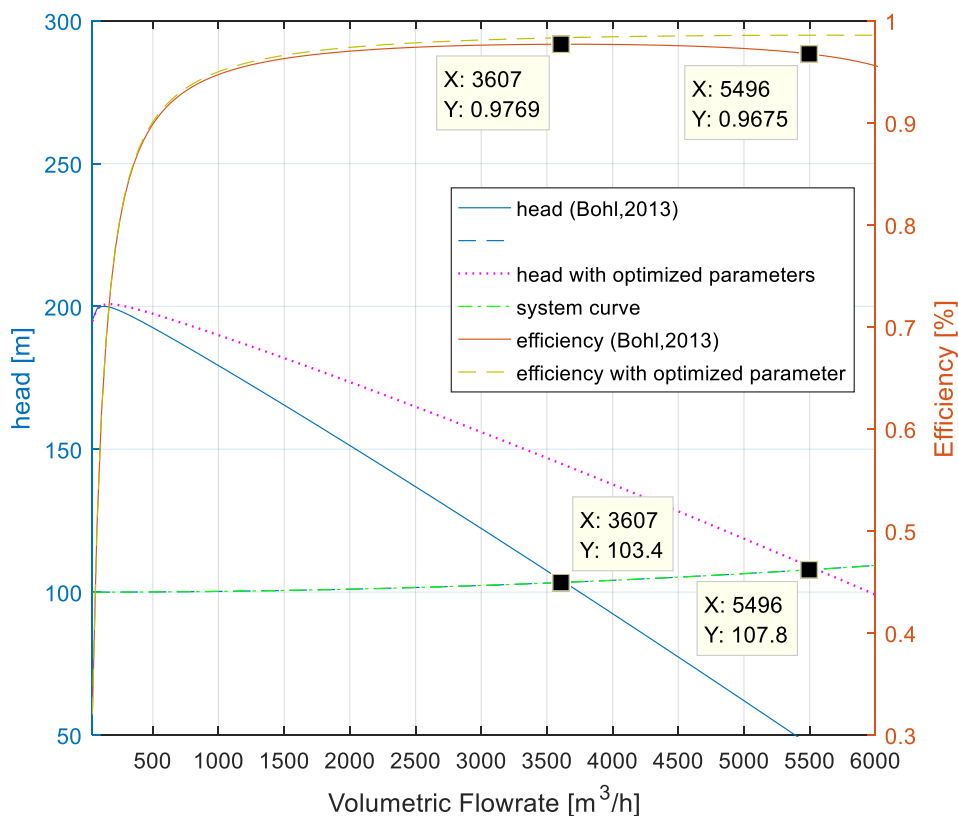
- 1st case using the optimized values of $\beta_2 = 30^\circ$ and $Z_{La} = 9$
- 2nd case calculating the required:
 - Outer diameter d_2
 - Inlet and outlet height of the impeller b_1/b_2
 - Inlet and outlet blade angles β_1/β_2
 - Number of blades Z_{La}

To carry out the 2nd case, the calculations will be based on (Bohl, 2013). Detailed calculations on how to obtain the above mentioned geometrical parameters appear in Appendix 11.9.

| | | 2 nd case | 1 st case | units |
|----------------------------|------------|--------------------------|----------------------|-------|
| | Symb. | Value using (Bohl, 2013) | Optimized values | |
| Outlet diameter | d_2' | 612.9 | 612.9 | [mm] |
| Inlet diameter | d_1' | 239 | 239 | [mm] |
| Inlet blade height | b_1' | 129.4 | 129.4 | [mm] |
| Outlet blade height | b_2' | 81.08 | 81.08 | [mm] |
| Outlet blade angle | β_2' | 19.55 | 30 | [°] |
| Inlet blade angle | β_1' | 24.27 | 33.08 | [°] |
| Number of blades | Z_{La}' | 7 | 9 | [-] |

Table 8-2 Summary table on used values for large-scale impeller

The listed values from the above table appear plotted in Graph 8-1. From the plot it can be seen that the optimized-scaled-impeller would have higher head at higher flow rates. This result was expected since that was the main objective of the optimization. In this case the BOP³ and the BEP⁴ coincide at a flow rate of 3607 m³/h. The efficiency for large scale pumps increases considerably compared to the efficiency the lab pump has.

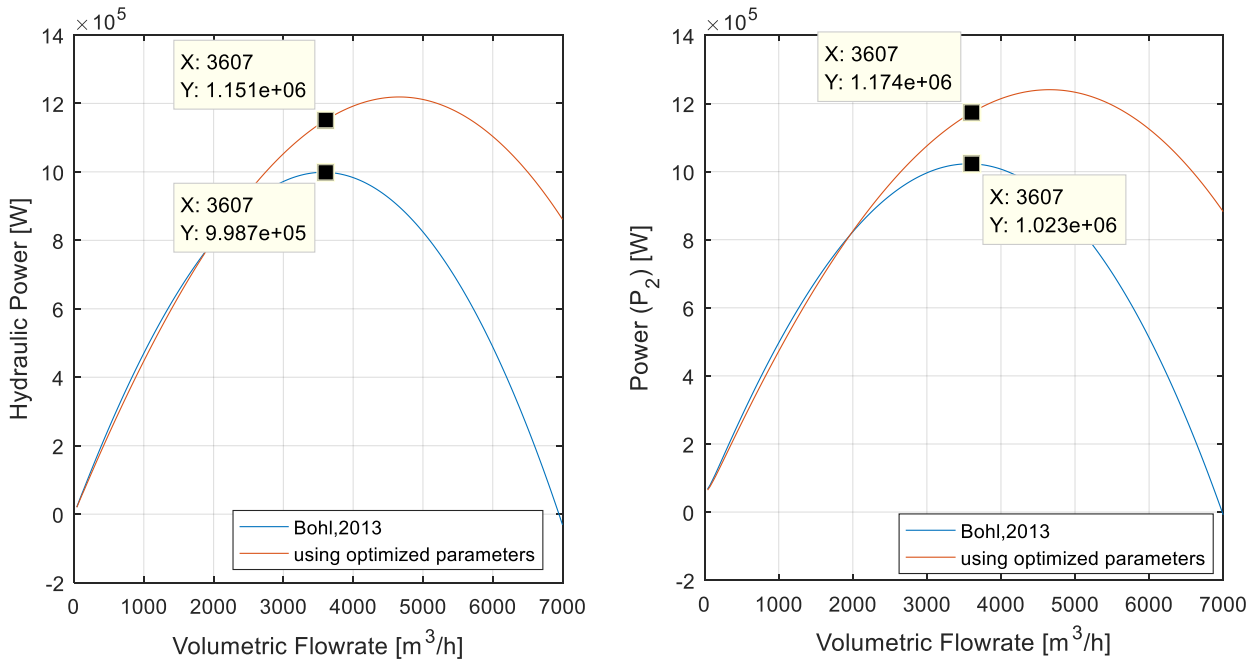


Graph 8-1 Q-H, Q-η comparing the use of parameters calculated with (Bohl, 2013) and the parameters obtained from the small-scale optimization

³ BOP stands for Best Operation Point

⁴ BEP stands for Best Efficiency Point

In Graph 8-2, it can be seen that P_2 is slightly over 1 MW as expected and P_{hyd} is below P_2 as expected too. Considering that the electrical motor efficiency is $\sim 100\%$, the required electrical power for the pump will be of around 1.03 MW.



Graph 8-2 Q- P_2 and Q- P_{hyd} obtained with the optimized parameters and the (Bohl,2013) parameters

8.1 Uncertainties in the scaled geometrical parameters

As it can be appreciated from the calculation methodology stated in Appendix 11.9, (Bohl, 2013) uses a lot of empirical parameters obtained from graphs in its calculations. Despite some parameters like de outer diameter d_2 being calculated with diverse methods to get the most accurate result, these methods contain numerous sources of uncertainty.

In previous chapters, the recirculation coefficient $\xi_{recir.}$ and the mechanical loss coefficient φ_{mech} , were chosen to be the only fittings to include in the model. For the scaling, the model was executed without any fittings, which means that the values of this two coefficients are inside the range of values given by the literature. For the scaled pump, a value of $\xi_{recir.} = 0.005$ was chosen, and the original value of $\varphi_{mech} = 0.0045$ was maintained.

8.2 Conclusions part 2

Part 2 was structured with the following sequential chapters:

- Pump modeling
- Model fitting and validation
- Model uncertainty analysis
- Impeller optimization
- Model-based up-scaling of the impeller

The fitting and validation concluded that some empirical parameters used in the model had to be severely altered to avoid important deviations from the test results and the manufacturers plots. Some of these alterations were excluded from the following sections, while the recirculation loss fitting and the mechanical loss fitting had to be maintained for better coherence.

The uncertainty analysis revealed the leakage flow calculation contains the most uncertain geometrical values but the recirculation contains the most uncertain empirical parameters with the greatest effect.

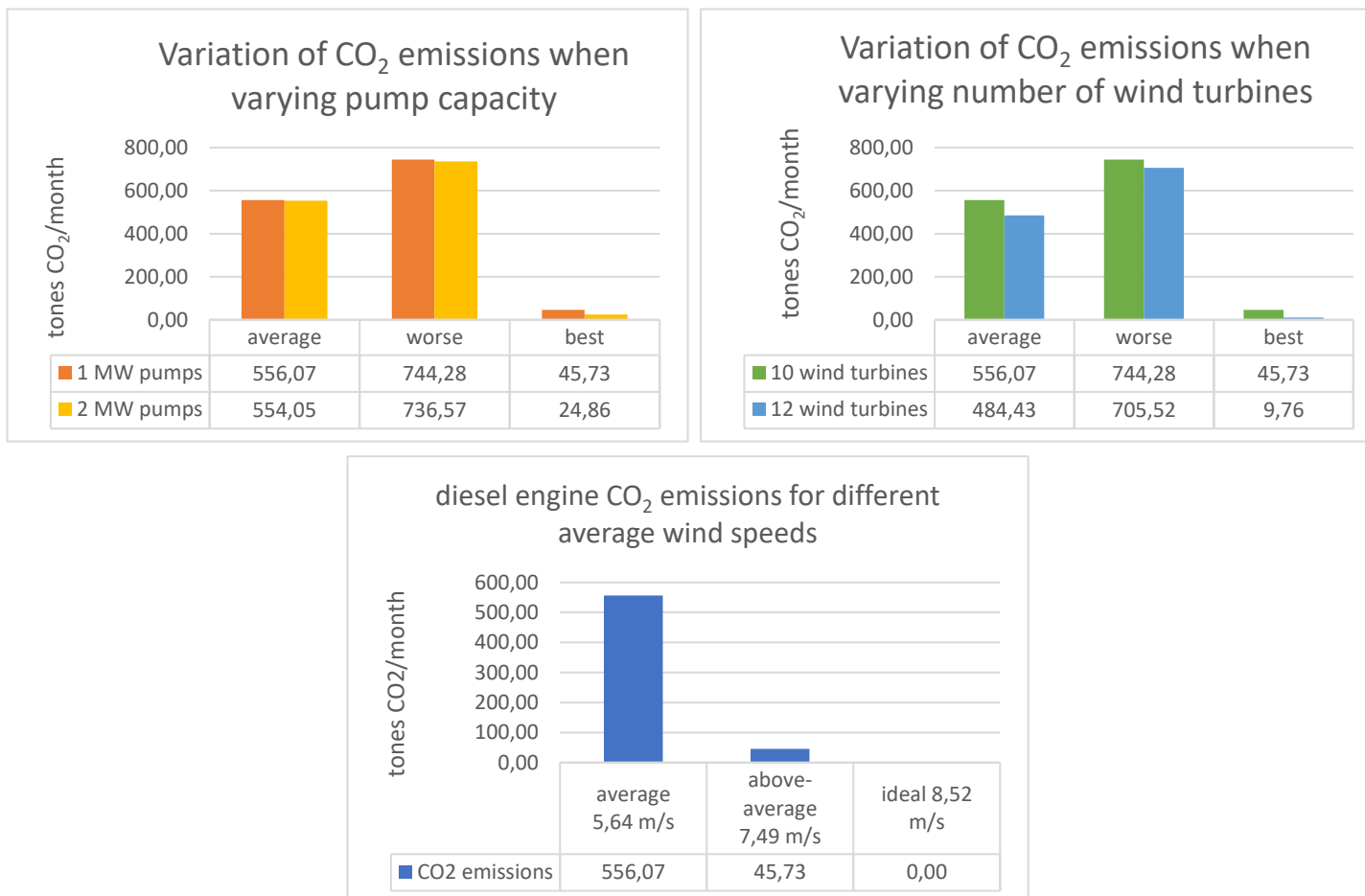
The impeller optimization allowed to see what parameters have a greater influence in the pump characteristics. The optimization concluded that the number of blades, the outlet blade angle and the blade thickness were the most relevant parameters to vary.

Lastly, and following the results obtained from the optimization, a larger impeller suitable for hydro-storage was designed. The power requirements of said pump were given from the previous dimensioning done for the hybrid wind-hydro power plant in Part 1. Two different configurations were used; the optimized one and a newly calculated one. The second one ended up being better for the purpose.

Chapter 9 Conclusion

Hybrid wind-hydro power plants could become more feasible and eco-friendly than batteries in locations where average wind speeds reach 8.5 m/s. In the island of el Hierro the average wind speeds range from [5.6-7.5]m/s, which does not meet the threshold wind condition.

Pump capacity is looked into as one possible hypothesis to reduce CO₂ emissions. Increasing pump capacity does have an effect reducing the emissions, but it has to be bared in mind, that increasing the pump capacity must also involve increasing the storage capacity of the upper reservoir. The second hypothesis is to increase the number of wind turbines. This option has a greater effect but will be indeed a more expensive alternative than the first one. Lastly, the option of placing the hybrid power plant in a windier place is contemplated. This last option would not be an option in real life since once such infrastructure is installed it won't be removed. The average wind speed in el Hierro is of 5.64 m/s which involves a high usage of the auxiliary Diesel engines which emit under this wind conditions 556 tones CO₂ /month. Under the best wind conditions in el Hierro, this number is reduced to 45.73 tones CO₂ /month. The problem is that in el Hierro only 112 days out of 365 have above average wind conditions. Under the ideal wind conditions, the auxiliary diesel engines would not be necessary at all, but this location only experiences winds above 8.5 m/s 52 days in a year.



Graph 9-1 Different monthly emissions for different varying scenarios

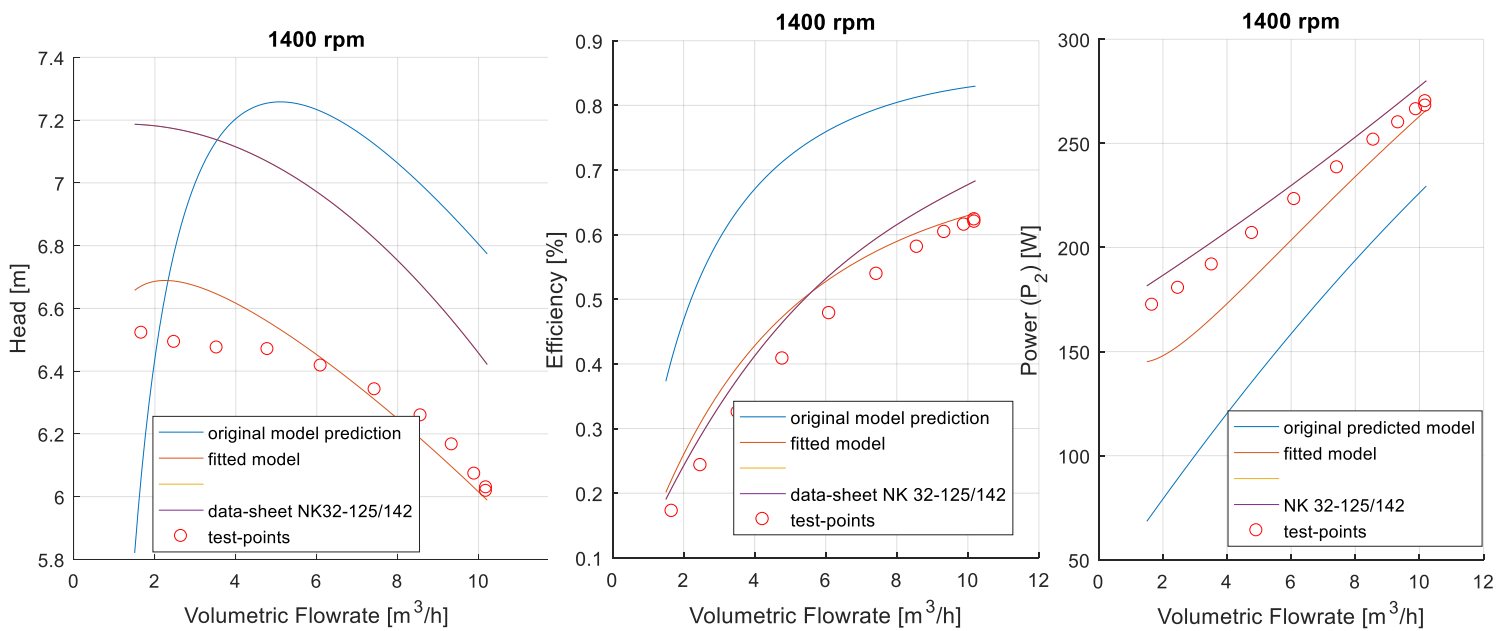
Despite this, the modeled hybrid power plant is flexible to any variations that may need to be introduced for future work. As it was already mentioned in the section 3.8, one of the limitations of this model came with the dimensioning of the lower reservoir.

Regarding the pump modelling, the performance of the mathematical model for the Grundfos impeller NK 32-125/142 is compared to the test results obtained from the same pump in the lab. Additionally, also the points from the Grundfos data-sheet are plotted for major concretion. Using the before mentioned plots, the mathematical model is fitted and validated (see Graph 9-2). This fitted model is later used for optimization purposes. The objective of the optimization has been to increase the pump head and efficiency at high flow rates bearing in mind that this optimization would also benefit a large-scale pump for hydro-storage use. The optimization results with a new impeller which in fact has higher head and efficiency at high flow rates. Lastly, the model is used to predict the pump performance of a large-scale pump. The main geometrical traits for a 1 MW pump are calculated and used in the model. For major correlation between the small impeller and the large impeller, the optimized values obtained for the small one are used in the large-scale model to evaluate their feasibility at larger scales.

The fitting is carried out by altering the head and power losses. The test-points are used as a reference for the fitting. The most significant fitting comes with the recirculation loss, for which an alternative value for the recirculation coefficient has been proposed and used in the small-scale impeller. The same occurs with the mechanical loss factor. For the friction losses, the friction coefficient for the volute is newly introduced in the fitting since in the first prediction the volute isn't considered for the impeller losses. Table 9-1 summarizes these changes.

| Name of the coefficient | Symb | Value from literature | Fitted value | Unit | Affects... |
|--------------------------------|-------------------|------------------------------|---------------------|-------------|-----------------------------|
| Recirculation coefficient | $\xi_{recir.}$ | 0.001 | 0.0001 | [-] | Recirculation losses → head |
| Friction coefficient volute | ξ_{volute} | 0 | 0.35 | [-] | Friction losses → head |
| Relative shock factor | φ_{shock} | 0.3 | 0.3 | [-] | Shock losses → head |
| Mechanical loss factor | φ_{mech} | 0.0045 | 0.3 | [-] | Mech. losses → power |

Table 9-1 Summary of fittings



Graph 9-2 Comparison between before and after the fitting with test points and data-sheet points.

Moreover, throughout the writing of the report it has been seen that different correlations for the slip had very different effects on the pump characteristics. The slip has a great effect in the theoretical head since it reduces C_{2t} , making the head get lower. The correlations that have been examined come from (Dixon, 1978) and (Gülich, 2010). The head obtained with the Gülich method has a better coherence with the test-points and has less uncertainty sources than the Dixon method. Hence, it was chosen for this report.

With all the applicable fittings, the impeller is optimized following the recommendations from (Gülich, 2010) (and other sources) to conclude an optimization with the parameters from Table 9-2. Each of the changes has a positive or negative effect on losses/phenomena. For instance, increasing the number of blades has a negative effect in the blade blockage, shock losses and leakage flow while it has a positive effect on the slip. One of the requirements that has been kept in mind during the optimization is the CFC⁵ criteria, to avoid increasing the instability of the pump curve. The final result of such optimization is plotted in Graph 9-3.

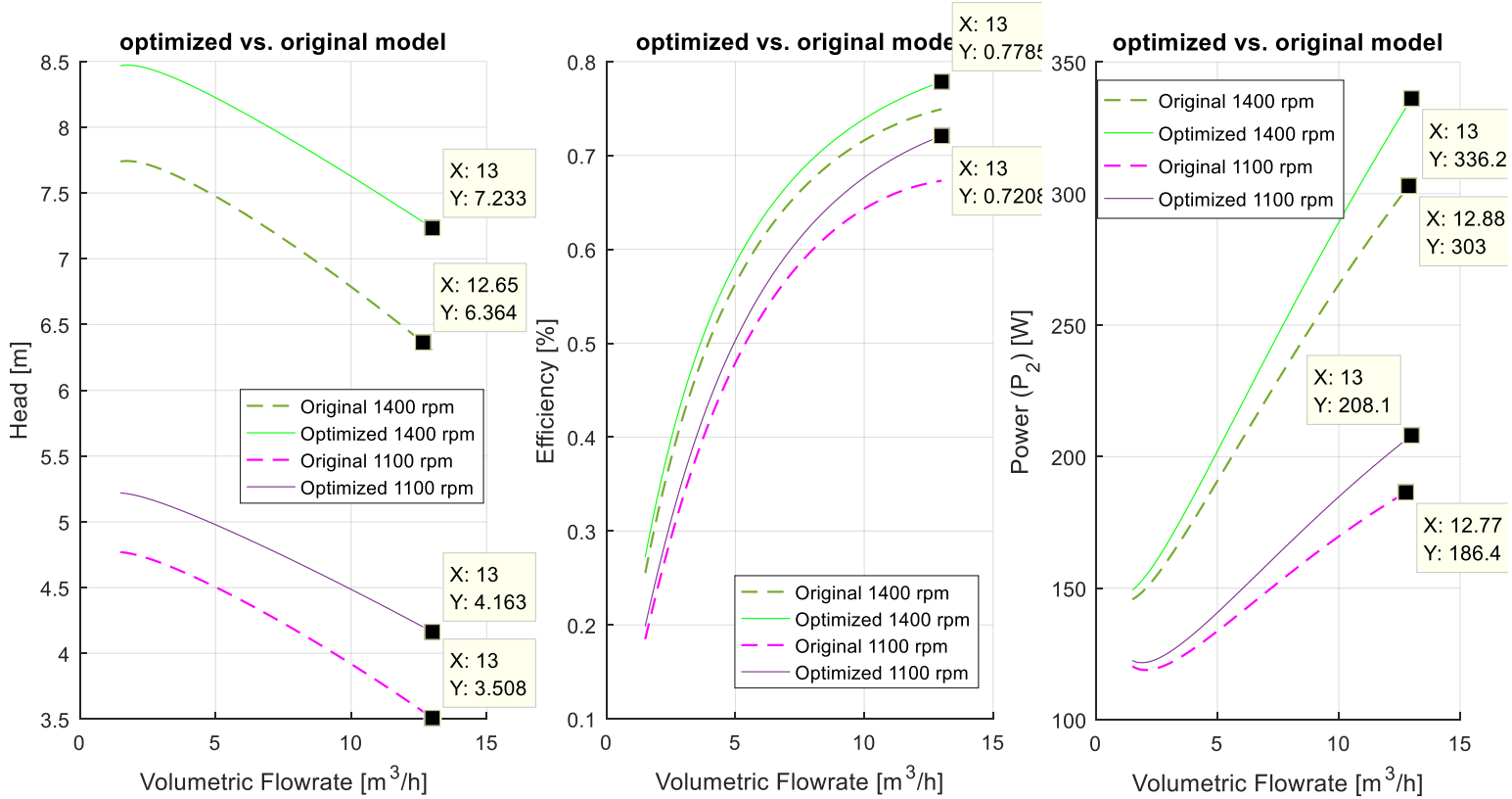
Table 9-2 Summary of the optimized parameters

| Description | Symb | Initial | Final | unit |
|-----------------------------------|-----------|---------|-------|--------|
| Outlet blade angle | β_2 | 27.28 | 30 | ° |
| Thickness of the blades at inlet | e_1 | 2.17 | 1.75 | mm |
| Thickness of the blades at outlet | e_2 | 3.47 | 2.8 | mm |
| Number of blades | Z_{La} | 5 | 9 | blades |

⁵ CFC stands for constantly falling curve



Figure 9-1 Rendering of the optimized impeller



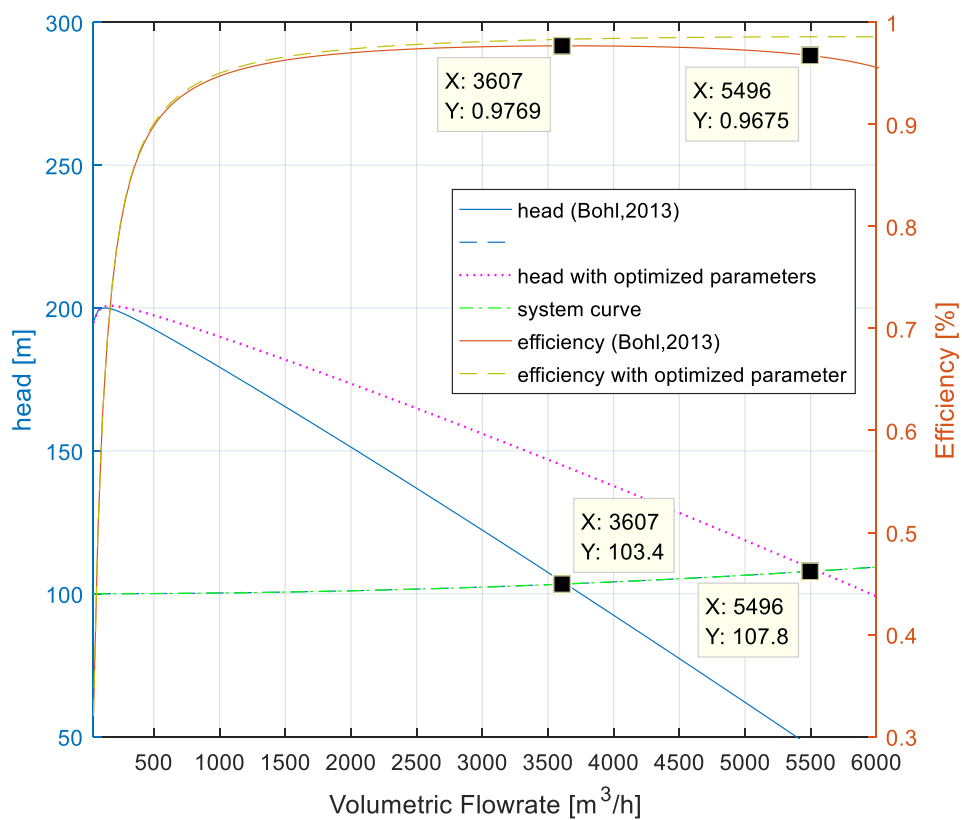
Graph 9-3 Q-H, Q- η and Q-P₂ for the original and optimized impeller at 2 different rpm

From Graph 9-3 and Table 9-3 it can be concluded that the optimization had better results at the low rotational velocity, especially regarding the efficiency.

Table 9-3 Summary of values at highest flow rate to evaluate improvement

| rpm | Characteristic | original value | optimized value | improvement |
|------|----------------|----------------|-----------------|-------------|
| 1400 | P ₂ | 304.4 | 336.2 | 10,45% |
| | H | 6.306 | 7.233 | 14,70% |
| | η | 0.7493 | 0.7785 | 3,90% |
| 1100 | P ₂ | 187.7 | 208.1 | 10,87% |
| | H | 3.508 | 4.163 | 18,67% |
| | η | 0,673 | 0,7208 | 7,10% |

Lastly, the model is used to dimension a large-scale pump for the hydro-storage of the hybrid wind-hydro power plant. Bearing in mind the power, head and flow requirements set by the hybrid plant, the most relevant geometrical parameters of the impeller are calculated and those that cannot be calculated are adapted to the big impeller using the same geometrical relations existing in the small-scale impeller. Despite that, some parameters like the size of the gap or the length of the gap between the impeller and the housing cannot be scaled since that would not be correct. In this case an approximate guess is made. For the dimensioning of the large-scale pump, the fittings used for the small-scale pump are not used since there is no reference to fit to. In this case, the original values provided by the literature are used. The optimized parameters; outlet blade angle β_2 and number of blades Z_{La} are also plotted separately to evaluate their effect in a geometrically bigger pump. The optimization meets its objective (see Graph 9-4), but large-scale pumps have other β_2 and Z_{La} requirements like smaller number of blades and more acute blade angles.



Graph 9-4 Q-H, Q-eff comparing plots obtained with the small-scale optimization and the calculated ones

Chapter 10 Future work

10.1 User interface

Designing a user interface in which by choosing the location you would get the hourly wind speed data and the hourly demand curve. Secondly, the user would choose the wind turbine model to use for the installation and the available geometrical head and surface area to use for the upper and lower reservoirs. The loss calculation would be entirely automatic including the secondary loss calculation. The dimensioning of the pump/turbine groups would be done to meet the average flow requirements as well as the head and power requirements.

From here the interface would use the information of head, volumetric flow and power to dimension the required pump for such application calculating the geometrical parameters and afterwards the present losses.

10.2 PIV tests for a better understanding of the impeller flow

Additionally, and to make the pump model more accurate, some loss models have shown to be highly dimension-dependent, requiring different values for different pump dimensions. This was the case of the recirculation loss. According to reference literature (Grundfos, 2008) and (Gulich, 2010), this loss is difficult to model and can only be quantified throughout performance measurements using advanced laser based velocity measurements.

Carrying out PIV⁶ measurements in small-scale impellers as well as larger-scale impellers would allow to assess how recirculation affects these two impellers. Beginning with this, new recirculation models could be formulated. There's a possibility that depending on the sizing of the impeller, the most suitable model would be different in each case.

10.3 Testing of the optimized impeller

The new manufactured impeller should be tested in the lab and further PIV analysis could be done to assess to which extent the optimization has influenced the losses in it.

10.4 Optimization of large-scale impellers

Furthermore, the optimization of large-scale impellers hasn't been looked into in this report thoroughly, so it would be interesting to study too.

⁶ Particle Image Velocimetry

Chapter 11 Appendix 1

11.1 Calculations for the hydro storage

If the flow chart from Figure 3-4 is followed, for the calculation of the cumulative and released volume the following equations must be used:

$$V_{absorbed} = \frac{P_{excess} \cdot 3600 \cdot 10^6 \cdot \eta_p}{(h_0 + h_f) \cdot 9810} \quad [m^3] \quad (11.1.1)$$

Where,

P_{excess} is the excess power produced by the wind turbines [MW]

η_p efficiency of the pump

h_0 initial height of the water in the reservoir [m]

h_f losses due to friction with pipes [m] calculated in Eq.(11.1.3)

$$V_{released} = \frac{P_{defect} \cdot 3600 \cdot 10^6}{(h_0 + h_f) \cdot 9810 \cdot \eta_t} \quad [m/s] \quad (11.1.2)$$

Where,

η_t is the efficiency of the turbine

Method 1: Equivalent length

For the friction losses h_f , the Darcy-Weisbach equation is used

$$h_f = f \left(\frac{L_{eq}}{D} \right) \frac{v^2}{2g} \quad [m] \quad (11.1.3)$$

Where,

L_{eq} is the length of the pipe [m] calculated as: $L_{eq} = L_{pipe} + L_{sec.losses}$ (see pg.9)

D is the diameter of the pipe [m]

v is the speed at which the flow circulates through the pipe [m/s]

g is acceleration of gravity [m/s²]

f is the friction factor [-]

In order to proceed with the calculations to find out the friction losses, the flow chart from Figure 11-1 explains the steps to be taken.

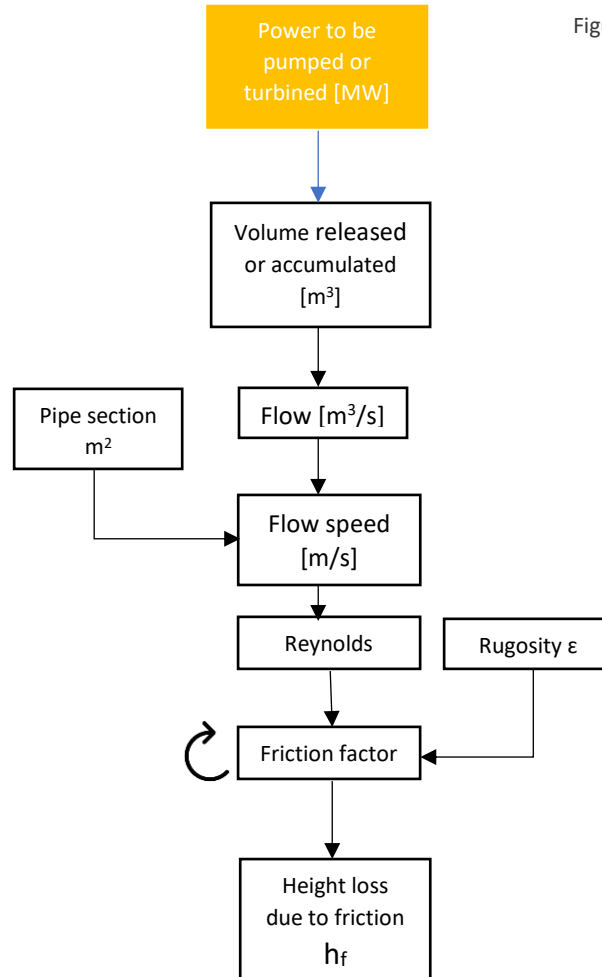


Figure 11-1 Step-by-step flowchart on how to calculate losses

For the calculation of the friction factor the Reynolds number is used both for laminar and turbulent flows

$$Re = \frac{\rho D v}{\mu} = \frac{D v}{\nu} \quad [-] \quad (11.1.4)$$

Where,

ρ is the fluid's density [kg/m³]

D is the pipe's diameter [m]

v is the fluid's speed in the pipe [m/s]

μ is the fluid's dynamic viscosity [kg/(m·s)]

ν is the fluid's kinematic viscosity [m²/s]

For laminar flows with $Re < 2000$ the following equation for the calculation of the friction factor is used

$$f = \frac{64}{Re} \quad [-] \quad (11.1.5)$$

For turbulent flow with $Re < 4000$ these iterative equation is used instead:

$$f = \frac{0.25}{\log\left(\frac{\varepsilon}{3.7D} + \frac{2.51}{Re\sqrt{f}}\right)^2} \quad [-] \quad (11.1.6)$$

Where,

ε is the rugosity of the pipe's interior [m]

D is the pipe's diameter [m]

Normally a starting value of $f = 0.0225$ is taken since it is a good starting approximation. The same equation will be repeated each time with the value of f obtained in the last calculation until the new value equals the old one. That value will be then the friction factor.

Alternatively, the Moody diagram which plots the Reynolds number and the relative rugosity can also be used.

Knowing the f , now the friction losses can be calculated for that given amount of power to be pumped/turbined. The same process was done for a range of powers from [1-16]MW and a curve was plotted examining how h_f varied depending on the power. The relation is plotted in Graph 11-1.

Method 2: loss coefficient K_L

As with Method 1, the Darcy Weisbach equation is also used with some modifications

$$h_f = \left(f \frac{L}{D} + \sum K_L\right) \frac{v^2}{2g} \quad [m] \quad (11.1.7)$$

Where,

L is the length of the pipe [m]

D is the diameter of the pipe [m]

v is the speed at which the flow circulates through the pipe [m/s]

g is acceleration of gravity [m/s²]

K_L are the representative loss coefficients proposed in (Çengel, et al., 2012) (see Table 11-1)

The rest of the calculation for the friction factor follow the same standard as for Method 1: Equivalent length.

| | K_L |
|---|--------------------------------------|
| Sudden expansion | $\left(1 - \frac{d^2}{D^2}\right)^2$ |
| Sudden contraction | Figure 11-2 |
| 45° threaded elbow | 0.4 |
| Gate valve $\frac{3}{4}$ closed | 17 |

Table 11-1 Values for loss coefficients. Source: (Çengel, et al., 2012)

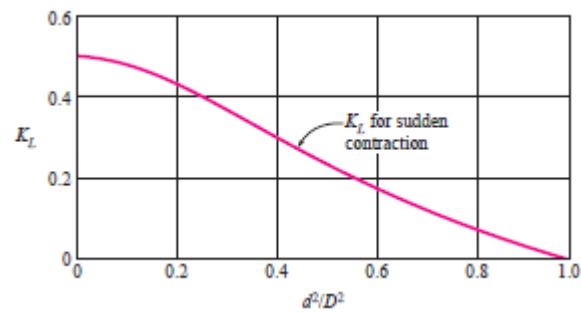
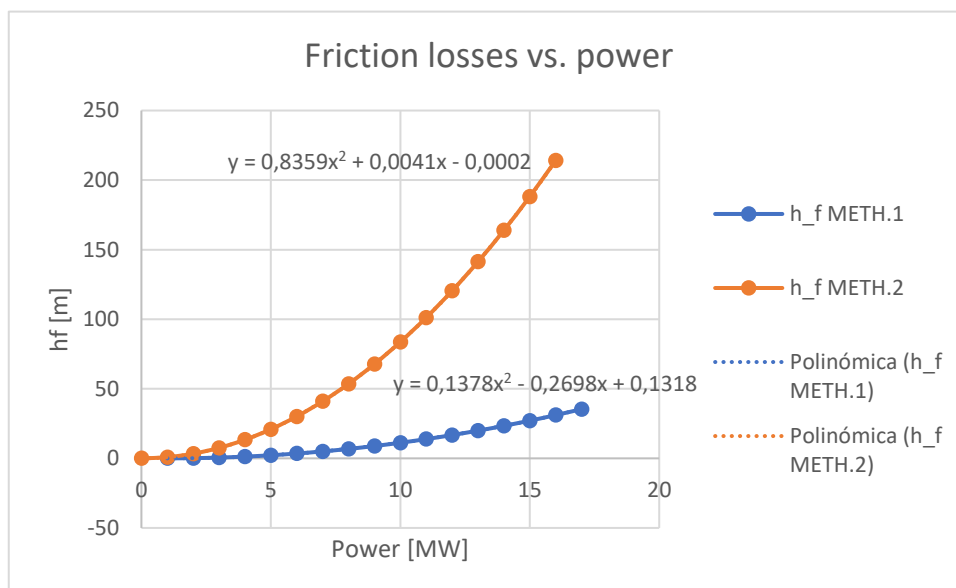


Figure 11-2 loss coefficient for sudden contraction. Source: (Çengel, et al., 2012)

How the losses vary with the power was plotted in Graph 11-1 also with Method 2. A very different plot was obtained with respect to the first method

The polynomic fit for the second method was further used to calculate all the friction losses for all the existent cases in the template.



Graph 11-1 Relation between power and friction loss for the 2 methods.

11.2 Inlet velocity triangle

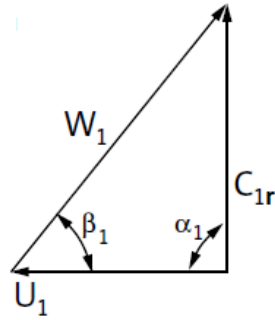


Figure 11-3 Velocity triangle inlet. Source: (Grundfos, 2008)

For a radial impeller like the one in Figure 4-2, the area will be calculated as in Eq.(11.2.1)

$$A_1 = 2\pi \cdot r_1 \cdot b_1 \quad [m^2] \quad (11.2.1)$$

Where

r_1 is the radius of the inlet edge [m]

b_1 is the blade's height in the inlet [m]

If the leakage flow is inexistent then the entire volumetric flow must go through the impeller's section ($Q_{impeller} = Q_{pump}$), therefore the radial velocity just at the entrance of the impeller corresponds to Eq.(11.2.2)

$$C_{1r} = \frac{Q_{impeller}}{A_1} \quad [m/s] \quad (11.2.2)$$

The tangential and the radial components of C_1 can be expressed respectively with Eq.(11.2.3) and Eq.(11.2.4) considering that α_1 is 90°

$$C_{1t} = \cos \alpha_1 \cdot C_1 \quad [m/s] \quad (11.2.3)$$

$$C_{1r} = \sin \alpha_1 \cdot C_1 \quad [m/s] \quad (11.2.4)$$

The blade's velocity U depends on the radius and the rotational speed of the impeller. Eq.(11.2.5)

$$U_1 = 2\pi \cdot r_1 \cdot \frac{n}{60} = r_1 \cdot \omega \quad [m/s] \quad (11.2.5)$$

Where

n is the rotational speed [rpm]

ω is the rotational velocity [rad/s]

Lastly, the relative velocity W can be described by means of Eq.(11.2.6)

$$W_1 = \sqrt{C_{1r}^2 + U_1^2} \quad [m/s] \quad (11.2.6)$$

When all the velocities have been identified, we can draw the triangle as shown in Figure 11-3 where according to α_1 is 90° it can be said that $C_{1r} = C_1$. The angle β will then correspond to Eq.(11.2.7)

$$\tan \beta_1 = \frac{C_{1r}}{U_1} \quad [-] \quad (11.2.7)$$

As was mentioned in the beginning, the value of α_1 can be 90° if there's no swirl and the inlet is entirely radial. But this doesn't always occur. Instead we could find relative flow angles above or below 90° . In this cases the inlet triangles would look like the ones in Figure 11-4 and Figure 11-5

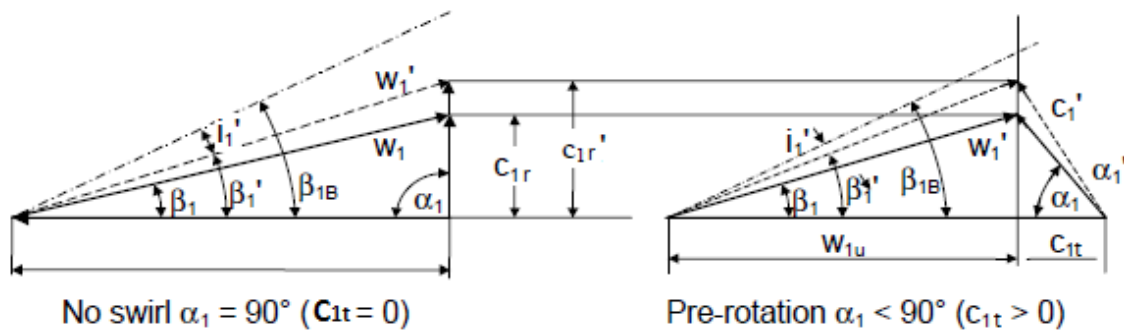


Figure 11-4 Inlet triangles with and without pre-rotation. Source: (Gülich, 2010)

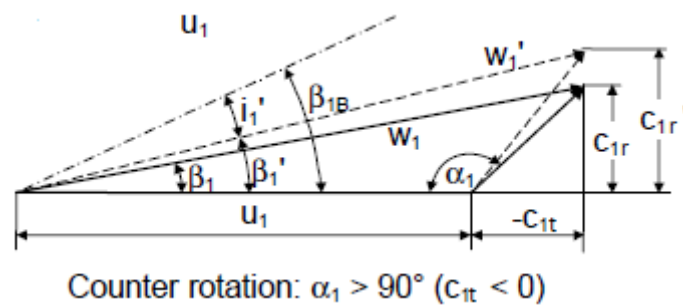


Figure 11-5 Inlet triangle for counter rotation. Source: (Gülich, 2010)

11.3 Outlet velocity triangle

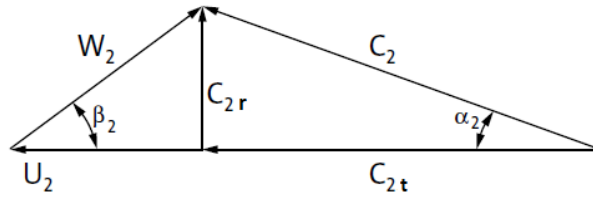


Figure 11-6 Outlet velocity triangle. Source: (Grundfos, 2008)

For a radial impeller, the outlet area can be described with Eq.(11.3.1)

$$A_2 = 2\pi \cdot r_2 \cdot b_2 \quad [m^2] \quad (11.3.1)$$

The flow's meridional velocity at the outlet can be described in the same way as for the inlet as Eq.(11.3.2) shows.

$$C_{2r} = \frac{Q_{impeller}}{A_2} \quad [m/s] \quad (11.3.2)$$

The tangential velocity U_2 is calculated with Eq.(11.3.3)

$$U_2 = 2\pi \cdot r_2 \cdot \frac{n}{60} = r_2 \cdot \omega \quad [m/s] \quad (11.3.3)$$

The value of the blade angle β at the outlet is assumed to be the same as the blade angle in the early stages of the design phase. We can know the relative velocity W_2 with Eq.(11.3.4)

$$W_2 = \frac{C_{2r}}{\sin \beta_2} \quad [m/s] \quad (11.3.4)$$

Analyzing the outlet triangle, we can deduce that the tangential component of the absolute velocity C_{2t} corresponds to Eq.(11.3.5)

$$C_{2t} = U_2 - W_{2t} = U_2 - \frac{C_{2r}}{\tan \beta_2} \quad [m/s] \quad (11.3.5)$$

11.4 Euler's pump equation

The flow enters the impeller through A_1 with an angular momentum

$$L_1 = \rho \cdot Q_{pump} \cdot r_1 \cdot C_{1t} \quad [kg \cdot m^2/s] \quad (11.4.1)$$

The flow leaves the impeller through A_2 with an angular momentum

$$L_2 = \rho \cdot Q_{pump} \cdot r_2 \cdot C_{2t} \quad [kg \cdot m^2/s] \quad (11.4.2)$$

Knowing that:

- Static pressures do not produce any forces in the tangential direction and therefore do not contribute in the momentum balance
- Radial components in the different velocities do not contribute either
- Only tangential components (C_{1t} & C_{2t}) act on the blade movement and are the only considered.

Subject to these considerations the conservation of the momentum gives an angular momentum change rate/torque as follows

$$T = \dot{m} \cdot (r_2 \cdot C_{2t} - r_1 \cdot C_{1t}) \quad [Nm] \quad (11.4.3)$$

Where,

\dot{m} is the mass flow rate through the impeller [kg/s]

Multiplying the shaft torque by the angular velocity we can find the shaft power

$$\begin{aligned} P_{shaft} &= \dot{m} \cdot \omega (r_2 \cdot C_{2t} - r_1 \cdot C_{1t}) \quad [W] \quad (11.4.4) \\ &= Q_{impeller} \cdot \rho (U_2 \cdot C_{2t} - U_1 \cdot C_{1t}) \end{aligned}$$

The specific work produced by the blades is given by dividing the shaft power (Eq.(11.4.4)) between the mass flow rate that crosses the impeller:

$$Y_{blades} = \frac{P_{shaft}}{\dot{m}} \quad [m^2/s^2] \quad (11.4.5)$$

According to the energy equation the hydraulic power applied to the fluid can be described as the increase in pressure in the impeller times the volumetric flow.

$$P_{hydr} = \Delta P \cdot Q = H \cdot \rho \cdot g \cdot Q = \dot{m} \cdot H \cdot g \quad [W] \quad (11.4.6)$$

Where

ΔP is the pressure increase in the pump [Pa]

ρ is the fluid's density [kg/m³]

g is the gravitational acceleration [m/s²]

Ideally with no losses the power absorbed by the fluid would be equal to the power delivered by the pump so that $P_{shaft} = P_{hydr}$. Considering this scenario, we obtain the Euler equation which expresses the impeller's head:

$$H_{theoric} = \frac{U_2 \cdot C_{t2} - U_1 \cdot C_{t1}}{g} = \frac{C_2^2 - C_1^2}{2g} + \frac{U_2^2 - U_1^2}{2g} + \frac{W_2^2 - W_1^2}{2g} \quad [m] \quad (11.4.7)$$

11.5 Blade blockage

The outlet of the impeller has been taken to exemplify the calculations but the same equations must be used for the inlet too.

$$C'_{2r} = C_{2r} \cdot \tau_2 \quad [m/s] \quad (11.5.1)$$

Where

C'_{2r} is the corrected radial velocity at the outlet [m/s]

τ_2 is the outlet blade blockage factor[-]

The Eq.(11.5.2) from (Gülich, 2010) shows how to calculate this factor

$$\tau_2 = 1 - \left(\frac{\pi \cdot D_2 \cdot \sin \beta_2 \cdot \sin \lambda_{LA}}{e_2 \cdot Z_{La}} \right) \quad [-] \quad (11.5.2)$$

Where

Z_{La} is the number of blades

e_2 is the thickness of the blades at outlet [m]

D_2 is the outlet diameter [m]

β_2 is the blade angle in outlet [rad]

λ_{LA} is the inclination of the blade to the impeller at outlet [rad]

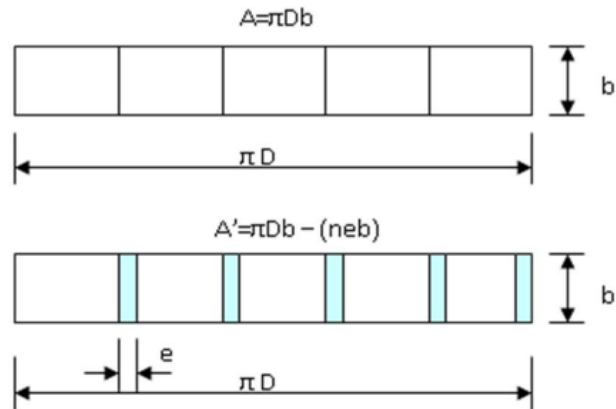


Figure 11-7 Reduction of the effective area

Finally, as it can be seen from the previous equations, blade blockage only exerts an effect on the radial component of the absolute velocity. On the other hand, the slip has an effect on the tangential component as it will be seen now.

11.6 Slip

Figure 11-8 Shows the outlet triangle with and without slip where the subscript ∞ indicates the ideal triangle. The difference between the ideal tangential absolute velocity $C_{2t\infty}$ and the real tangential absolute velocity C_{2t} is given by Eq.(11.6.1)

$$C_{2t\infty} - C_{2t} = (1 - \gamma) \cdot U_2 \quad [m/s] \quad (11.6.1)$$

Where

$C_{2t\infty}$ is the ideal tangential absolute velocity [m/s]

γ slip factor

$(1 - \gamma)$ "the slip"

Therefore, having a slip factor of $\gamma = 1$ means that the flow is totally blade-congruent and ideal. The more the γ decreases the greater the deviation becomes.

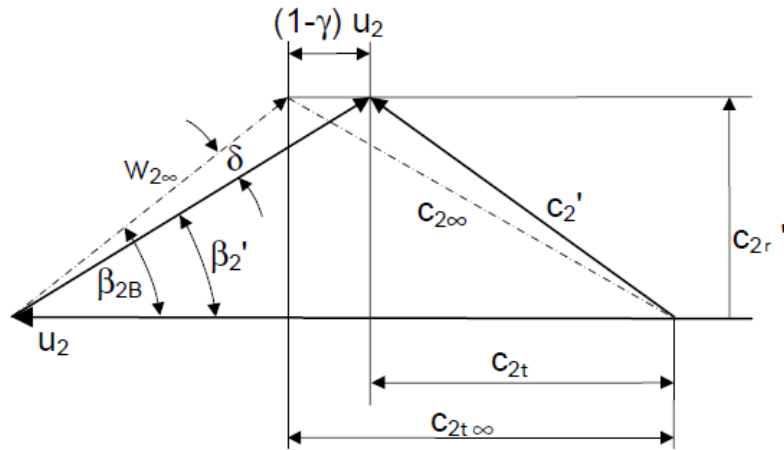


Figure 11-8 Slip and deviation angle. Source: (Gülich, 2010)

Furthermore, there's another equation (Eq.(11.6.2)) present in (Gülich, 2010) which describes accurately the slip factor for impellers with $N_{blades} \geq 3$. It reflects the results of the slip factor for radial impellers with a standard deviation of $\pm 4\%$. Since γ also appears in the calculation of the head, considerable uncertainties can be expected in the performance prediction.

$$\gamma = f_1 \cdot \left(1 - \frac{\sqrt{\sin \beta_{2B}}}{Z_{La}^{0.7}} \right) \cdot k_w \quad [-] \quad (11.6.2)$$

Where,

$f_1 = 0.98$ for radial impellers and $f_1 = 1.02 + 1.2 \cdot 10^{-3} \cdot (n_q - 50)$ for semi-axial impellers

Z_{La} is the number of blades

k_w coefficient indicating the influence of the inlet diameter on the slip factor. Calculated in Eq.(11.6.5).

β_{2B} is the ideal relative outlet angle

$$d_{1m}^* = \frac{\sqrt{0.5(d_1^2 + d_{1i}^2)}}{d_2} \quad [-] \quad (11.6.3)$$

Where,

d_1 is the inside diameter of the top part of the blade [m]

d_{1i} is the inside diameter of the bottom part of the blade [m]

d_2 is the outer diameter [m]

$$\varepsilon_{Lim} = e^{\left(\frac{-8.16 \cdot \sin \beta_{2B}}{Z_{La}}\right)} \quad [-] \quad (11.6.4)$$

If $d_{1m}^* < \varepsilon_{Lim}$ then the following parameter $k_w = 1$. Otherwise it must be calculated with the following equation:

$$k_w = 1 - \left(\frac{d_{1m}^* - \varepsilon_{Lim}}{1 - \varepsilon_{Lim}}\right)^3 \quad [-] \quad (11.6.5)$$

Where,

d_{1m}^* is a dimensionless number from Eq.(11.6.3)

ε_{Lim} is given by Eq.(11.6.4)

Alternatively, the Busemann slip factor (Dixon, 1978) proposes another method to calculate the slip. which can be written as Eq.(11.6.6). This method is going to be used further in the model.

$$\gamma_B = \frac{A - B \cdot \varphi_2 \cdot \tan \beta'_2}{1 - \varphi_2 \cdot \tan \beta'_2} \quad [-] \quad (11.6.6)$$

Where,

A & B are functions of r_2/r_1 , β'_2 and the number of blades Z_{La}

φ_2 coefficient calculated in Eq. (11.6.7)

$$\varphi_2 = \frac{C_{r2}}{U_2} \quad [-] \quad (11.6.7)$$

For pumps in which the coefficient l/s Eq.(11.6.8) & Eq.(11.6.9) exceeds the unity the dependence of A & B on r_2/r_1 is negligible

$$s = 2\pi \cdot \frac{(r_2 - r_1)}{Z_{La} \cdot \ln(r_2 - r_1)} \quad [-] \quad (11.6.8)$$

$$l = \frac{Z_{La}}{2\pi \cdot \cos \beta_2} \cdot \ln\left(\frac{r_2}{r_1}\right) \cdot s \quad [-] \quad (11.6.9)$$

If $\frac{l}{s} \geq 1$ then Eq.(11.6.6) can be applied. The value of A can be found in the Csanady graph (Dixon, 1978) shown in Figure 11-9.

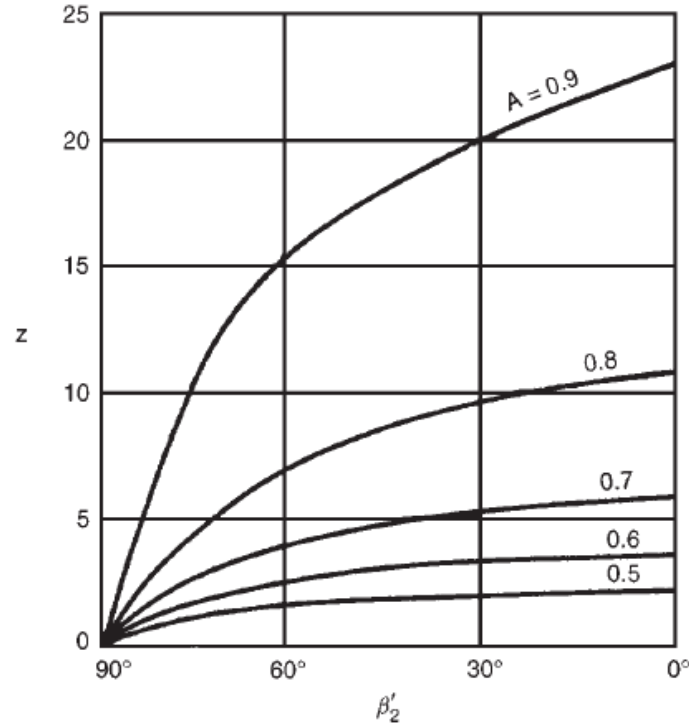


Figure 11-9 Csanady graph for head correction factors

The graph from Figure 11-9 is in general valid for blade outlet angles between $50 \leq \beta_2 \leq 70$ with 5 to 12 blades. As long as these criteria are followed the value of B remains constant and equal to 1 under all the conditions. The A values may also be interpreted as the value for γ_B when there's no flow through the impeller.

Knowing the slip factor γ_B we can now calculate the corrected absolute radial velocity at the outlet.

$$C_{2tcorrected} = \gamma_B \cdot U_2 \cdot (1 - (\varphi_2 \cdot \tan \beta_2)) \quad [m/s] \quad (11.6.10)$$

The corrected C_{2t} must be used for further head calculations instead of the first C_{2t} that was calculated.

11.7 Mechanical losses

The mechanical losses follow Eq.(11.7.1) (Gülich, 2010)

$$P_{mech} = 0.0045 \cdot \left(\frac{Q_{ref}}{Q}\right)^{0.4} \cdot \left(\frac{n_{ref}}{n}\right)^{0.3} \cdot P_{opt} \quad [W] \quad (11.7.1)$$

Where,

Q_{ref} is the reference volumetric flow which equals 1 m³/s

Q is the volumetric flow through the impeller [m³/s]

n_{ref} is the reference rotational speed which equals 1500 rpm

n is the impeller's rotational speed

P_{opt} is the shaft's power at the BEP [W]

Our motor has a P_{opt} of 370 W The mechanical efficiency of a given pump decreases with the speed

11.8 Hydraulic losses

They contemplate losses in the inlet, the impeller, the volute, the diffuser and the outlet. Hydraulic losses are generated by friction and the creation of vortices:

1. Surface friction losses occur as a result of shear stresses in the boundary layers of the pump structures. If the flow is accelerating the roughness and the Reynolds number will have a significant impact, on the other hand with decelerating flows they will have less impact.
2. Instead decelerating flow creates thick boundary layers which makes the flow profile less uniform. This gives places to more turbulences which ends up in a slight increase in the temperature of the fluid

The hydraulic efficiency that we obtain from the power balance doesn't provide any relevant information about the individual loss in the pump's components. These losses have to be estimated individually by means of empirical calculations since they cannot be described uniquely with simple models.

Friction losses

The loss model for impellers considers the following steps (Gülich, 2010):

1. Definition of the average relative velocity at the impeller's channels Eq.(11.8.1) formed by the throat areas a_1 and a_2 (Figure B-11-10)

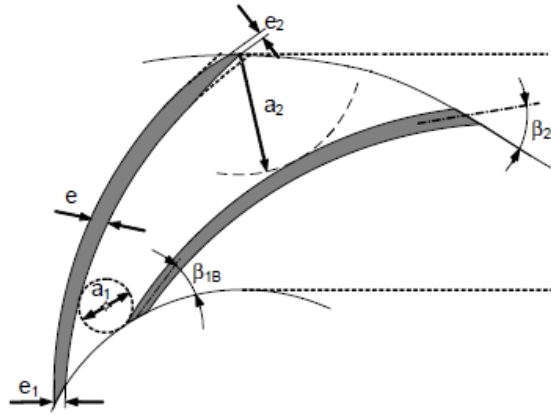


Figure B-11-10 Distance between vanes at inlet and outlet. Source: (Gülich, 2010)

$$w_{av} = \frac{2 Q_{impeller}}{Z_{La} (a_2 b_2 + a_1 b_1)} \quad [m/s] \quad (11.8.1)$$

Where,

Z_{La} is the number of blades

a_2/a_1 is the distance between the vanes at the outlet/inlet [m]

b_2/b_1 is the height of the blade at the outlet/inlet [m]

2. Definition of the friction coefficient is a function of the Reynolds number and the roughness

$$Re = \frac{w_{av} L_{sch}}{\nu} \quad [-] \quad (11.8.2)$$

Where,

w_{av} average relative velocity at the impeller's channels in Eq. (11.8.1)

L_{sch} is the length of the impeller channel [m]

$$C_d = \frac{0.136}{\left[-\log\left(0.2 \frac{\varepsilon}{L_{sch}} + \frac{12.5}{Re}\right)\right]^{2.15}} \quad [-] \quad (11.8.3)$$

Where,

ε is the roughness of the surface

L_{sch} is the length of the impeller channel [m]

Re is the Reynolds number calculated in Eq.(11.8.2)

3. Definition of the hydraulic diameter

$$D_h = \frac{2(a_2b_2 + a_1b_1)}{a_1 + b_1 + a_2 + b_2} \quad [-] \quad (11.8.4)$$

Where,

a_2/a_1 is the distance between the vanes at the outlet/inlet [m]

b_2/b_1 is the height of the blade at the outlet/inlet [m]

4. Definition of the loss coefficient for the impeller including the friction, the deceleration and the effect of turbulence

$$\xi_{friction} = 4 \cdot C_d \cdot \frac{L_{sch}}{D_h} \cdot \left(\frac{w_{av}}{U_2}\right)^2 \quad [-] \quad (11.8.5)$$

Where all the variables have been described in Eq.(11.8.1)(11.8.2)(11.8.3)(11.8.4)

5. Lastly, the loss coefficient will be included in the following equation which gives us the head loss. According to (Grundfos, 2008), when the flow friction is calculated in the impeller, the relative velocity must be used in the equation.

$$H_{fric_{impeller}} = \xi_{friction} \cdot \frac{W_2^2}{2g} \quad [m] \quad (11.8.6)$$

Where,

$\xi_{friction}$ is the coefficient for these losses [-]

U_2 is the outlet blade velocity [m/s]

g is the gravity acceleration [m/s²]

Friction losses in the volute

These losses were taken into account to adapt the head of the model to the head obtained from the test setup. Losses in the volute cannot be neglected. Nevertheless, all the models used to calculate these losses are highly complex, therefore this loss will be treated as a hydraulic loss containing a loss coefficient ξ_{volute} which will be varied until the modeled curve fits the head curve obtained from the testing.

$$H_{fric_{volute}} = \xi_{volute} \cdot \frac{(\sqrt{C_{2r}^2 + C_{2t}^2})^2}{2g} \quad [m] \quad (11.8.7)$$

Where,

ξ_{volute} coefficient for these losses in the volute (values ranging from [0.08-0.18]) [-]

U_2 is the outlet blade velocity [m/s]

g is the gravity acceleration [m/s²]

To sum up the total friction losses between the impeller and the volute will look like:

$$H_{fiction} = H_{fric_{volute}} + H_{fric_{impeller}} \quad [m] \quad (11.8.8)$$

Where,

$H_{fric_{volute}}$ is calculated in Eq.(11.8.7) [m]

$H_{fric_{impeller}}$ is calculated in Eq.(11.8.6) [m]

Shock losses

This loss coefficient ξ_{shock} uses the following steps from (Gülich, 2010) to be calculated:

1. We calculate the radial component of the relative velocity at the inlet

$$W_{1r} = \sqrt{C_{1r}^2 + (U_1 - C_{1t})^2} \quad [m/s] \quad (11.8.9)$$

Where,

C_{1r} is the radial component of the absolute [m/s]

U_1 is the blade velocity at the inlet [m/s]

C_{1t} is the tangential component of the absolute velocity [m/s]

2. We calculate the velocity in the impeller's throat

$$W_{1throat} = \frac{Q_{impeller}}{Z_{La} a_1 b_1} \quad [m/s] \quad (11.8.10)$$

3. Thirdly, we can calculate the loss coefficient

$$\xi_{shock} = 0.3 \left(\frac{W_{1r} - W_{1throat}}{U_2} \right)^2 \quad [-] \quad (11.8.11)$$

4. Lastly, the height losses can be calculated according to the shock loss equation provided by (Grundfos, 2008)

$$H_{shock} = \xi_{shock} \cdot \frac{|W_1 - W_{1throat}|^2}{2g} \quad [m] \quad (11.8.12)$$

Recirculation losses

There are no simple or generic models that quantify recirculation, it is normally identified through performance measurements showing lower heads or higher power consumptions when the pump is operating at $Q_{impeller} \neq Q_{BEP}$. Though, one way to calculate the power loss due to recirculation is suggested by (Tuzson, 2000) only valid when $Q_{impeller} < Q_{BEP}$

$$P_{recir.} = \xi_{recir.} \cdot \omega^3 \cdot d_1^2 \cdot \left(1 - \frac{Q_{impeller}}{Q_{BEP}} \right)^{2.5} \quad [W] \quad (11.8.13)$$

Where,

$\xi_{recir.}$ Has a value between 0.0001 and 0.0007 according to literature (Tuzson, 2000)

ω is the rotational velocity [rad/s]

d_1 is the inlet diameter [m]

$Q_{impeller}$ flow rate through the impeller [m³/s]

Q_{BEP} flow rate at the best efficiency point [m³/s]

And the head is then calculated as

$$H_{recirc.} = \frac{P_{recir.}}{Q_{impeller} \cdot \rho \cdot g} \quad [m] \quad (11.8.14)$$

The chosen value for $\xi_{recir.}$ has a considerable effect on this calculation. Throughout the report this parameter will be set at a value of 0.001 which gives the most reasonable Q-H and Q-P diagrams.

Expansion and contraction losses

According to literature (Çengel, et al., 2012) the height loss due to this components when having turbulent flow follow both the same principle

$$H_{loss} = \xi_{loss} \cdot \frac{V^2}{2g} \quad [m] \quad (11.8.15)$$

Where,

ξ_{loss} is the loss coefficient depending on whether it's an expansion or a contraction

V is the highest velocity in the component

For the case of the contraction, it must be assumed that manufacturers always round up all edges to avoid unnecessary losses. Therefore the contraction is assumed to be a smooth one. Literature suggests different values for ξ_{loss} depending on the degree of gradual contraction of the pipe (Figure 11-11). For the inlet in the impeller the angle of opening is $\theta \geq 60^\circ$, according to (Çengel, et al., 2012) a value of $\xi_{loss} = 0.07$ corresponds to this opening.

$$H_{contract} = \xi_{contract} \cdot \frac{C_{1r}^2}{2g} \quad [m] \quad (11.8.16)$$

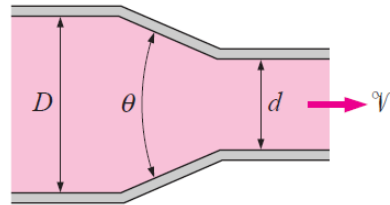


Figure 11-11 gradual contraction. Source: (Çengel, et al., 2012)

For the case of the expansion, most of the expansions occurring in the impeller and the housing are sudden. Therefore the implemented equation has been:

$$H_{exp} = \xi_{exp} \cdot \frac{C_{2r}^2}{2g} \quad [m] \quad (11.8.17)$$

Where,

$$\xi_{exp} = \alpha \left(1 - \frac{b_2^2}{b_3^2} \right)^2 \quad [-] \quad (11.8.18)$$

Where,

α is the kinetic energy correction factor which is 2 for laminar flow and 1.05 for turbulent flow.[-]

b_2 is the blade height at the outlet [m]

b_3 is the diameter of the volute [m]

Disk friction losses

The value of the disk friction depends on the impeller diameter and the dimensions of the casing, particularly the distance between the casing and the impeller Figure B-11-12.

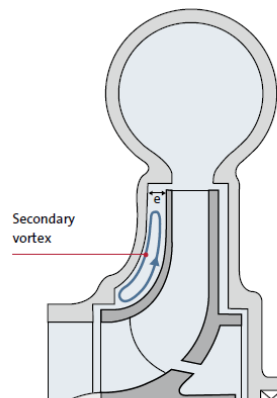


Figure B-11-12 Separation between pump casing and impeller. Source: (Grundfos, 2008)

The fluid that flows through the space left between the casing and the impeller rotates creating a primary vortex. The rotational velocity equals the impellers rotational velocity at its surface while it is 0 on the surface of the pump's casing. Therefore, the rotational velocity of this vortex is considered to be half of the total rotational velocity.

The centrifugal force creates a secondary vortex due to the difference in the rotational speeds between the above mentioned surfaces. This vortex increases the disk friction since it originates an energy transfer from the impeller's surface to the inner surface of the casing.

The value of the disk friction depends on the dimensions of the impeller and the housing as well as the surface roughness. It can be divided in 2 different contributions; plate-friction and cylinder-friction. It is divided into 3 plate frictions and 2 cylinder frictions.

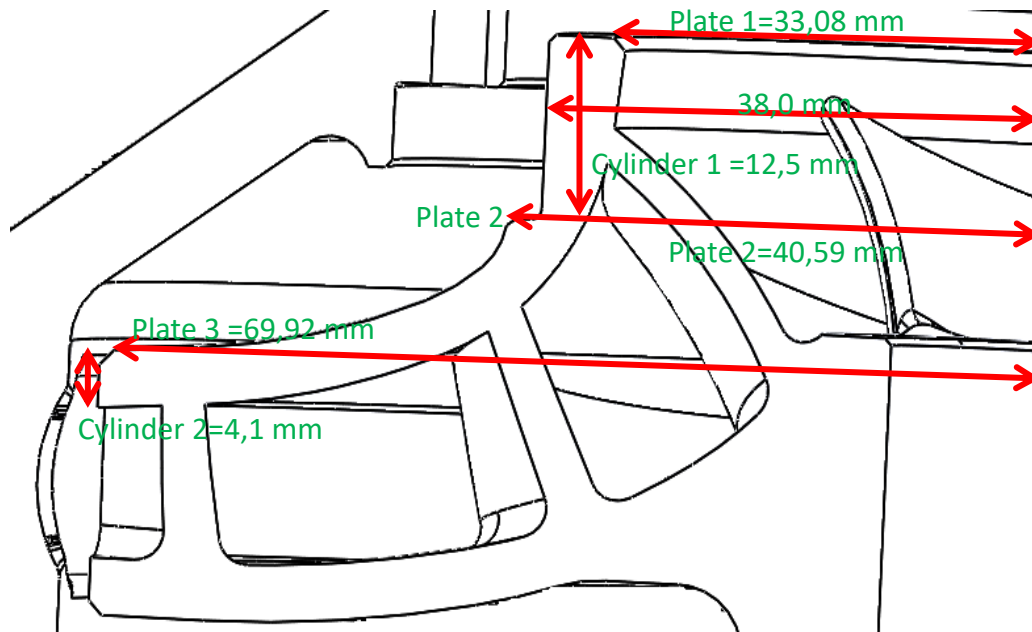


Figure 11-13 Measures taken from the ilet eye of the impeller

The

equations used depend on whether we speak about the plate of the cylinder and whether it is a turbulent or laminar flow. The equations are from (Gülich, 2010).

The flow friction factor C_f depends on the Reynolds number, the length of the disk and the roughness of the surface. If the Reynolds Eq.(11.8.19) is in this range $10^5 < Re < 10^8$ and the relative roughness is in this range $0 < \frac{\varepsilon}{L_{disk}} < 10^{-3}$ then the flow is turbulent.

$$Re = \frac{\bar{\omega} \cdot L_{disk}}{\nu} \quad [m^2] \quad (11.8.19)$$

Where,

$\bar{\omega}$ is the tangential velocity of the impeller. $\bar{\omega}_{plate} = \omega(r_{innerplate} + \frac{2}{3}r_{outerplate})$ and $\bar{\omega}_{cylinder} = \omega \cdot r_{cylinder}$

L_{disk} is the circumference of the impeller. $L_{disk_{plate}} = (r_{innerplate} + \frac{2}{3} \cdot r_{outerplate}) \cdot 2\pi$ and $L_{disk_{cylinder}} = r_{cylinder} \cdot 2\pi$

ν is the kinematic viscosity [m^2/s]

Once we have the Reynolds number we can calculate the friction coefficient for a turbulent flow

$$C_{f,turbulent} = \frac{0.136}{\left[-\log_{10}\left(0.2 \cdot \frac{\varepsilon}{L_{disk}} + \frac{12.5}{Re}\right)\right]^{2.15}} \quad [-] \quad (11.8.20)$$

Where,

Re is the Reynolds number calculated in Eq.(11.8.19)

If the flow is instead laminar ($0.01 < Re < 10^5$) the friction coefficient will be:

$$C_{f,laminar} = \frac{2.65}{Re^{0.875}} - \frac{2}{8 \cdot Re + \frac{0.016}{Re}} + \frac{1.328}{\sqrt{Re}} \quad [-] \quad (11.8.21)$$

Once we have the coefficient we go ahead and calculate the power loss for the plate and for the cylinder. It must be known that we have considered 3 plates and 2 cylinders, and therefore the previous calculations must be repeated twice considering plate 1 & plate 2 and additionally plate 2 & plate 3. With the cylinders we just have to repeat the calculations for each cylinder. We will have two friction coefficients for the plates and two friction coefficients for the cylinders, which now must be used in Eq. (11.8.22) and Eq.(11.8.23)

$$P_{plate,loss} = \frac{\pi}{5} \rho C_f \omega^3 (r_{outerplate}^5 - r_{innerplate}^5) \quad [W] \quad (11.8.22)$$

Where,

ρ is the density of the fluid [kg/m³]

C_f is the friction coefficient [-]

ω is the rotational speed [rad/s]

$r_{outerplate}$ is the outer radius of the plate [m]

$r_{innerplate}$ is the inner radius of the plate [m]

For the rotating cylinder the power consumption will be:

$$P_{cylinder,loss} = \pi \rho C_f \omega^3 r_{cylinder}^4 h_{cylinder} \quad [W] \quad (11.8.23)$$

Where,

$r_{cylinder}$ is the radius of the cylinder [m]

$h_{cylinder}$ is the height of the cylinder [m]

Lastly, the addition of the before calculated power losses gives the total disk loss power

$$P_{disk,loss} = P_{cylinder,loss} + P_{plate,loss} \quad [W] \quad (11.8.24)$$

Leakage flow

Leakage occurs when there's a back flow through the existing gaps between the impeller and the housing. This results in losses due to the flow in the impeller being greater than the one through the pump. This happens due to pressure differences inside the impeller. This problem can be minimized (but not avoided) by fitting the impeller as close to the housing as possible. What needs to be determined from the following equations is the $Q_{leakage}$.

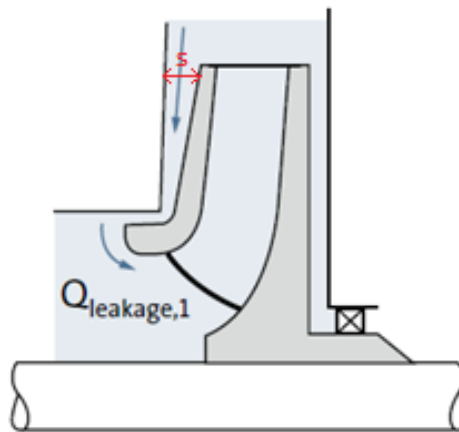


Figure B-11-14 Illustration of where does the leakage flow occurs. Source: (Grundfos, 2008)

The pressure drop across the seal is determined by Eq.(11.8.25)

$$H_p = \frac{U_2^2 - U_1^2 + W_1^2 - W_2^2}{2g} - H_{losses} \quad [m] \quad (11.8.25)$$

Where,

U corresponds to the blade velocity in inlet/outlet [m/s]

W corresponds to the relative velocity in inlet/outlet [m/s]

H_{losses} corresponds to the height losses in the impeller (Shock losses, contraction & expansion losses, friction losses, recirculation losses)

Secondly the Reynolds number is calculated with radial and circumferential speeds, determined as the averages between inlet and outlet.

$$Re_{U_2} = \frac{U_2 \cdot r_2}{\nu} \quad [-] \quad (11.8.26)$$

Where,

U_2 is the blade velocity at the outlet [m/s]

r_2 is the radius at the outlet [m]

ν is the kinematic viscosity [m²/s]

The rotation factor for radially inward flow k is determined as

$$k = 0.9 \cdot y_{sp}^{0.087} \quad [-] \quad (11.8.27)$$

Where,

y_{sp} is the coefficient expressed in Eq.(11.8.28) [-]

$$y_{sp} = Re_{U_2}^{0.3} \frac{s \cdot d_{sp}}{d_2^2} \sqrt{\frac{s}{L_{sp}}} \quad [-] \quad (11.8.28)$$

Where,

Re_{U_2} is the Reynolds number calculated in Eq.(11.8.26)

s is the width of the gap through where the leakage flow goes [m]

d_{sp} is the radial distance to the gap [m]

d_2 is the diameter at the outlet [m]

L_{sp} is the length of the gap [m]

Now the pressure difference across the seal when the leakage flows radially inwards is calculated

$$\Delta H_{sp} = H_p - k^2 \frac{U_2^2}{2g} \left(1 - \frac{d_{sp}^2}{d_2^2} \right) \quad [m] \quad (11.8.29)$$

Where,

H_p is the static pressure rise created by the impeller calculated in Eq.(11.8.25)

k coefficient calculated in Eq.(11.8.27)

The axial velocity of the fluid inside the gap for “i” number of chambers is determined as

$$c_{ax} = \sqrt{\frac{2g \cdot \Delta H_{sp}}{\zeta_{EA} + \lambda \cdot \frac{L_{sp}}{2S} + \sum_{i=1}^i \left(\frac{d_{sp}}{d_{si}}\right)^2 \cdot \left(\frac{S}{s_i}\right)^2 \cdot \left[\zeta_K + \lambda_i \cdot \frac{L_i}{2s_i}\right]}} \quad [m/s] \quad (11.8.30)$$

Where,

ΔH_{sp} corresponds to the pressure difference across the seal as shown in Eq. (11.8.29)

ζ_{EA} loss coefficient in inlet and outlet. Range of values from [1,1.2]

ζ_K loss coefficient per chamber. Range of values from [1,1.3]

d_{si} the radial distance to the gap i [m]

s_i is the width of the gap i [m]

λ_i is the friction coefficient for the gap i [-]

L_i is the length of the gap i [m]

The calculation of the value of the friction coefficient depends on two different Reynolds numbers calculated in Eq. (11.8.31).

$$Re = \frac{2 \cdot s \cdot c_{ax}}{\nu} \quad [-] \quad (11.8.31)$$

$$Re_u = \frac{2 \cdot s \cdot u_{sp}}{\nu} \quad [-] \quad (11.8.32)$$

Where,

u_{sp} is the velocity given by Eq. (11.8.33)

$$u_{sp} = \frac{\pi \cdot d_{sp} \cdot n}{60} \quad [m/s] \quad (11.8.33)$$

From here, for $Re > 2000$ the friction coefficient λ can be calculated as:

$$\lambda = \left[1 + 0.19 \left(\frac{Re_u}{Re}\right)^2\right]^{0.375} \cdot \lambda_0 \quad [-] \quad (11.8.34)$$

Where,

λ_0 is the friction coefficient when $u_{sp} = 0$ calculated in Eq.(11.8.35)

$$\lambda_0 = \frac{0.31}{\left[\log\left(A + \frac{6.5}{Re}\right)\right]^2} \quad [-] \quad (11.8.35)$$

Where,

A corresponds to the seal surface which differs depending on how the surface is. For rough surfaces $A = 0.135 \cdot \frac{\varepsilon}{s}$

On the other hand, for $Re < 2000$ the friction coefficient equals

$$\lambda = 1 + 0.2 \left(\frac{Re_u}{2000}\right)^{1.03} \cdot \lambda_0 \quad [-] \quad (11.8.36)$$

Where,

λ_0 is the friction coefficient when $u_{sp} = 0$ calculated in Eq.(11.8.37)

$$\lambda_0 = \frac{96}{Re} \cdot \left(1 - 0.6 \frac{e_x}{s}\right) \quad [-] \quad (11.8.37)$$

Where,

e_x this term called eccentricity. According to (Gülich, 2010) this term can be neglected with turbulent flow. With laminar flow the seal resistance decreases with increasing eccentricity.

Finally, the leakage flow can be calculated as:

$$Q_{leakage} = \pi d_{sp} s c_{ax} \quad [m^3/h] \quad (11.8.38)$$

Where,

d_{sp} is the radial distance to the gap [m]

s is the width of the gap through where the leakage flow goes [m]

c_{ax} is the average axial velocity in the gap. Calculated in Eq.(11.8.30)

Once we know the leakage flow through the gaps we can calculate the flow through the impeller as

$$Q_{impeller} = Q_{pump} + Q_{leakage} \quad [m^3/s] \quad (11.8.39)$$

11.9 Calculation of geometrical dimensions

For the calculation of the more meaningful geometrical dimensions of an impeller, some previous baseline data must be known such as the volumetric flow through the impeller, the achievable head and the rotational speed.

The most meaningful geometrical dimensions of a pump, which will allow to make a proper estimation of the rest of parameters are:

- Outer diameter d_2
- Inlet and outlet height of the impeller b_1/b_2
- Inlet and outlet blade angles β_1/β_2
- Number of blades Z_{La}

Outlet diameter d_2

The first step will be to calculate the specific rotational speed

$$n_q = n \cdot \frac{\sqrt{Q}}{H^{\frac{3}{4}}} \quad [rad/s] \quad (11.9.1)$$

Where,

n is the rotational speed [rad/s]

Q is the volumetric flow rate through the impeller [m³/s]

H is the pump's head [m]

The exterior diameter d'_2 depends on the factor ψ

$$d'_2 = 0.45 \cdot \frac{1}{n} \cdot \sqrt{\frac{Y}{[\psi_0; \psi_1]}} \quad [m] \quad (11.9.2)$$

Where,

n is the rotational speed in [s⁻¹] → $n/60$

Y is the parameter which is calculated as $Y = g \cdot H$ [J/kg]

$\psi_0; \psi_1$ is a parameter which initial value comes from Figure 11-15. This value has a minimum and a maximum for a given rotational speeds. Both will be considered, obtaining two different results.

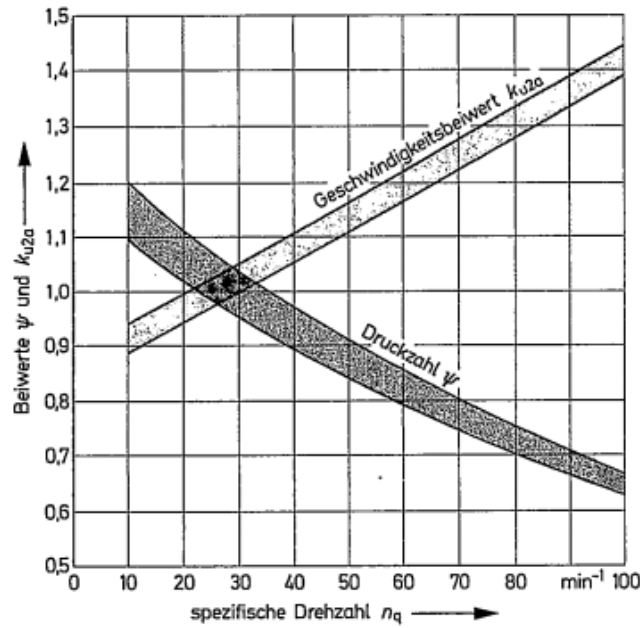


Figure 11-15 Relation between ψ , K_{u2a} and specific rotational speed. Source: (Bohl, 2013)

The ψ parameter can be calculated with the following equation:

$$\psi \approx \frac{2}{n_q^5} \quad [-] \quad (11.9.3)$$

Where,

n_q is the specific rotational speed calculated in Eq.(11.9.1)

A control calculation via the coefficient k_{u2a} gives the following range of values for d'_2

$$u_{2a} = [k_{u2a,0}; k_{u2a,1}] \sqrt{2 \cdot Y} \quad [m/s] \quad (11.9.4)$$

Where,

$[k_{u2a,0}; k_{u2a,1}]$ is a coefficient with a range of values according to Figure 11-15.

Y is the parameter which is calculated as $Y = g \cdot H$ [J/kg]

The range of values for u_{2a} is now used to calculate the control d'_2 :

$$d'_2 = \frac{u_{2a}}{\pi \cdot n} \quad [m] \quad (11.9.5)$$

Where,

u_{2a} is the circumferential speed at the outer diameter d'_2 [m/s]

n is the rotational speed in $[s^{-1}] \rightarrow n/60$

An empirical formula gives the following value for d'_2

$$d'_2 = \frac{0.45 \cdot n_q + [K_0; K_1]}{n} \cdot \sqrt{H} \quad [m] \quad (11.9.6)$$

Where,

n_q is the specific rotational speed calculated in Eq.(11.9.1)

$[K_0; K_1]$ coefficient which according to (Bohl, 2013) ranges from [71-75]

H is the required head [m]

n is the rotational speed [rpm]

Under the effect of the coefficient δ , another measurement for d'_2 is obtained

$$\delta \approx \frac{138.5}{n_q^{0.96}} \quad [-] \quad (11.9.7)$$

And finally, the last d'_2 is calculated:

$$d'_2 = \delta \cdot \frac{\sqrt{Q}}{(2 \cdot Y)^{\frac{1}{4}} \sqrt{\pi}} \cdot 2 \quad [m] \quad (11.9.8)$$

Where,

Q is the flow through the impeller [m^3/s]

δ is the coefficient calculated in Eq.(11.9.7)

Y is the parameter which is calculated as $Y = g \cdot H$ [J/kg]

All of these previous values for d'_2 must be taken into account to calculate an average value.

Height of the impeller b_1/b_2

This two values depend on the meridional speeds of the flow C_{2m} and C_{1m} that are calculated as

$$C_{2m} = k_{m2} \cdot \sqrt{2Y} \quad [m/s] \quad (11.9.9)$$

$$C_{1m} = k_{m1} \cdot \sqrt{2Y} \quad [m/s] \quad (11.9.10)$$

Where,

k_{m2}/k_{m1} are values that depend directly on the specific rotational speed n_q . (Bohl, 2013) provides

Y is the parameter which is calculated as $Y = g \cdot H$ [J/kg]

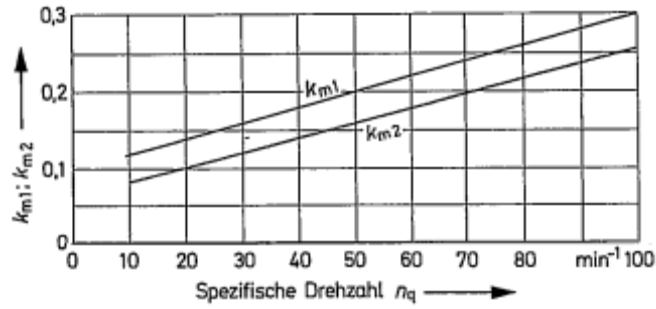


Figure 11-16 Values for k_{m1} and k_{m2} . Source: (Bohl, 2013)

In the next step, the scaled blade height can be determined as

$$b'_2 = \frac{Q}{d_{2m} \cdot \pi \cdot C_{2m}} \cdot k_2 \quad [m] \quad (11.9.11)$$

$$b'_1 = \frac{Q}{d_{1m} \cdot \pi \cdot C_{1m}} \cdot k_1 \quad [m] \quad (11.9.12)$$

Where,

b'_2/b'_1 are the scaled outlet and inlet blade heights [m]

C_{2m}/C_{1m} are the meridional speeds of the flow. Calculated in Eq.(11.9.9) and (11.9.10)

Q is the volumetric flow through the impeller [m³/s]

k_2/k_1 are blade thickness coefficients

d_{2m}/d_{1m} are meridional diameters [m]. It will considered that $d_{1i} = d_{1m}$

The blade thickness coefficients k_2/k_1 are calculated as

$$k_1 = \frac{d_{1m} \cdot \pi}{d_{1m} \cdot \pi - Z_{La} \cdot \frac{e_1}{\sin \beta_1}} \quad [-] \quad (11.9.13)$$

$$k_2 = \frac{d_{2m} \cdot \pi}{d_{2m} \cdot \pi - Z_{La} \cdot \frac{e_2}{\sin \beta_2}} \quad [-] \quad (11.9.14)$$

Where,

d_{1m}/d_{2m} are the meridional diameters calculated in Eq. (11.9.15) and (11.9.16) [m]

Z_{La} is the number of blades

e_1/e_2 is the blade thickness at inlet/outlet [m]

β_1/β_2 are the blade angles at inlet/outlet [°]

According to Figure 11-17, for a specific speed $n_q = 47.11$

$$\frac{d_{2m}}{d_2'} = 1 \quad [-] \quad (11.9.15)$$

$$\frac{d_{1m}}{d_2'} = 0.39 \quad [-] \quad (11.9.16)$$

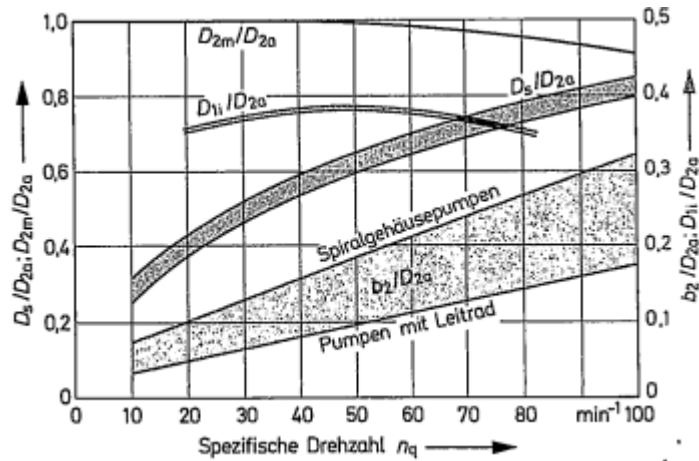


Figure 11-17 Diameter relations for different specific speeds. Source: (Bohl, 2013)

Blade angle β_1/β_2

The scaled blade angle are defined as

$$\beta_1' = \arctan \frac{C_{1m}}{U_1} \quad [^\circ] \quad (11.9.17)$$

Where,

C_{1m} is the meridional velocity at the inlet/outlet. Calculated in Eq.(11.9.9) and (11.9.10)

U_1 is the inlet/outlet blade speed. Calculated as $U = \omega \cdot r_{1/2}$

According to (Bohl, 2013), the outlet blade angle β_2' is dependent on the specific rotational speed.

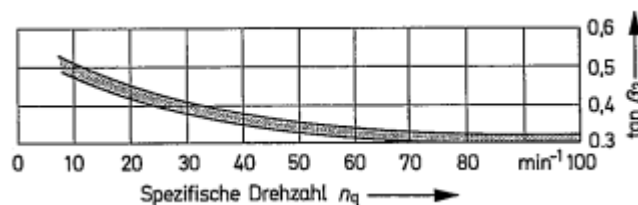


Figure 11-18 outlet blade angle with varying specific rotational speed. Source: (Bohl, 2013)

Number of blades Z_{La}

According to (Bohl, 2013), a good estimation for the number of blades in the impeller is

$$Z_{La}' \approx \frac{\beta_2}{3} \quad [-] \quad (11.9.18)$$

11.10 The Weibull distribution

This distribution is represented by the following equation when the wind speed $v \geq 0$

$$f(v) = \frac{k}{C} \left(\frac{v}{C}\right)^{k-1} e^{-\left(\frac{v}{C}\right)^k} \quad [-] \quad (11.10.1)$$

Where,

$f(v)$ represents de probability of a specific wind speed v

v is the wind speed [m/s]

k is the shape parameter of the function (it might be also identified as α in other sources)

C scaling parameter or characteristic velocity of the wind. **It is not the average speed in the distribution** despite being closely related to it.

A very important consideration is that the area enclosed under the curve must be equal to unity, otherwise the distribution is not plotted correctly.

Depending on the values k takes, the function turns out differently;

- If $k = 1$ the distribution becomes an exponential function
- If $k = 2$ the distribution becomes the Rayleigh distribution also known as Chi-squared χ^2
- If $k = 3.6$ the distribution is the closest to be a normal distribution.

Depending on the rugosity of the terrain we have approximate values for k (Martinez, 2017)

| Terrain | k of Weibull |
|----------|--------------|
| Interior | 2 |
| Sea | 3 |
| Islands | 5 |

Table 11-1 Values for different terrains

For instance, the month of January is chosen at the given location. In January according to wind databases (Anon., 2017) the $k = 5.607$ and $C = 8.857$

| | | | |
|-----|------|---|------------|
| m/s | f(v) | 1 | 2,7371E-05 |
|-----|------|---|------------|

| | | | |
|---|------------|--------------|---------------------|
| 2 | 0,00066686 | 10 | 0,15366299 |
| 3 | 0,00430912 | 11 | 0,05906656 |
| 4 | 0,01606751 | 12 | 0,01059306 |
| 5 | 0,04363659 | 13 | 0,00068354 |
| 6 | 0,09404206 | 14 | 1,146E-05 |
| 7 | 0,16389519 | 15 | 3,347E-08 |
| 8 | 0,22509918 | total | 0,9999999046 |
| 9 | 0,22823839 | | |

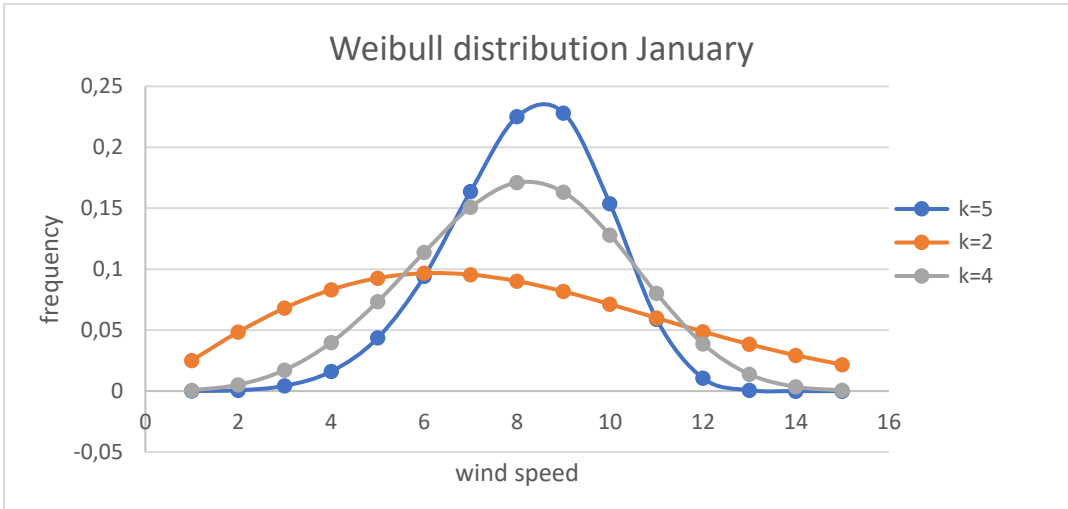
For the given location in El Hierro, the values of k and C according to the wind databases (Anon., 2017):

| Weibull k | | | | | | | | | | | | |
|-------------|------|-------|-------|-------|-------|-------|-------|-------|-------|-------|-------|-------|
| Jan | Feb | Mar | Apr | May | Jun | Jul | Aug | Sep | Oct | Nov | Dec | All |
| 5,607 | 3,1 | 5,296 | 3,361 | 3,373 | 3,279 | 5,805 | 3,92 | 2,567 | 2,308 | 3,502 | 3,042 | 2,973 |
| Weibull C | | | | | | | | | | | | |
| 8,857 | 8,63 | 8,14 | 6,098 | 6,921 | 5,947 | 8,591 | 7,477 | 4,793 | 5,148 | 7,269 | 5,735 | 7,059 |

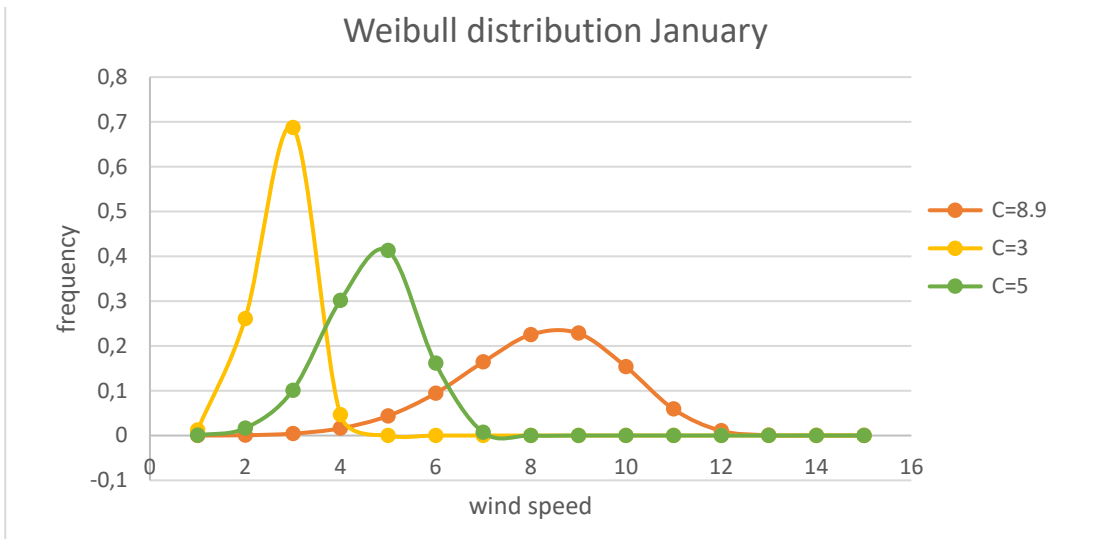
Tabla 11.10-1 Monthly values for k and C at 60 m in el Hierro

In Graph 11-2 it can be seen how the histogram looks like for January. The shape parameter k has been varied to see what effect it has in the distribution. In this case the same scale parameter C has been kept. Both parameters are seasonal and depend on the altitude too.

In Graph 11-3 the parameter C has been varied leaving k constant for all plots. Both graphs illustrate the importance of having accurate monthly data for this two parameters given the significant changes they cause in the distribution.



Graph 11-3 Effect of C in the distribution



Graph 11-2 Effect of k in the distribution

C.1 Effect of altitude

Another consideration to make is how the wind speed changes with height. Wind speed is theoretically null in contact with the ground. As we get away from the ground, the effects of friction decrease and the wind speed tends to increase. A gradient appears constituting a vertical wind speed profile (Figure 11-19).

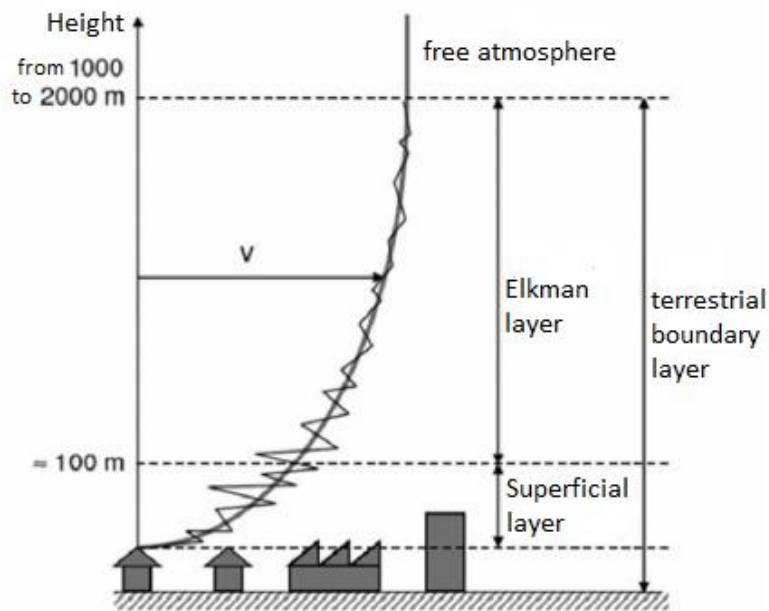


Figure 11-19 Variation of the wind's profile with altitude. Source: (Martinez, 2017)

The wind speed must be corrected if it's measure is not done already at hub height.

$$v = v_0 \frac{\ln\left(\frac{h}{z_0}\right)}{\ln\left(\frac{h_{ref}}{z_0}\right)} \quad [m/s] \quad (11.10.2)$$

Where,

v is the speed at height h [m/s]

h is the height above the terrain with speed v [m]

v_0 is the reference speed known at the known height h_{ref} [m/s]

h_{ref} is the reference height at which v_0 is known [m]

z_0 is the length of rugosity in the normal direction of the wind [m]. Some examples are listed in Table 11-2

| | | | |
|-----------|-----------------|------------|-------|
| z_0 [m] | Kind of terrain | 0.8 | Woods |
| 1 | City | | |

| | |
|-------------|-------------------------------|
| 0.5 | Districts in the city suburbs |
| 0.3 | Constructed terrains |
| 0.2 | Set of trees or shrubs |
| 0.1 | Closed agricultural land |
| 0.05 | Open agricultural land |

| | |
|---------------|---|
| 0.03 | Agricultural land with few trees or buildings |
| 0.01 | Airports, landing tracks |
| 0.009 | Meadows |
| 0.005 | Plain ground |
| 0.001 | Snowed land |
| 0.0003 | Sandy areas |
| 0.0001 | Water surfaces |

Table 11-2 Length of rugosity. Source: (Martinez, 2017)

An alternative method to evaluate the variation of wind speed with height is with the exponential law of Hellmann.

Exponential Law of Hellmann

This law follows a statistical equation:

$$v = v_0 \left(\frac{h}{h_0} \right)^\alpha \quad [m/s] \quad (11.10.3)$$

Where,

v_0 is the reference speed known at the known height h_0 [m/s]

h_0 is the reference height at which v_0 is known [m]

h is the height above the terrain with speed v [m]

α is the Hellmann coefficient calculated in Eq.(11.10.4)

The Counihan approximation gives an empirical formula to calculate α

$$\alpha = 0.096 \log_{10} z_0 + 0.016(\log_{10} z_0)^2 + 0.24 \quad [-] \quad (11.10.4)$$

Where,

z_0 takes values between $0.0001 \text{ m} < z_0 < 10 \text{ m}$ and represents the rugosity of the surface (Table 11-2)

Comparing the values of corrected v with the standard method and the Hellmann Law, there's a divergence of a 3% in the result

Effect of altitude on k and C

Altitude also influences the above mentioned k and C . (Lopez, 2012) When the stated parameters are known for one altitude but they are required at another altitude, the *Justus and Mikhail relation* gives the value of them for recommended heights above 100 m. and for terrains with low rugosity and just in the case that the values at the desired height are not available.

$$k = k_0 \left(\frac{1 - 0.088 \ln \left(\frac{h_0}{10} \right)}{1 - 0.088 \ln \left(\frac{h}{10} \right)} \right) \quad [-] \quad (11.10.5)$$

Where,

k_0 is the original value for k at altitude h_0

k is the new value for k at altitude h

$$C = C_0 \left(\frac{h}{h_0} \right)^\beta \quad [-] \quad (11.10.6)$$

Where,

C_0 is the original value for k at altitude h_0 [-]

C is the new value for k at altitude h [-]

β coefficient calculated in Eq.(11.10.7) [-]

$$\beta = \frac{0.37 - 0.088 \ln C_0}{1 - 0.088 \ln \left(\frac{h_0}{10} \right)} \quad [-] \quad (11.10.7)$$

11.11 The Betz law

The flow rate of air is conserved along the control volume:

$$Q_{air} = S_1 v_1 = S v = S_2 v_2 \quad [m^3/s] \quad (11.11.1)$$

Where,

S_1 surface area at the inlet of the control volume [m^2]

v_1 is the air's speed at the inlet [m/s]

S is the swept area by the rotor [m^2]

v is the wind's speed when crossing the blades [m/s]

S_2 surface area at the outlet of the control volume [m^2]

v_2 is the air's speed at the outlet[m/s]

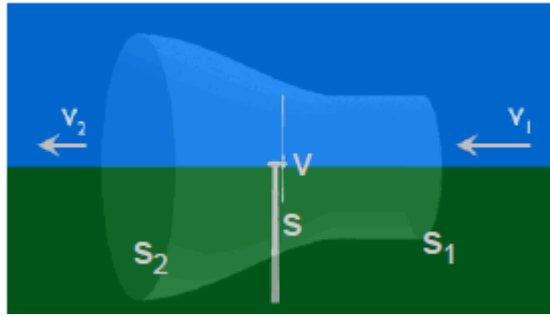


Figure 11-20 wind speeds in control volume

The force exerted by the air on the blades:

$$F_{air} = \rho Q_{air} (v_1 - v_2) = \rho S v (v_1 - v_2) \quad [N] \quad (11.11.2)$$

Where,

ρ is the air's density [kg/m³]

Q_{air} is the air flow calculated in Eq.(11.11.1)

The power absorbed by the blades:

$$P_{blades} = F_{air} v = \rho S v^2 (v_1 - v_2) \quad [W] \quad (11.11.3)$$

Where,

F_{air} is the force exerted by the wind over the blades calculated in Eq.(11.11.2)

The change in the air's kinetic energy per unit time must be equal to the mechanical power absorbed by the blades:

$$P_{blades} = \frac{1}{2} \rho S v (v_1^2 - v_2^2) \quad [W] \quad (11.11.4)$$

With this relation, we obtain:

$$v = \frac{v_1 + v_2}{2} \quad [m/s] \quad (11.11.5)$$

Taking into consideration the above equations, finally the Betz formula for maximum power is obtained:

$$P_{wind,max} = \frac{8}{27} \rho S v^3 = \frac{1}{2} C_p \rho S v^3 \quad [W] \quad (11.11.6)$$

Where,

ρ is the air density [kg/m³]

S is the swept area [m²] $\frac{\pi D^2}{4}$

D is the rotor's diameter [m]

v is the wind's speed [m/s]

C_p is the turbine's power coefficient which can be a maximum value of $\frac{16}{27}$

Besides power, torque is also an important concept

$$M_{wind,max} = \frac{1}{2} \rho C_m r S v^3 = \frac{P_{wind,max}}{\omega} \quad [N \cdot m] \quad (11.11.7)$$

Where,

C_m is the turbine's torque coefficient [-]

r is the radius of the rotor [m]

$P_{wind,max}$ is power calculated in Eq.(11.11.6)

ω is the angular velocity of the wind turbine [rad/s]

Chapter 12 Appendix 2

12.1 Maps of the island of el Hierro



Figure 12-2 Altimetric map of the island. Source: (Anon., 2017)



Figure 12-1 Electrical map of the island. Source: (Anon., 2017)

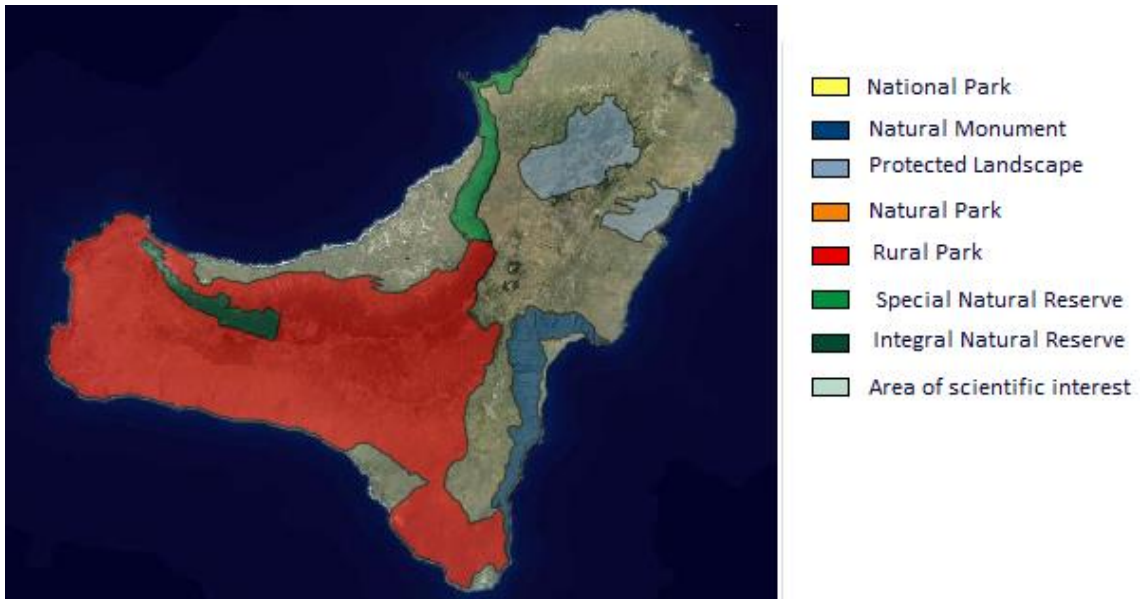


Figure 12-3 Non-buildable areas. Source: (Anon., 2017)

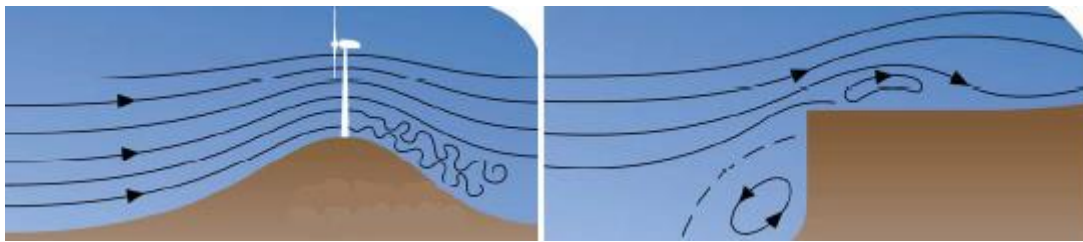


Figure 12-4 Positive and negative influence in wind speed due to hills and cliffs. Source: (Martinez, 2017)

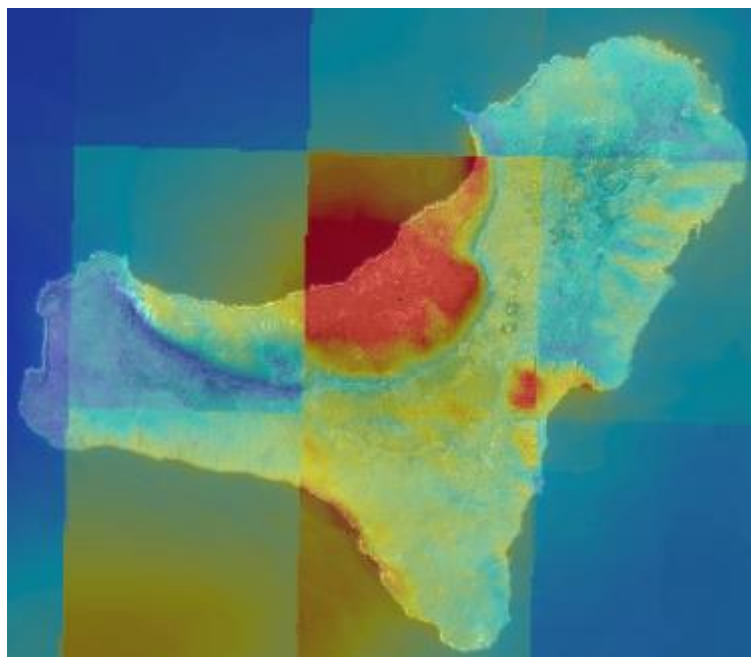


Figure 12-5 Air turbulences at 60m. Source: (Anon., 2017)

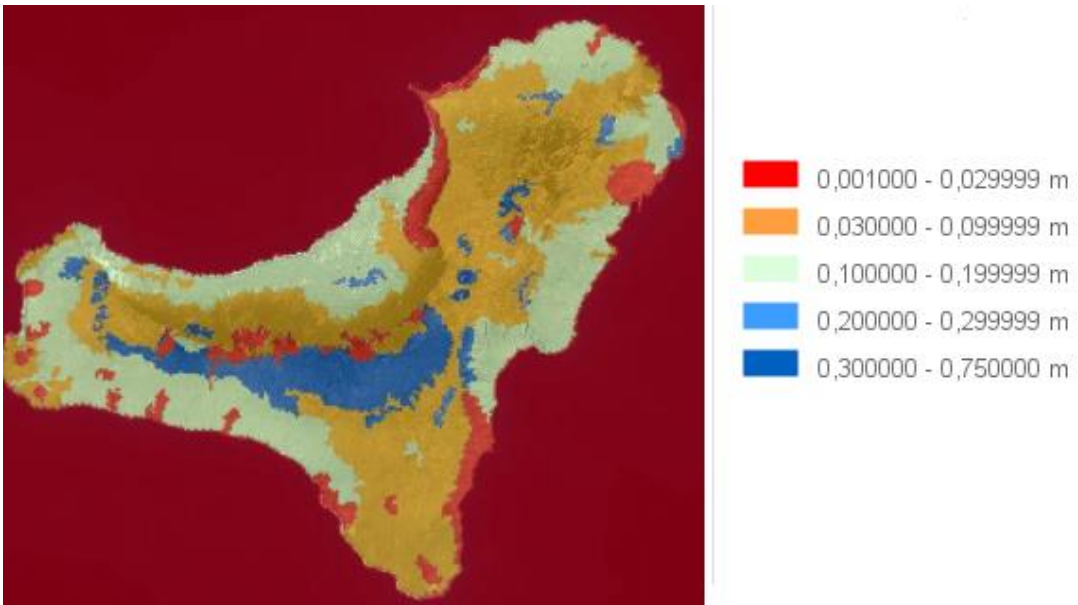


Figure 12-6 Map of rugosities present in the surface. Source: (VISOR GRAFCAN , 2017)

12.2 Wind roses

In Figure 12-9 and Figure 12-8 more detailed wind roses with the monthly and hourly wind orientation are detailed

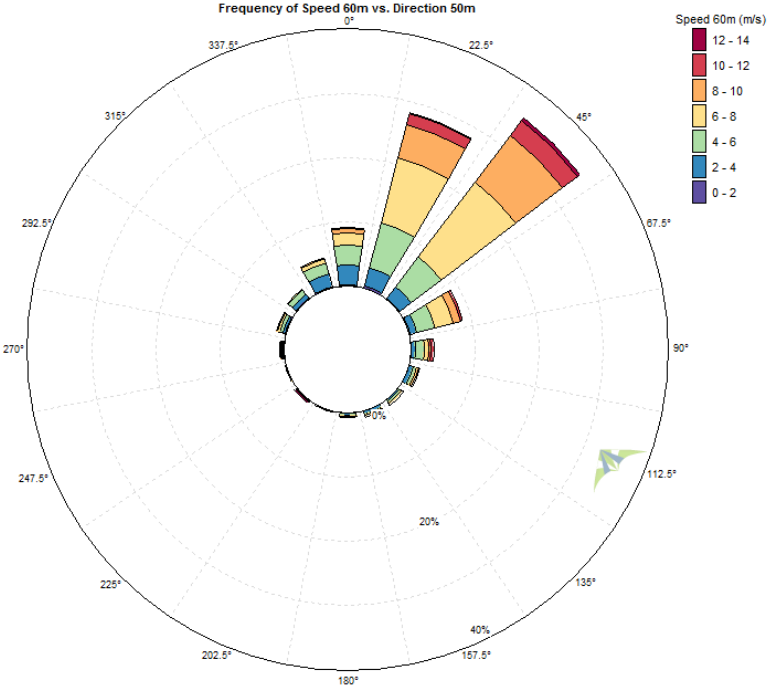


Figure 12-7. Frequency of speeds at 60 m above ground level. Source: (Anon., 2017)

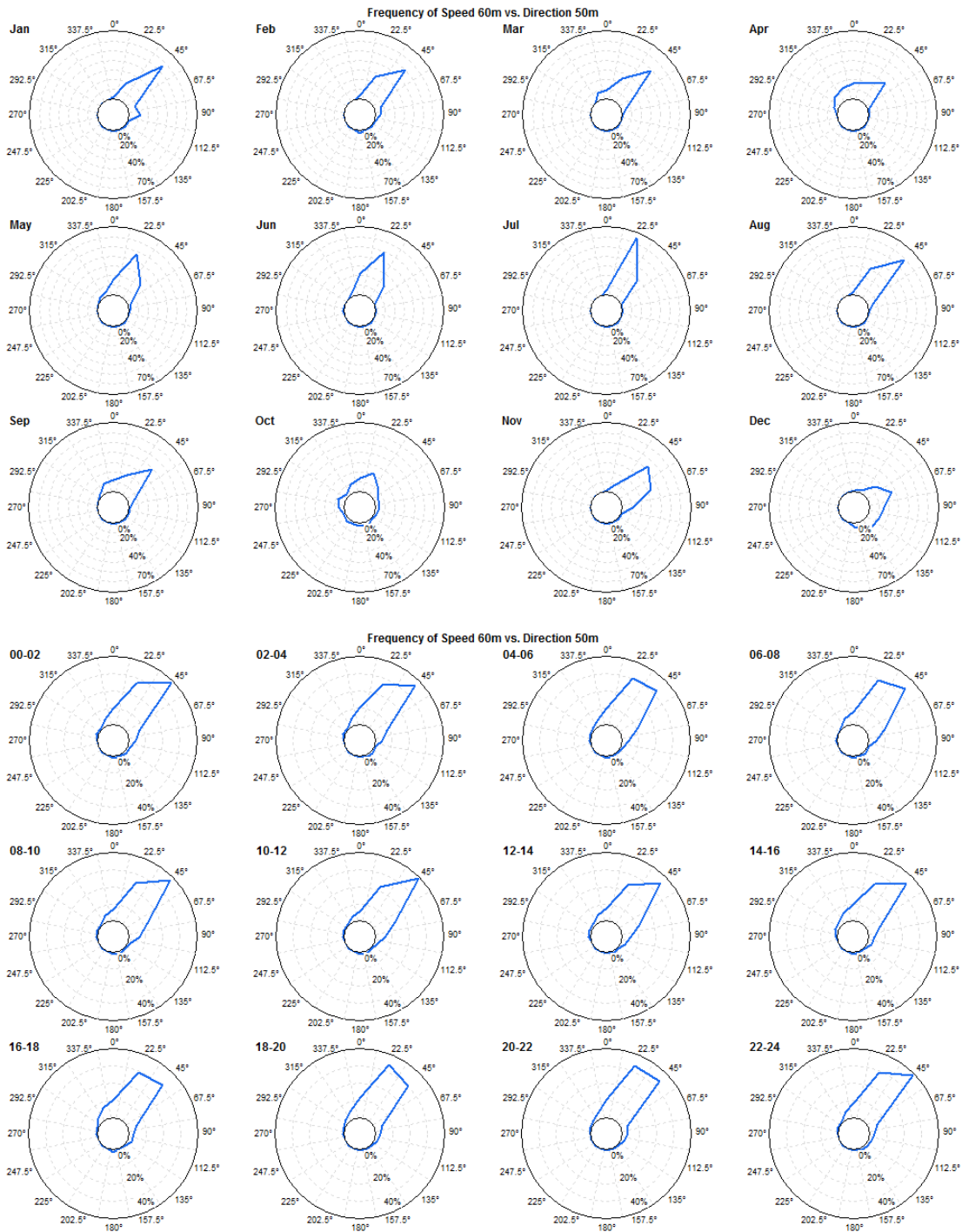
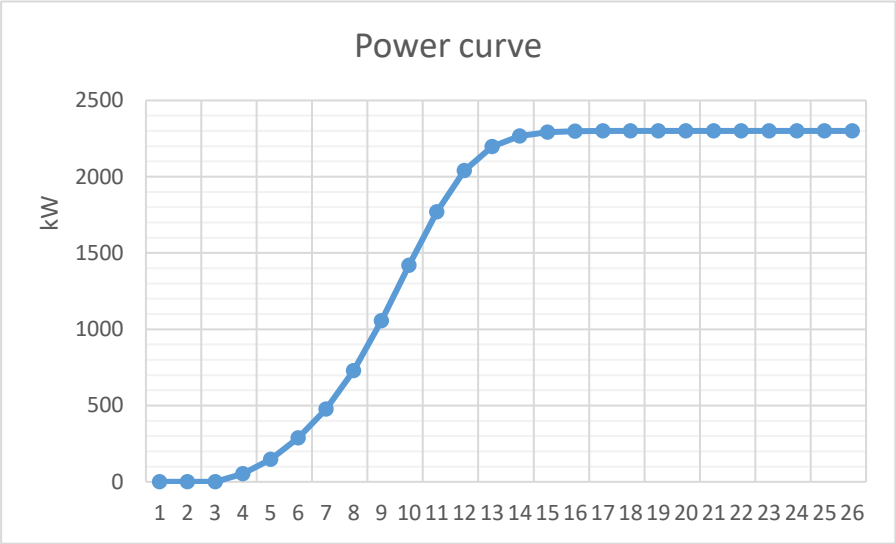


Figure 12-8 Hourly wind rose at Punta de Ajones. Source: (Anon., 2017)

12.3 Data of the wind turbine

| Mechanical properties | | Electrical properties | |
|-----------------------|---------------------|-----------------------|-------------|
| Swept area | 5300 m ² | Generator | Asincronous |
| Nº of blades | 3 | Frecuencia | 50 Hz |
| Hub height | 60 m | Rotor Ø [m] | 82.4 |
| | | Voltage | 690 V |

Table 12-1 Wind turbine characteristics. Source: (The wind power, s.f.)



Graph 12-1 Power curve for Bonus 2300/82.4

12.4 Data for the hydro storage dimensioning

Abacus for the calculation of equivalent meters of pipe for it's accessories

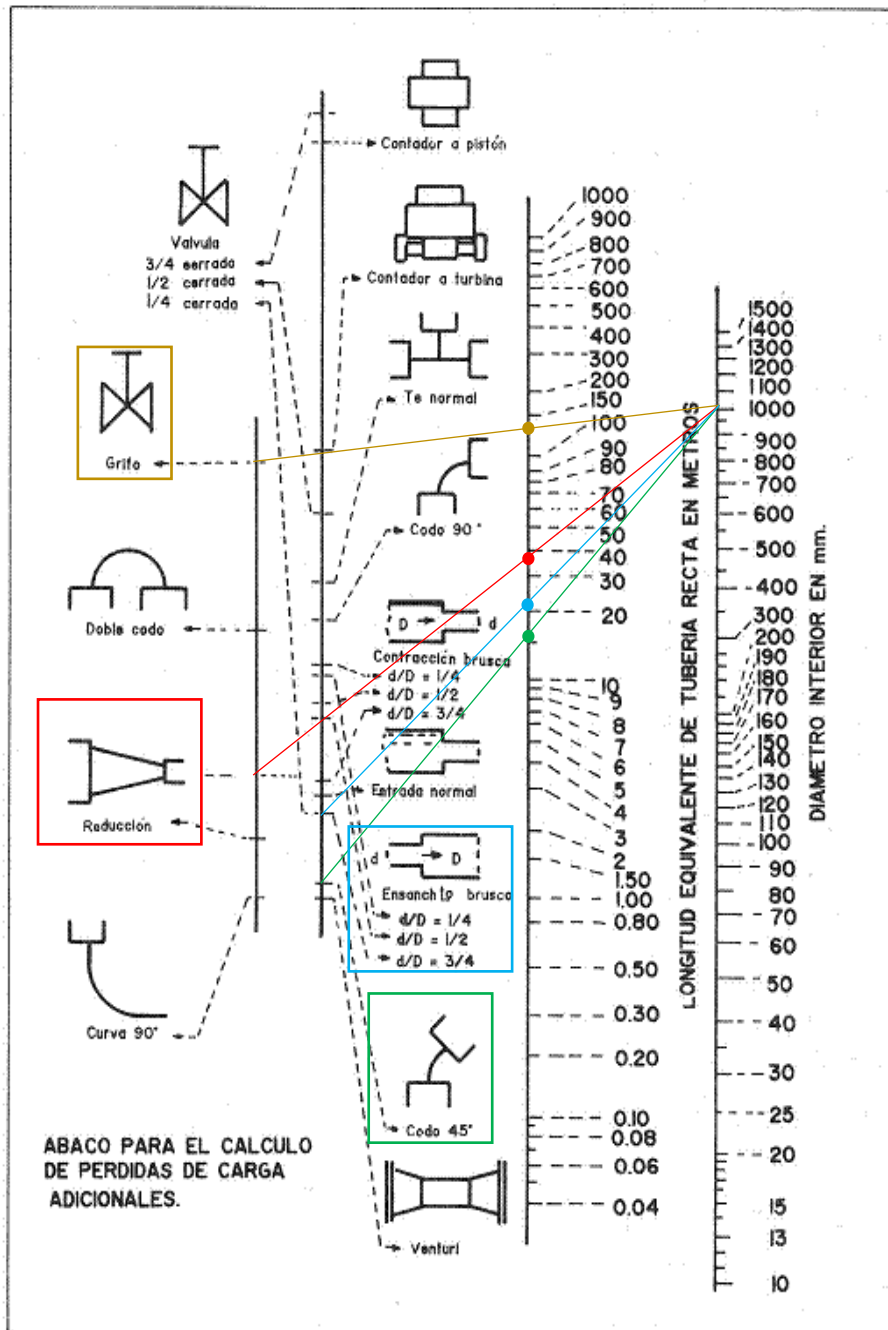


Figure 12-10 Abacus for the calculation of accessory losses. Source:

| | | |
|---|------------|---------------------|
| Maximum flow rate | 2 | [m ³ /s] |
| Diameter | 1 | [m] |
| Section | 0.7854 | [m ²] |
| Maximum flow speed | 5.08 | [m/s] |
| Rugosity of the pipe (cast iron) | [0.12-0.6] | [mm] |
| Length | 275.04 | [m] |
| Equivalent length | 407.04 | [m] |

Table 12-2 dimensions of the pipe network for hydrostorage

| | | |
|---------------------------------------|--------|----------------------|
| Lower calorific value (diesel) | 36500 | [MJ/m ³] |
| | 10.153 | [KWh/l] |
| Efficiency of the engine | 96 | [%] |

Table 12-3 Fuel and engine data

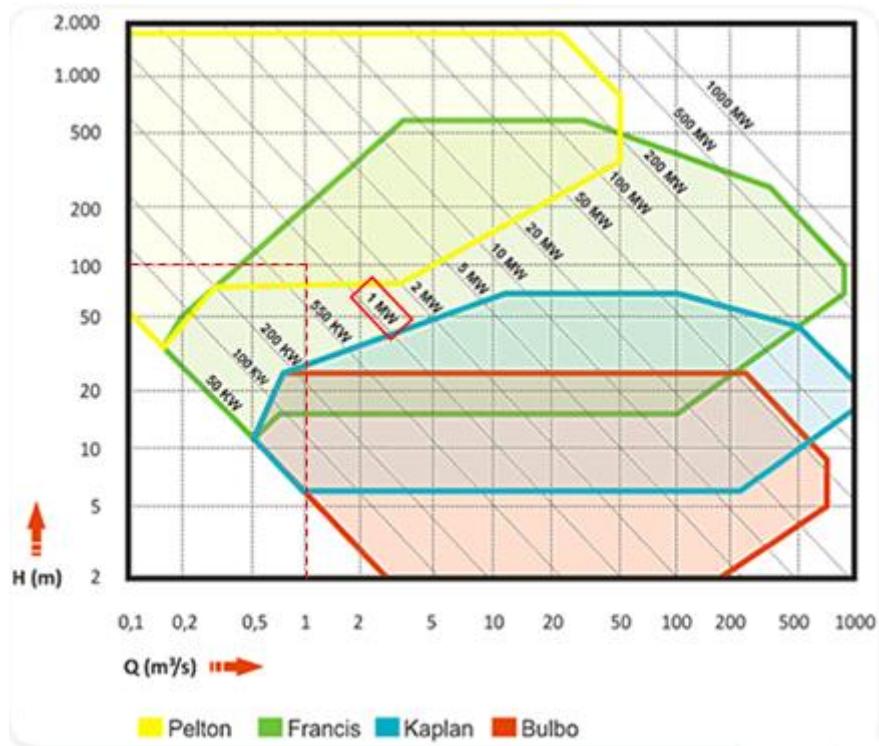


Figure 12-11 Pump selection depending on flow and head

12.5 Parameters of the pump

Some of the parameters for the pump were obtained from previous reports, concretely the one indicated in the 'source' column in the following table

| Description | Symb | Initial | Final | unit | Source |
|-------------------------------------|-----------------|---------|-------|-------------------|------------------------|
| Distance between the vanes at inlet | a_1 | 16.26 | 16.26 | mm | (Hærvig, et al., 2012) |
| Distance between vanes at outlet | a_2 | 27.10 | 27.10 | mm | (Hærvig, et al., 2012) |
| Blade height at inlet | b_1 | 14.48 | 14.18 | mm | (Hærvig, et al., 2012) |
| Blade height at outlet | b_2 | 10.19 | 10.19 | mm | (Hærvig, et al., 2012) |
| Inlet blade angle | β_1 | 33.08 | 33.08 | ° | (Hærvig, et al., 2012) |
| Outlet blade angle | β_2 | 27.28 | 30 | ° | |
| Inner diameter of the impeller | d_1 | 64.34 | 64.34 | mm | (Hærvig, et al., 2012) |
| Outer diameter of the impeller | d_2 | 142 | 142 | mm | (Hærvig, et al., 2012) |
| Thickness of the blades at inlet | e_1 | 2.17 | 1.75 | mm | |
| Thickness of the blades at outlet | e_2 | 3.47 | 2.8 | mm | |
| Number of blades | Z_{La} | 5 | 9 | blades | |
| Radial distance to the gap | d_{sp} | 75.95 | 75.95 | mm | (Hærvig, et al., 2012) |
| Length of the gap | L_{sp} | 2.88 | 2.88 | mm | (Hærvig, et al., 2012) |
| Blade inclination inlet | λ_{La1} | 90 | 90 | ° | (Hærvig, et al., 2012) |
| Blade inclination at outlet | λ_{La2} | 90 | 90 | ° | (Hærvig, et al., 2012) |
| Gap between impeller and housing | s | 0.25 | 0.25 | mm | (Hærvig, et al., 2012) |
| Flow at BEP | Q_{BEP} | 12.8 | 12.8 | m ³ /h | (Hærvig, et al., 2012) |
| Maximum flow | Q_{max} | 17 | 17 | m ³ /h | (Hærvig, et al., 2012) |

Table 12-4 Parameter of Grundfos NK 32-125/142 with optimized values

Bibliography

- Anon., 2017. *Red Eléctrica Española*. [En línea]
Available at: <http://www.ree.es/es/actividades/sistema-electrico-canario/red-de-transporte>
- Anon., 2017. *Visor GRAFCAN*. [En línea]
Available at: <http://visor.grafcan.es/visorweb/#>
- Anon., 2017. *Why underfile*. [En línea]
Available at: <https://www.ekwestrel.com/impellers-why-underfile/>
- Anon., 2017. *Windographer wind data base*. [En línea]
Available at: www.windographer.com
- Anon., 2017. *Windographer*. [En línea]
Available at: <https://www.windographer.com/>
- Association, D. W. I., 2003. [En línea]
Available at: <http://xn--drmstrre-64ad.dk/wp-content/wind/miller/windpower%20web/en/tour/wres/pwr.htm>
- Bohl, W., 2013. *Strömungs-maschinen 2*. s.l.:Vogel Fachbuch Kamprath-Reihe.
- Çengel, Y. A., M.Cimbala, J. & H.Turner, R., 2012. *Fundamentals of Thermal-Fluid Sciences*. 4th ed. s.l.:McGrawHill.
- Dixon, S., 1978. *Fluid Mechanics, Thermodynamics of Turbomachinery*. 5th ed. s.l.:ELSEVIER.
- gate, R., 2014. [En línea]
Available at: https://www.researchgate.net/figure/267048009_fig4_A-pumped-hydroelectric-storage-plant-layout
- Grundfos, 2008. *The centrifugal pump*. 1st edition ed. s.l.:s.n.
- Gulich, J. F., 2010. *Centrifugal Pumps*. 2nd edition ed. s.l.:Springer.
- Hærvig, J., Johansen, F. E. & Knudsen, M. H., 2012. *Design and Test of Impellers for Centrifugal Pumps*, s.l.: s.n.
- Lopez, M. V., 2012. *Ingeniería de la energía eólica*. s.l.:Marcombo S.A..
- M.G.Patel, A., 2013. Effect of Impeller Blade Exit Angle on the Performance of. *International Journal of Emerging Technology and Advanced Engineering*, 3(1).
- Martinez, H., 2017. *Sistemas de EO: Introduccion a las Instalaciones*. s.l.:s.n.
- Quora, 2015. [En línea]
Available at: <https://www.quora.com/Why-do-turbine-runners-have-odd-number-of-blades>
- The wind power, w. e. m. i., s.f. [En línea]
Available at: www.thewindpower.net/turbine_en_312_bonus_2300.php
- Tuzson, J., 2000. *Centrifugal pump design*. s.l.:s.n.

Wang, C. y otros, 2016. Optimal design of multistage centrifugal pump based on the combined. *Applied Energy*.

Wikipedia, 2017. *Wikipedia*. [En línea]
Available at: https://es.wikipedia.org/wiki/El_Hierro
[Último acceso: 2017].